CHALMERS

Ringhals Diagnostics and Monitoring, Annual Research Report 2016-17

I. PÁZSIT
C. MONTALVO
H. N. TRAN
H. NYLÉN
O. OLVERA GUERRERO

Nuclear Engineering Group
Division of Subatomic and Plasma Physics
CHALMERS UNIVERSITY OF TECHNOLOGY
Gothenburg, Sweden, 2017
CTH-NT-333/RR-21 December 2017

CTH-NT-333/RR-21 December 2017

Ringhals Diagnostics and Monitoring, Annual Research Report 2016-2017

I. Pázsit, C. Montalvo, H. N. Tran, H. Nylén and
O. Olvera Guerrero

Nuclear Engineering Group
Division of Subatomic and Plasma Physics
Chalmers University of Technology
SE-412 96 Göteborg, Sweden
ISSN 0281-9775

Ringhals Diagnostics and Monitoring, Annual Research Report 2016-2017

I. Pázsit, C. Montalvo, H. N. Tran, H. Nylén and O. Olvera Guerrero

Nuclear Engineering Group
Division of Subatomic and Plasma Physics
Chalmers University of Technology
SE-412 96 Göteborg, Sweden

Abstract

This report gives an account of the work performed by the Division of Subatomic and Plasma Physics (formerly, Division of Nuclear Engineering), Chalmers, in the frame of a research collaboration with Ringhals, Vattenfall AB, contract No. 663628-054. The contract constitutes a 1-year co-operative research work concerning diagnostics and monitoring of the BWR and PWR units. The work in the contract has been performed between July 1st 2016, and December 31st, 2017. During this period, we have worked with six main items as follows:

1. Further development and improvement of the coupled coarse-fine mesh CORE SIM-based model;
2. Further investigation of the point-kinetic component of the noise induced by fuel assembly vibrations;
3. Analysis of new ex-core measurements, taken in R-4 after power increase;
4. Further development and test of the mode separation model as applied to 3-D "wobbling" type or "tilting" type core-barrel vibrations;
5. A basic study in neutron noise theory which could provide some indirect support for the determination of the void fraction from neutron noise measurements;
6. A pilot study of the possibility of using fission chambers for zero power noise experiments.

The work was performed at the Division of Subatomic and Plasma Physics, Chalmers University of Technology by Imre Pázsit (project co-ordinator), Cristina Montalvo (visitor from the Technical University of Madrid), Hoai-Nam Tran (research collaborator from Duy Tan University, Vietnam), Omar Alejandro Olvera Guerrero (visitor, PhD student at UAM/Autonomus Metropolitan University, Mexico City, Mexico) and Henrik Nylén, the contact person at Ringhals. The measurements reported in Chapter 6 were designed and executed by our collaborating partners in EPFL/PSI, Mathieu Hursin, Oskari Pakari and Vincent Lamirand.

CONTENTS

1. INTRODUCTION

This report gives an account of the work performed by the Nuclear Engineering Group of the Division of Subatomic and Plasma Physics (former Division of Nuclear Engineering), Chalmers, in the frame of a research collaboration with Ringhals, Vattenfall AB, contract No. 663628-054. The contract constitutes a 1-year cooperative research work concerning diagnostics and monitoring of the BWR and PWR units. The work in the contract has been performed between July 1st 2016, and December 31st, 2017. During this period, we have worked with six main items as follows:

1. Further development and improvement of the coupled coarse-fine mesh CORE SIM-based model;
2. Further investigation of the point-kinetic component of the noise induced by fuel assembly vibrations;
3. Analysis of new ex-core measurements, taken in R-4 after power increase;
4. Further development and test of the mode separation model as applied to 3-D "wobbling" type or "tilting" type core-barrel vibrations;
5. A basic study in neutron noise theory which could provide some indirect support for the determination of the void fraction from neutron noise measurements;
6. A pilot study of the possibility of using fission chambers for zero power noise experiments.

This work was performed at the Division of Subatomic and Plasma Physics, Chalmers University of Technology by Imre Pázsit (project co-ordinator), Cristina Montalvo (visitor from the Technical University of Madrid), Hoai-Nam Tran (research collaborator from Duy Tan University), Omar Alejandro Olvera Guerrero (visitor, PhD student at UAM/Autonomus Metropolitan University, Mexico City, Mexico) and Henrik Nylén, who was also the contact person at Ringhals. The measurements reported in Chapter 6 were designed and executed by our collaborating partners in EPFL Lausanne/PSI, Mathieu Hursin, Oskari Pakari and Vincent Lamirand.

2. FURTHER DEVELOPMENT AND IMPROVEMENT OF THE COUPLED COARSE-FINE MESH CORE SIM-BASED MODEL

The goal in this stage was the further development and improvement of the coupled coarse-fine mesh CORE SIM-based model presented in the previous Stage (Etapp 2015, [1]) and used for simulating the noise induced by three dimensional fuel assembly vibrations. As reported in the previous stages, the vibrations of the individual fuel assemblies contribute significantly to the ex-core detector noise, which is used for diagnosing the core barrel vibrations. A good knowledge of the ex-core noise induced by fuel assembly vibrations is therefore essential in order to interpret and diagnose the core-barrel vibrations correctly.

Such calculations have been already performed and analysed with the use of the noise simulator CORE SIM [2]. However, one limitation was that with the general mesh size used in CORE SIM, the vibration amplitude could not be chosen sufficiently small. The main objective in this stage was thus to develop a better model of the realistic displacement (in the sub-millimetre range) of the fuel assembly during vibrations at the fine mesh scale. This required using more advanced and faster numerical techniques for solving the governing CORE SIM equations. An overall decreasing of the mesh size would have led to unacceptably long running times and memory requirements. Hence, a model was developed with non-uniform mesh size. Around the vibrating fuel assembly, in a layer several times thicker than the vibration amplitude, a fine mesh was used, whereas in the rest of the core the same coarse mesh was used as before.

This extension of the method and the computational models of a previous work has been applied to two different PWR cores. Both the performance of the model, as well as the effect of cycle burnup on the properties of the ex-core detector noise could be investigated. The final goal was to further examine the hypothesis that the amplitude of the peak in the auto power spectral density (APSD), induced by fuel assembly vibrations, increases during the cycle. Stochastic vibrations along a random two-dimensional trajectory of individual fuel assemblies were assumed to occur at different locations in the cores. Two models regarding the displacement amplitude of the vibrating assembly have been considered to determine the noise source. Then, the APSD of the ex-core detector noise was evaluated at three burnup steps.

Similarly to the findings of the previous work, the results show that there is no monotonic trend of the change of the APSD of the ex-core detector, induced by a single vibrating assembly, at a random position. However, the increase of APSD occurs predominantly for peripheral assemblies. When assuming simultaneous vibrations of a number of fuel assemblies uniformly distributed over the core, the effect of the peripheral assemblies dominate the ex-core neutron noise. This behaviour was found similarly in both cores, thereby further corroborating our previous hypothesis.

The work reported in this Chapter was performed by a group led by our collab-

orating partner Hoai Nam Tran. The work was published in Nuclear Science and Technology [3], and the description below largely follows that article.

2.1 The neutron noise equations in two group theory

The noise equation in two-group diffusion theory is derived from the time-dependent diffusion equation by splitting the time-dependent quantities into mean values and fluctuations,

$$X(\boldsymbol{r},t) = X(\boldsymbol{r}) + \delta X(\boldsymbol{r},t), \tag{2.1}$$

removing the static parts, performing a Fourier transform, eliminating the delayed neutron precursors, and neglecting the second-order terms (linear theory). The first order noise equation is written as follows [4, 5]:

$$\left[\nabla.\overline{\overline{D}}(\boldsymbol{r})\nabla + \overline{\overline{\Sigma}}_{dyn}(\boldsymbol{r},\omega)\right] \times \begin{bmatrix} \delta\phi_1(\boldsymbol{r},\omega) \\ \delta\phi_2(\boldsymbol{r},\omega) \end{bmatrix} = \begin{bmatrix} S_1(\boldsymbol{r},\omega) \\ S_2(\boldsymbol{r},\omega) \end{bmatrix} \tag{2.2}$$

where

$$\overline{\overline{D}}(\boldsymbol{r}) = \begin{bmatrix} D_1(\boldsymbol{r}) & 0 \\ 0 & D_2(\boldsymbol{r}) \end{bmatrix}, \tag{2.3}$$

$$\overline{\overline{\Sigma}}_{dyn}(\boldsymbol{r},\omega) = \begin{bmatrix} -\Sigma_1(\boldsymbol{r},\omega) & \nu\Sigma_{f2}(\boldsymbol{r},\omega) \\ \Sigma_{rem}(\boldsymbol{r}) & -\Sigma_{a2}(\boldsymbol{r},\omega) \end{bmatrix}, \tag{2.4}$$

$$\Sigma_1(\boldsymbol{r},\omega) = \Sigma_{a1}(\boldsymbol{r},\omega) + \Sigma_{rem}(\boldsymbol{r}) - \nu\Sigma_{f1}(\boldsymbol{r},\omega), \tag{2.5}$$

$$\nu\Sigma_{f1,2}(\boldsymbol{r},\omega) = \frac{\nu\Sigma_{f1,2}(\boldsymbol{r})}{k_{eff}}\left(1 - \frac{i\omega\beta_{eff}}{i\omega+\lambda}\right), \tag{2.6}$$

$$\Sigma_{a1,2}(\boldsymbol{r},\omega) = \Sigma_{a1,2}(\boldsymbol{r},\omega) + \frac{i\omega}{\upsilon_{1,2}}. \tag{2.7}$$

In the above equations,

$\delta\phi_g$ is the neutron noise in group g with $g = 1, 2$ representing the fast and thermal energy groups, respectively;

D_g is the diffusion coefficient in group g;

$\Sigma_{a,g}$ is the macroscopic absorption cross section in group g;

$\nu\Sigma_{f,g}$ is the macroscopic production cross section in group g;

Σ_{rem} is the macroscopic scattering cross section from the fast group to the thermal group (removal cross section);

k_{eff} is the effective multiplication factor;

β_{eff} is the total delayed neutron fraction;

λ is the delayed neutron decay constant;

υ_g is the neutron velocity in group g;

ω is the angular frequency.

The right hand side vector in Eq. (2.2) represents the noise source in the fast and thermal groups. The noise source can be modelled through the fluctuations of macroscopic cross-sections as a result of mechanical or thermal processes in the core, such as absorption perturbation, core barrel vibrations, fuel assembly vibrations, core inlet coolant temperature fluctuations etc., and is written as follows:

$$\begin{bmatrix} S_1(\boldsymbol{r},\omega) \\ S_2(\boldsymbol{r},\omega) \end{bmatrix} = \overline{\phi}_{rem}(\boldsymbol{r})\delta\Sigma_{rem}(\boldsymbol{r}) + \overline{\overline{\phi}}_a(\boldsymbol{r}) \begin{bmatrix} \delta\Sigma_{a1}(\boldsymbol{r},\omega) \\ \delta\Sigma_{a2}(\boldsymbol{r},\omega) \end{bmatrix} + \overline{\overline{\phi}}_f(\boldsymbol{r}) \begin{bmatrix} \delta\nu\Sigma_{f1}(\boldsymbol{r},\omega) \\ \delta\nu\Sigma_{f2}(\boldsymbol{r},\omega) \end{bmatrix} \tag{2.8}$$

where the terms δX_i, $i = \{\text{rem, a1, a2, f1, f2}\}$ stand for the fluctuations of the macroscopic cross sections, corresponding to the actual perturbation (in this case to the fuel assembly movement), and

$$\overline{\phi}_{rem}(\boldsymbol{r}) = \begin{bmatrix} \phi_1(\boldsymbol{r}) \\ -\phi_1(\boldsymbol{r}) \end{bmatrix}, \tag{2.9}$$

$$\overline{\overline{\phi}}_a(\boldsymbol{r}) = \begin{bmatrix} \phi_1(\boldsymbol{r}) & 0 \\ 0 & \phi_2(\boldsymbol{r}) \end{bmatrix}, \tag{2.10}$$

and

$$\overline{\overline{\phi}}_f(\boldsymbol{r}) = \begin{bmatrix} -\phi_1(\boldsymbol{r}) & -\phi_2(\boldsymbol{r}) \\ 0 & 0 \end{bmatrix}. \tag{2.11}$$

with ϕ_g being the neutron flux in group g.

In order to solve the neutron noise equation, the noise source in Eq. (2.8) must be determined via the fluctuations of the macroscopic cross sections of a specific scenario (in this case, the displacement of vibrating fuel assemblies). For pendular vibrations of a fuel assembly, the displacement function is a two-component vector $(\varepsilon_x, \varepsilon_y)$, whose components represent the displacement of the vibrating component around the equilibrium position in the x- and y-directions, respectively, according to the (x, y)-coordinates as displayed in Fig. 2.1.

For the vibrations in both the x- and y-directions, the displacements of a fuel assembly can be described by the two displacement functions ε_x and ε_y as identically distributed, independent random processes in a coordinate system which coincides with the principal axes of the most and least preferred directions [6]. The normalized total thermal noise itself is given as a linear combination of the noise induced by the vibrations in x- and y-directions as

$$\widetilde{\delta\phi}_2 = \delta\phi_2/\phi_2 = A_x\varepsilon_x(\omega) + A_y\varepsilon_y(\omega), \tag{2.12}$$

where $|A_x|$ and $|A_y|$ refer to the scaling factors of the ex-core noise with the fuel assembly vibration in x- or y-direction, respectively. The scaling factor and the phase of the noise are parameters which can be calculated using the noise simulator. In noise analysis, the gain and phase of APSD and cross power spectral density (CPSD) are used rather than the absolute values and the phase of the detector signals.

$$APSD_{\delta\phi_2} = |A_x|^2 APSD_{\varepsilon_x} + |A_y|^2 APSD_{\varepsilon_y} + 2A_xA_y\text{Re}\{CPSD_{\varepsilon_x\varepsilon_y}\}. \tag{2.13}$$

In the case of random 2D vibrations, following a model of random force acting on the assembly surface suggested by [6], one obtains that for the case of isotropic vibrations ($|\varepsilon_x| = |\varepsilon_y|$), $CPSD_{\varepsilon_x\varepsilon_y} = 0$, and the APSD of the ex-core noise can be simply calculated by

$$APSD_{\delta\phi_2} = |A_x|^2 + |A_y|^2. \tag{2.14}$$

2.2 PWR cores and modelling of fuel assembly vibration

Numerical calculations for investigating the effect of fuel burnup on the APSD of the ex-core detector noise induced by the vibrations of fuel assemblies have been performed based on two PWR core models. These correspond to the Ringhals-3 and the Ringhals-4 reactors at cycle 15, and will be referred to as Core 1 and Core 2, respectively. The two PWR cores have a similar configuration as illustrated in Fig. 2.1. Four ex-core detectors are assumed to be located at the outer periphery of the reflector to investigate the ex-core noise. In reality, the ex-core detectors are placed far outside from the core barrel. However, due to the limitation of the neutron noise simulator CORE SIM which does not allow simulating further than the reflector region, it is assumed that the neutron noise at the reflector region could represent the behaviour of the noise at the actual ex-core detector locations.

To investigate the burnup effect, calculations were performed at three burnup steps: the beginning of cycle (BOC), middle of cycle (MOC) and end of cycle (EOC). The cross section data and the kinetic parameters for the 2D models of the two PWR cores are taken from previous works [2, 7]. The kinetics parameters of the two cores are given in Table 2.1. The difference of fuel arrangement of the two cores is illustrated by the difference of the neutron flux distribution and its evolution with burnup in the two cores. Figs. 2.2 and 2.3 display the fast and thermal neutron flux distributions along the core diameter at the three burnup steps.

Table 2.1: Kinetic parameters of the two PWR cores.

Core 1					
Burnup	k_{eff}	β_{eff} (pcm)	λ (s^{-1})	v_1 (cm/s)	v_2 (cm/s)
BOC	1.00103	596.7	0.084356	1.78631×10^7	4.17195×10^5
MOC	1.00170	551.1	0.087121	1.81783×10^7	4.13994×10^5
EOC	1.00062	520.2	0.089139	1.81658×10^7	4.04119×10^5
Core 2					
BOC	1.00036	595.7	0.084499	1.78631×10^7	4.15325×10^5
MOC	1.00104	554.3	0.086985	1.81434×10^7	4.15859×10^5
EOC	1.01043	523.9	0.089071	1.81459×10^7	4.03678×10^5

In the present work, a similar assumption on the fuel assembly vibrations and on the 2D simulation model will be made as the one used in the previous work [2]. One of the limitations of the 2D model is that the vibration of fuel assembly is equivalent with a pendular vibration in a 3D model but not a second bending mode of the fuel assembly. Since in the present work we aim at investigating only the neutron noise at ex-core detectors located on the same axial plane, the 2D model can be considered

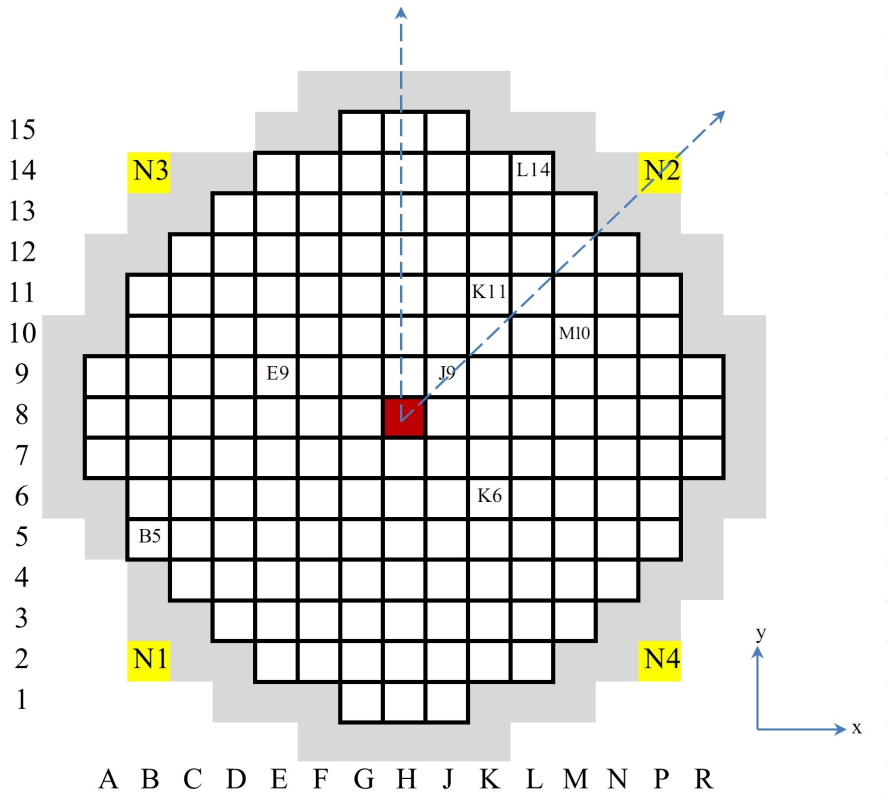

Figure 2.1: Core configuration of the PWR core with four ex-core detectors N1, N2, N3 and N4.

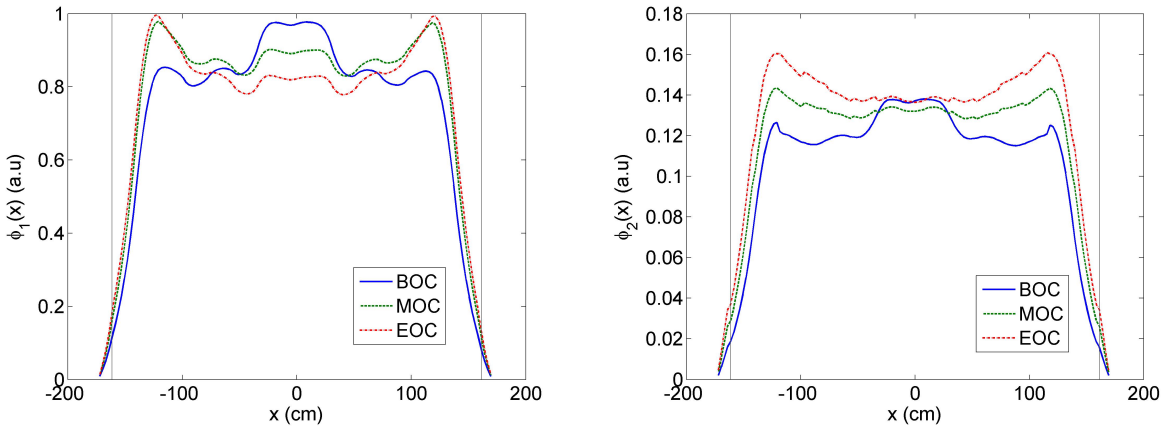

Figure 2.2: Neutron fluxes in fast (left) and thermal (right) groups across the diameter of Core 1.

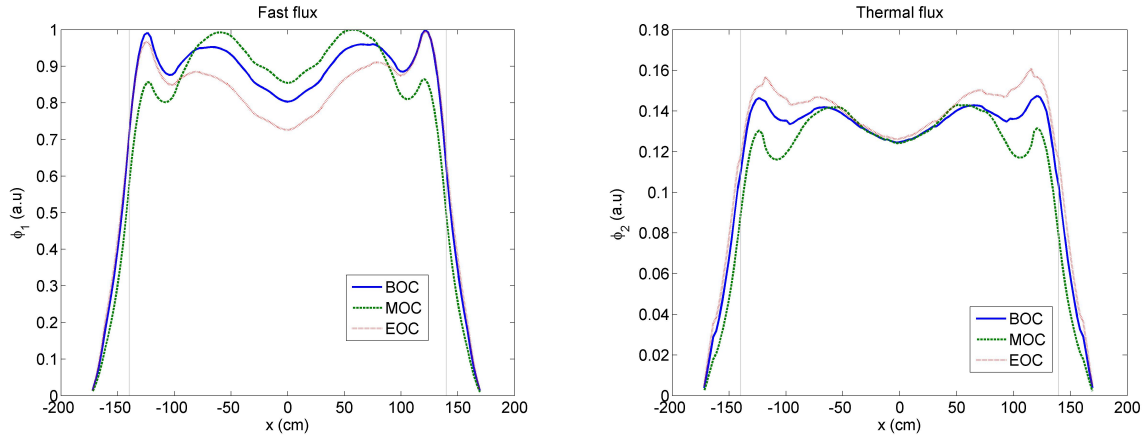

Figure 2.3: Neutron fluxes in fast (left) and thermal (right) groups across the diameter of Core 2.

as adequate. Further improvement of the simulation of second bending mode with a more realistic 3D model is planned in future work.

Acutally, there is not much information available regarding the characteristics of the displacements of the fuel assembly. According to Ref. [8], the displacement of a vibrating assembly is in the sub-millimetre range. However, in the numerical calculations, the mesh size of about 2.5 cm is used, which is too large compared to the displacement of a realistic vibration. In order to simulate the vibration with a flexible small displacement, the spatial discretisation was re-organised for the vibrating assembly by adding a very fine mesh around its border while keeping the original mesh size for all other assemblies. The size of the additional meshes could be defined as small as the amplitude of the displacement. Such an approach can be applied in a 2D simulation, where a very small displacement from vibrations can be simulated while the total number of meshes does not increase appreciably and therefore no significant numerical difficulty arises from the increase of different mesh sizes. Thus, the 2D version of CORE SIM was modified to handle additional fine meshes around the vibrating assembly for the purpose of this work.

The displacement of a fuel assembly is modelled by shifting materials for a very fine mesh around its equilibrium location. It means that the fluctuations in all types of cross-sections are taken into account in the noise source. If the displacement of a vibrating assembly is within the sub-millimetre range, the fluctuation of the cross sections is associated with the vibrating assembly only. However, if the amplitude of the displacement increases up to about 4 mm or more, a portion of the vibrating assembly will extend to the location of the neighbouring one, which hence also needs to be displaced. In this case the cross section fluctuations are associated with the displacement of two or more neighbouring assemblies. Therefore, two possible vibration models can be considered, regarding the amplitude of the displacement of the vibrating assembly as follows:

- Model 1 (large displacement): The displacement of the vibrating assembly

overlaps with the location of the neighbouring assemblies. Therefore, the real parts of the macroscopic cross section fluctuations in the meshes describing the displacement of the vibrating assembly around its equilibrium location are assumed to be the deviations of the cross sections of the vibrating assembly and its neighbouring one. In reality, this model assumes the collective vibrations of neighbouring fuel assemblies, to ensure that no space is occupied simultaneously by more than one fuel assembly.

- Model 2 (small displacement): The displacement of the vibrating assembly is within its own location, i.e. the vibration of fuel material does not overlap with the neighbouring assemblies. The real parts of the macroscopic cross section fluctuations in the meshes describing the displacement of the vibrating assembly are assumed to be the deviations of the cross sections of fuel material and water. In this case no collective motion of the neighbouring assemblies is required.

Regarding the vibration model, the previous work performed a systematic survey with both the directional trajectory and the stochastic trajectory vibration models [2], in which various directional vibrations in $x-$, $y-$ or both $x-$ and $y-$ directions have been considered. However, since the signals obtained in a measurement provide no information about the directional vibration, it is rather a random process of the vibration. This means that the stochastic trajectory vibration model can be considered as a more realistic model. Therefore, in this work we focus only on the stochastic trajectory vibration model and compare the results obtained with the two reactor cores.

2.3 Calculation of the neutron noise induced by fuel assembly vibrations

Calculations were performed at three burnup steps based on a full core model for investigating the dependence of cycle burnup on the APSD of the ex-core noise. In all calculations, the frequency of 8 Hz was selected since it corresponds to the frequency of fuel assembly vibrations in the core [9, 10]. To evaluate the hypothesis that the APSD of the ex-core noise increases throughout the cycle, the calculations of the ex-core scaling factors and the phases have been performed for various locations of the vibrating assemblies in the core using CORE SIM. From this the APSD of the noise can be obtained as in Eq. (2.14). Due to the symmetrical properties of the core, it is not necessary to perform the calculation for the vibrations of every single assembly in the core. The detailed calculations were performed only for the individual vibrations of fuel assemblies located in 1/8th of the core close to detector N2 as shown in Fig. 2.1. This is because of the fact that the noise induced by vibrations of a fuel assembly in any given octant of the core, one can find the similar noise induced by another fuel assembly in the corresponding position of another octant by a rotation transformation. Hence, for individual assembly vibration it is sufficient to consider vibrating assemblies located in one octant to map the possible tendencies as functions of the fuel assembly position. In the technical discussion we focus only on the behaviour of the neutron noise at the detector close to the vibrating assembly. However, to evaluate the contribution of vibrating assemblies

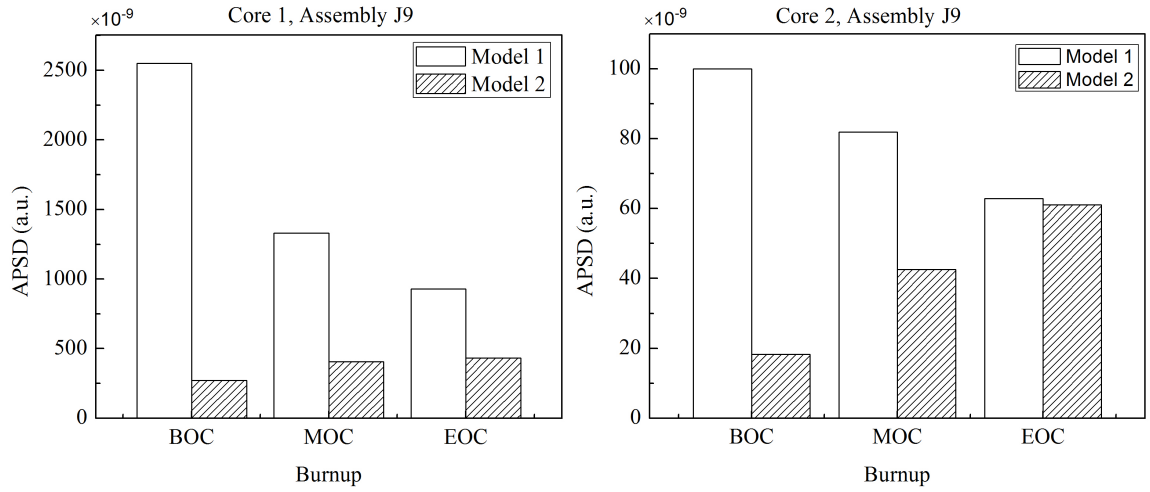

Figure 2.4: APSD of detector N2 induced by vibration of assembly J9 in Core 1 (left) and Core 2 (right), respectively.

at different locations on the ex-core APSD, calculations were also performed with the assumption of a group of assemblies distributed evenly throughout the core vibrating simultaneously and independently.

It is assumed that the core can be classified into three fuel regions from the center to the periphery: the central region, the middle region and the outer region. Fig. 2.4 displays the change of the APSD of detector N2 during burnup with the stochastic vibrations of assembly J9 located in the central fuel region. One can see that the variation trends of the APSDs in the two models regarding the displacement amplitude are different. The APSD decreases with burnup in Model 1 (large displacement) but increases in Model 2 (small displacement). The same behaviour was found in both PWR cores, as shown in Fig. 2.4. Figs. 2.5 and 2.6 show the same quantities as in Fig. 2.4, but for the stochastic vibrations of assemblies K11 and L14 located in the middle fuel region and the outer periphery, respectively. In the vibration of assembly K11, except the APSD in Model 1 in Core 1 which has a peak at MOC, the APSD of detector N2 increases with burnup monotonically. For the vibration of assembly L14, which is located in the periphery of the fuel region, Fig. 2.6 illustrates the increase of the APSD of detector N2 in both of the two models of the noise source, except that of N2 in Model 1 on Core 1 which has a dip at MOC. The vibrations of the three assemblies located in the three different fuel regions in the core show different behaviour of the APSDs of the ex-core noise, i.e. no general monotonic variation of the APSD of the ex-core detector noise can be noticeable. However, for the three assemblies the tendency of the monotonic increase in APSD occurred with Model 2 (small displacement) in both cores, which was also considered as a more realistic model of in-core fuel assembly vibration. In order to reach a conclusion, further survey has been conducted with various locations of fuel in the cores.

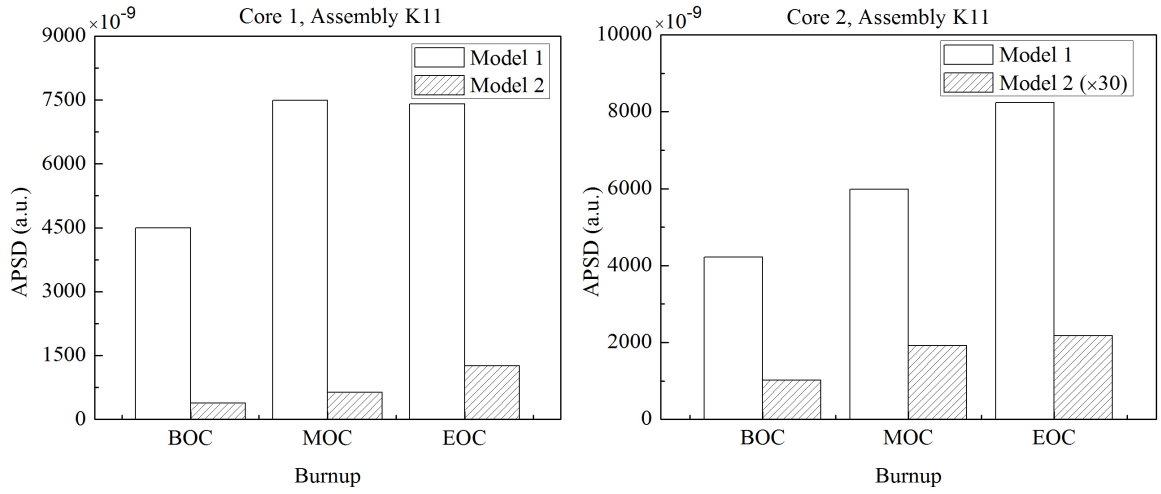

Figure 2.5: APSD of detector N2 induced by vibration of assembly K11 in Core 1 (left) and Core 2 (right), respectively. The values in Model 2 of Core 2 in the lower right figure are multiplied by a factor of 30 for the sake of clarity.

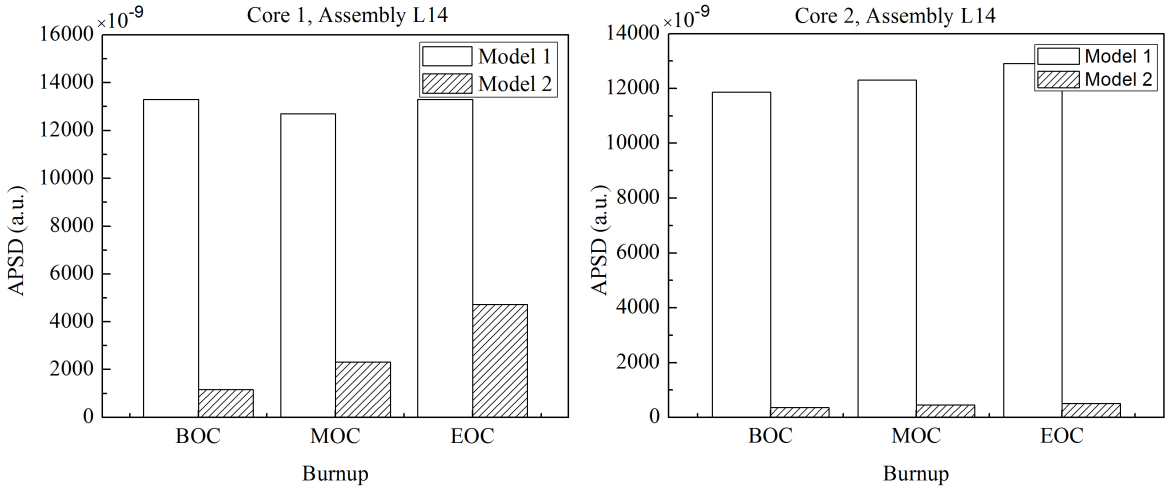

Figure 2.6: APSD of detector N2 induced by vibration of assembly L14 in Core 1 (left) and Core 2 (right), respectively.

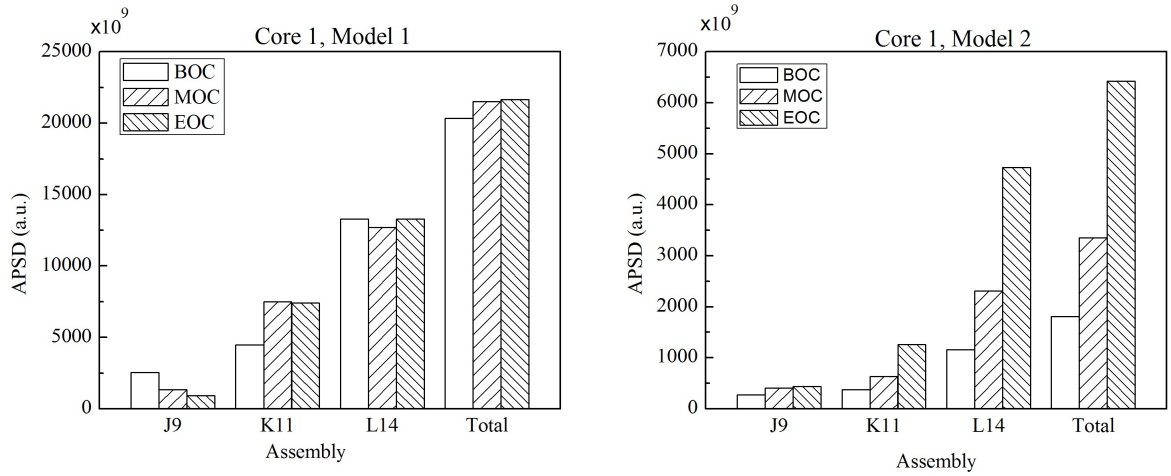

Figure 2.7: APSD of detector N2 induced by simultaneous vibrations of assemblies J9, K11 and L14 in Core 1.

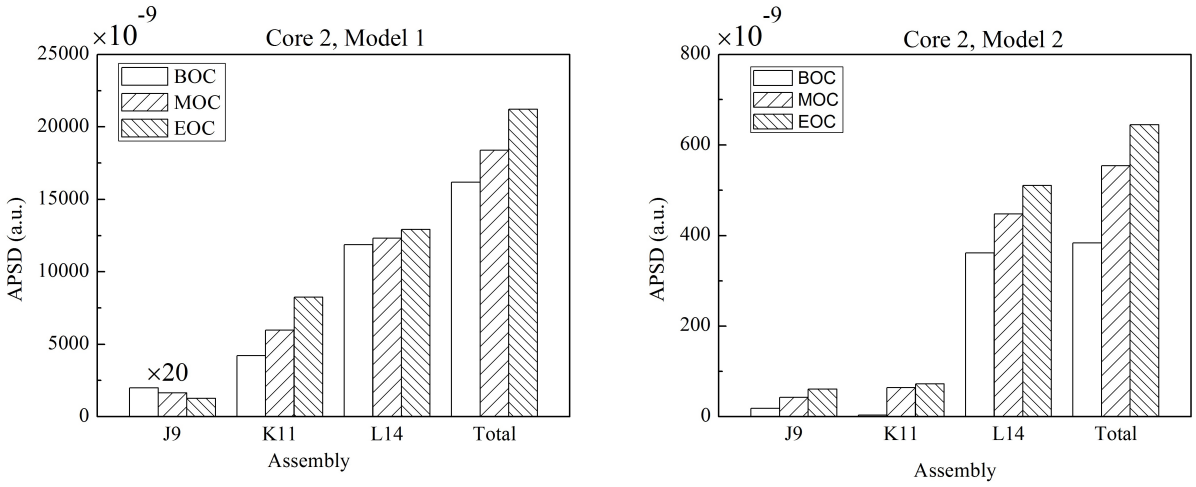

Figure 2.8: APSD of detector N2 induced by simultaneous vibrations of assemblies J9, K11 and L14 in Core 2. The values of assembly J9 in the left figure are multiplied by a factor of 20 for the sake of clarity.

Tables 2.2 and 2.3 show the APSDs of the ex-core detector N2 induced by individual stochastic vibrations of all fuel assemblies located in the 1/8th of the two core models, respectively. One can see that no general monotonic change in the APSDs during burnup cycle was found. Again, the two models regarding the displacement of vibrations result in different behaviour of the APSD of the ex-core noise. In Model 1, the constant decrease in APSD is found in the vibrations of assemblies located around the centre of the core, e.g. assemblies H8 to H12 and assemblies J9 to J11. Whereas, in Model 2 the effect of the central assemblies is not monotonic. The APSDs were found both to increase and decrease. Similarly, no general monotonic variation of the APSD was found with the vibrations of fuel assemblies located in the middle of the core in both PWR cores as shown in Table 2.2 and Table 2.3.

Comparing the effect of different assemblies, the contribution of the peripheral assemblies to the APSD of the ex-core noise is larger than that of the central assemblies, as shown in Table 2.2 and Table 2.3. This means that the ex-core detectors are more sensitive to the vibrations of the fuel assemblies in the periphery. In order to evaluate the contribution of vibrating assemblies at different locations in the core on the ex-core APSD, calculations were performed with the assumption of a group of assemblies vibrating simultaneously and independently. Fig. 2.7 and Fig. 2.8 display the APSD of detector N2 induced by simultaneous vibrations of the three assemblies J9, K11 and L14 in Core 1 and Core 2, respectively. The three assemblies are located in the octant core close to detector N2. One can see that the total APSD of detector N2 is dominated by the vibration of assembly L14, which is located at the periphery close to detector N2. The APSD of detector N2 increases monotonically with burnup in both cores and in both Model 1 and Model 2 of the displacement amplitude. Fig. 2.9 illustrates the APSDs of detectors N1 and N2 induced by simultaneous vibrations of assemblies B5, E9, K6 and L14 in Core 1. Fig. 2.10 displays the same quantities as in Fig. 2.9 but for the Core 2. It is noted that the two detectors N1 and N2 have diagonally opposite positions across the core diameter, while B5 and L14 are located in the peripheries close to N1 and N2, respectively (see Fig. 2.1). The assemblies E9 and K6 are located in the middle fuel region. Again, it is found that the total APSD of N1 is dominated by the vibration of the closest assembly B5, while the contribution of the other assemblies located far from N1 is small, as shown in Fig. 2.9. Conversely, the APSD of N2 is dominated by the vibration of the closest assembly L14. This behaviour is similar in both Core 1 and Core 2.

Thus, we will focus on the effect of some fuel assemblies located at the outer periphery, e.g. assemblies H15, J15, K14, L14 and M13. In Core 1, Table 2.2 shows that out of the five assemblies the vibrations of three assemblies H15, J15 and K14 result in the increase of the APSD of detector N2 in Model 1. In Model 2, the trend of the increase of the APSD was found at four of the five peripheral assemblies (H15, J15, L14 and M13). In Core 2, the increase of the APSD of detector N2 was found at 3 peripheral assemblies in Model 1 (J15, K14 and L14) and two in Model 2 (J15 and L14) as shown in Table 2.3. This means that the trend of increase in the APSD with burnup is predominantly with the peripheral assemblies. However, this tendency is also not monotonic with every peripheral assembly.

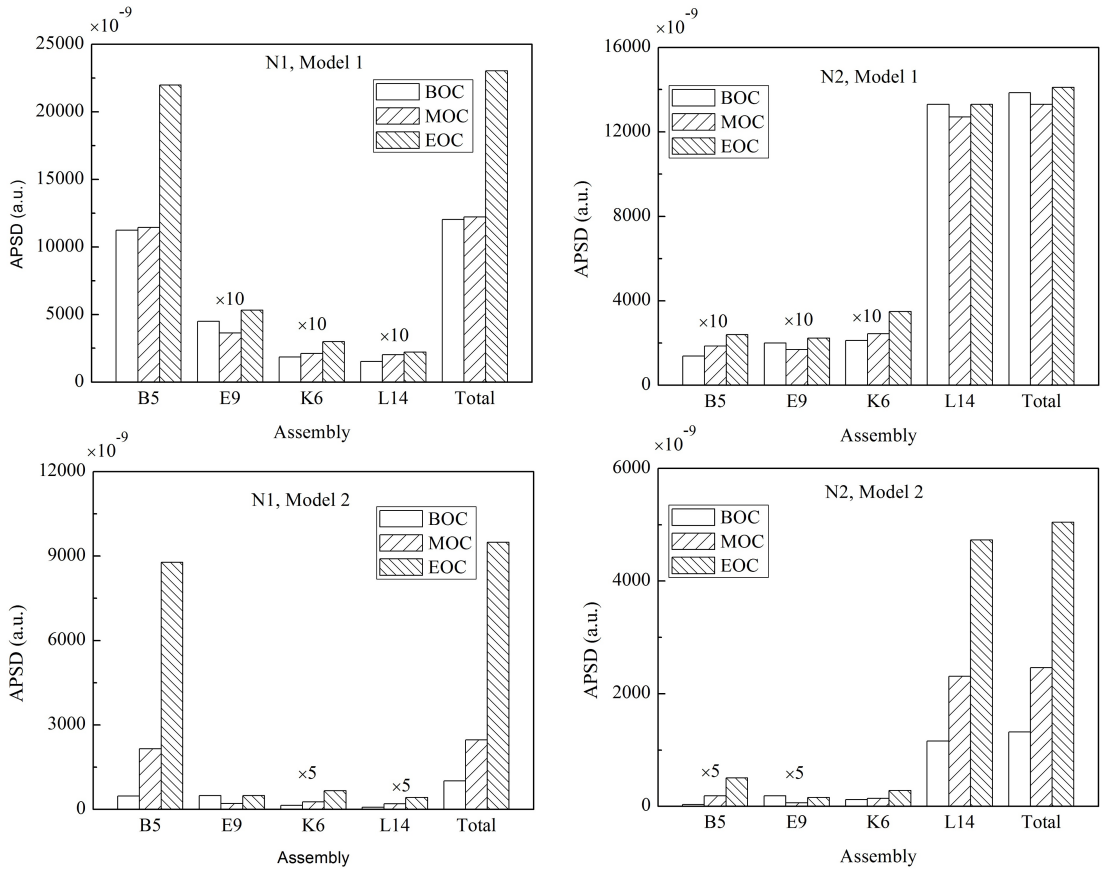

Figure 2.9: APSD of detector N2 induced by simultaneous vibrations of assemblies B5, E9, K6 and L14 in Core 1. The values of some assemblies are multiplied by a factor for the sake of clarity.

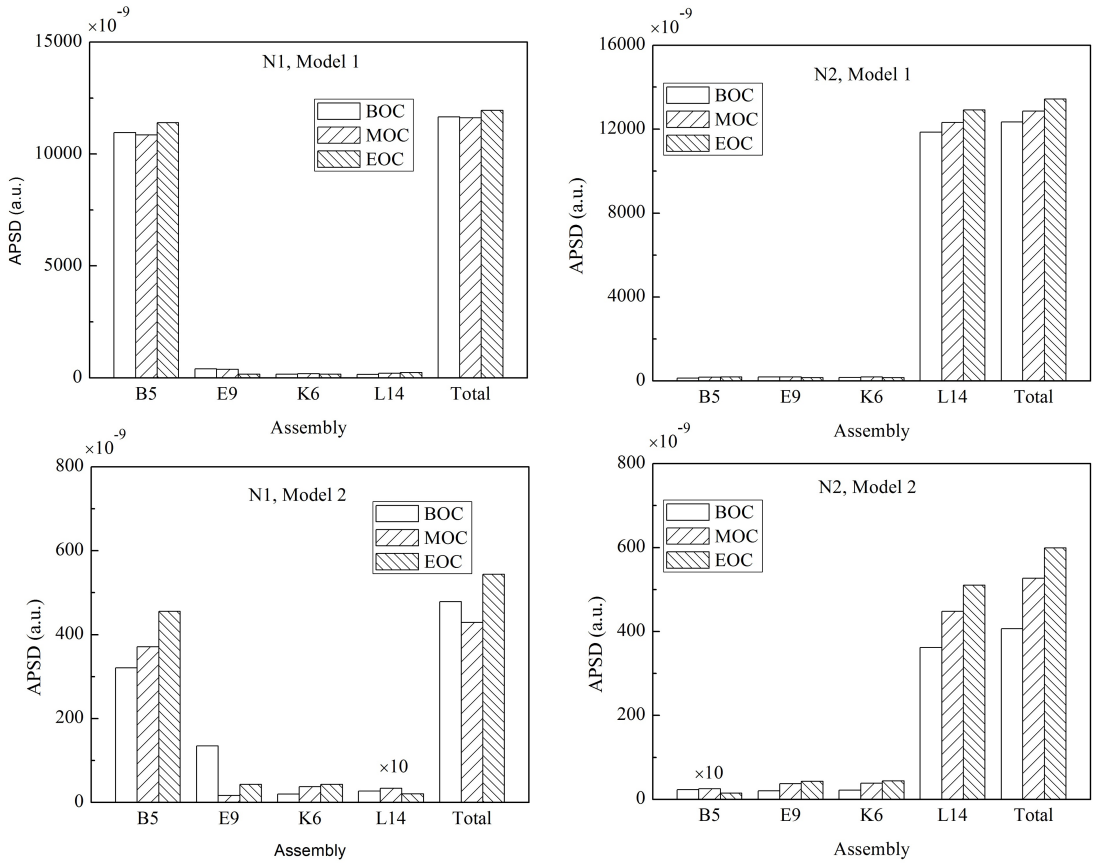

Figure 2.10: APSD of detector N2 induced by simultaneous vibrations of assemblies B5, E9, K6 and L14 in Core 2. The values of some assemblies are multiplied by a factor for the sake of clarity.

Table 2.2: APSD ($\times 10^{-9}$) (a.u) of detector N2 induced by stochastic fuel vibrations in Core 1 at BOC, MOC and EOC, respectively.

	Model 1			Model 2		
Assembly	BOC	MOC	EOC	BOC	MOC	EOC
H8	166	69.7	44.3	0.4	12.8	29.9
H9	1290	433	261	646	324	321
H10	149	66.4	46.8	151	184	238
H11	108	60.2	43.3	334	339	447
H12	2420	1820	1530	293	406	539
H13	73.1	247	245	37	53.2	99.2
H14	2460	2610	2210	4390	3840	3490
H15	979	1650	1750	671	1590	2980
J9	2550	1330	930	272	406	434
J10	201	259	195	53.2	253	378
J11	1580	1270	1010	185	575	864
J12	944	2190	2210	256	466	807
J13	897	1190	1250	120	131	258
J14	339	71.2	137	8700	7760	7610
J15	1160	1930	2650	373	996	2300
K10	1740	2000	1610	759	1770	2110
K11	4490	7490	7410	377	634	1260
K12	1370	1570	1360	2430	3090	4260
K13	1080	1020	1060	183	170	194
K14	2870	3600	5070	19600	14300	13700
L11	151	217	322	4770	4680	6290
L12	5470	1750	1670	358	507	987
L13	997	767	636	4640	3580	3460
L14	13300	12700	13300	1160	2310	4730
M12	289	94.4	97.1	1370	691	374
M13	18700	13800	10300	981	1510	2330

2.4 Conclusions

Extension of the calculation model and method used in a previous work [2] has been conducted for investigating the effect of the vibrations of individual fuel assemblies on the ex-core detector noise as a function of burnup and for confirming the results obtained with Ringhals-3 PWR core. The calculations were based on the 2D models of the two PWR cores which have different fuel arrangements represented by the different neutron flux distribution and its evolution with burnup. Stochastic vibrations of individual assemblies were assumed with the two models regarding the displacement amplitude of the vibrating assemblies. Analysis of the results shows that no general monotonic variation of the APSD of the ex-core detector noise with burnup was found in both cores. In the case of simultaneous vibrations of several

Table 2.3: APSD ($\times 10^{-9}$) (a.u) of detector N2 induced by stochastic fuel vibrations in Core 2 at BOC, MOC and EOC, respectively.

	Model 1			Model 2		
Assembly	BOC	MOC	EOC	BOC	MOC	EOC
H8	12.5	6.5	4.5	15.5	8.7	12.0
H9	420.7	224.3	146.4	4.2	1.7	1.3
H10	108.9	53.5	31.9	157	61.2	86.6
H11	90.6	57.1	44.4	48.7	22.5	45.4
H12	622.2	488.9	436.7	413.3	211.1	241.0
H13	305.3	358.8	251.1	10.4	19.1	17.7
H14	464.5	518.6	262.4	1575.9	952.1	781.6
H15	1438.1	2406.8	2342.7	18.0	16.2	1.3
J9	99.9	81.9	62.9	18.3	42.6	61.1
J10	86.5	44.7	8.9	32.2	18.1	44.5
J11	1783.4	1581.6	1320.7	51.3	265.9	350.5
J12	581.8	1557.6	2208.2	15.7	4.3	9.3
J13	1305.3	1635.0	1966.8	36.6	86.9	126.1
J14	117.8	32.9	171.6	1945.9	1043.8	1278.9
J15	982.6	1560.3	2414.1	23.4	61.4	162.7
K10	1407.6	1635.1	1302.9	421.5	627.9	660.4
K11	4218.1	5981.6	8241.7	3.4	64	72.6
K12	738.7	820.8	761.9	752.5	687.0	1031.0
K13	1047.3	1071.3	1175.9	51.4	23.6	22.1
K14	3082.9	3716.3	5739.4	4019.1	1590.5	1058.2
L11	167.5	166.6	339.2	1672.2	979.6	1648.8
L12	6718.8	3405.8	2362.6	581.6	147.6	16.4
L13	1131.0	920.6	812.7	1487.2	904.4	939.6
L14	11860.9	12312.6	12916.0	361.9	447.8	510.5
M12	274	175	180	90	97	84
M13	17831	13849	9912	2148	2335	2254

assemblies distributed throughout the core, the noise induced by the peripheral assemblies dominates the ex-core detector signals. This behaviour is similar in both cores. The trend of the noise amplitude increase with burnup is predominant for fuel assemblies located at the periphery of the two cores. The result is supportive of the conclusions based on Ringhals-3 core in the previous work.

Since there are still a number of limitations of the simulation models used in the present works, further improvements and investigations should be conducted in order to arrive to more concrete conclusion regarding the questions on the fuel assembly vibration.

3. FURTHER INVESTIGATION OF THE POINT KINETIC COMPONENT OF THE NOISE INDUCED BY FUEL ASSEMBLY VIBRATIONS

No dedicated simulation work was made specifically for this subject. This is because, in order to do a more detailed and conclusive analysis than in the previous Stages, first the improvement of the coupled coarse-fine mesh CORE SIM-based model had to be performed. This has been made in the present Stage, and reported in the previous Chapter.

The performance and the reliability of the improved method was shown by simulating two different cores. The results were in agreement with the previous investigations, in that the vibrations of a collection of peripherally situated fuel assemblies leads to an increase of the corresponding peak in the ex-core detector signals during the fuel cycle. With the improved model, it will be possible to perform dedicated studies to confirm further whether the peak of the ex-core detector spectra, due to such collective vibrations, is dominated by the reactivity component, as it was seen in previous studies with the course-mesh CORE SIM model. Such a dedicated study may be performed in the later stages of the project.

4. ANALYSIS OF NEW EX-CORE MEASUREMENTS, TAKEN IN R-4 AFTER POWER INCREASE

4.1 Introduction and background

The analysis of core-barrel vibration properties (often abbreviated to CBM, core barrel motion) have been the subject of study both in Sweden and internationally It has also been the subject of the collaboration between Chalmers and Ringhals from the beginning, as it was reported in several previous Stages in the Ringhals diagnostic project [11, 12, 13, 14, 15, 16, 17, 18, 19, 1],

Within the last decade, a series of studies dedicated to core barrel vibrations have been performed in order to analyse and find a suitable explanation for the recent observations of wear at both the lower and upper core-barrel-support structures, i.e. the lower radial key and the reactor vessel alignment pins in the Ringhals PWRs. In the last few years the main focus in this area was put on the investigation of a double peak observed in the Auto Power Spectrum in the frequency region of the beam mode component. A hypothesis was formulated about the nature of this peak, where it was suggested that the lower frequency peak is due to the beam mode vibrations and the upper peak is due to fuel assembly vibrations. A test of this hypothesis was one the main target of the analysis. A key factor of the analysis was to assume that the lower frequency peak is due to the (coherent) vibrations of the whole core barrel, hence the symmetries between the ex-core detectors could be used to enhance the effect, as well as to condense the quantification to one single parameter by taking combinations of the detector signals. However, the higher frequency mode was assumed to be due to the effect of the independent (incoherent) vibrations of the individual fuel assemblies, hence no symmetries could be utilised, and the results could not be condensed into one single parameter.

In 2014 a further, new assumption was made, in that the main effect of the individual vibrations manifests itself through the combined reactivity effect of all the individually vibrating fuel assemblies. This assumption, through the associated symmetries of the reactivity component, allowed to condense the analysis of the different detector signals into one single parameter even for the higher frequency peak. This hypothesis was tested with a fruitful outcome on the measurements taken at Ringhals-4. Thus, finally, it became possible to distinguish between the beam mode component due to core barrel vibrations and reactivity component associated to the single fuel assembly vibrations. In addition, it was also possible to confirm the constant amplitude within one fuel cycle for the beam mode component, and the varying amplitude (within one cycle) of the reactivity component (individual fuel assembly vibrations), which were in very good agreement with the original hypothesis.

The work in the continuation was therefore not concentrated any longer on the test and proof of the hypothesis, and the associated trend analysis of the evolution

of the peak amplitudes during the cycle, rather on checking whether there is any major change in the amplitude and frequency of the beam mode peaks, as compared to the previous measurements, which could indicate an increased play in the lower radial key support. A special circumstance in this aspect is that in 2015, the total power of Ringhals-4 was increased by 18.6 %. Therefore, it was natural to perform a routine analysis on a new set of measurements in order to investigate the effect of power increase on the measured neutron noise, in particular core barrel and fuel assembly vibrations and associated vibrations components (beam, shell, and reactivity modes).

Another aspect, which is worth mentioning since it affects the vibration properties, and hence the analysis and interpretation of the measurements, is that some structural changes took place in R4 relatively recently. The hold-down springs were replaced during the outage in 2013, and the interior parts were lifted out during the outage in 2014 for an inspection. These modifications, including the moving of the internal parts, affect the vibration properties, in particular the separation of the 7 and 8 Hz peaks, as will be seen in the forthcoming.

Last but not least, as it was described in the previous stage [1], a new type of pivotal vibration mode, which we named as "tilting" or "wobbling" mode, was discovered. The separation of the tilting mode from the other components is made with methods similar to the other mode separation methods with adding and subtracting the signals in various combinations. The only difference is that for the separation of the tilting mode from the other components, all 8 detectors (the four ex-core detectors at two axial elevations) need to be used. Hence in the routine analysis, the separation of all four components (beam, shell, reactivity and tilting modes) were made, and this is included into this Section. In connection with the tilting mode, some method development took also place, which is described in the next Section, and the Appendix.

4.2 Details of the measurements in R4

Three sets of measurements were analysed. The measurements were performed in R4 in cycle C34, on 22 November 2016, as well as 7 March and 20 June 2017, and for simplicity will be referred to a Measurement 1, 2 and 3 respectively. The sampling frequency was 62.5 Hz for all three sets of measurements. The measurement points are shown in Table 2. More detailed data regarding settings and general parameters can be found in the measurement protocols from previous measurements, which were performed in an identical manner [20, 21, 22]. Some sample spectra, showing the APSD for each of the 8 individual ex-core detectors, calculated from the corresponding measurement will be presented in the next section.

4.3 Analysis of the measurements made on 2016-11-22 (Measurement 1)

4.3.1 Individual spectra of all detectors

The APSDs of all eight individual detector signals are shown in Fig. 4.1. All signals show the two familiar peaks around 8 and 20 Hz for the beam and shell

Table 4.1: The measurement data of the three measurements in Ringhals 4 during 2016-17

Channel	**Measurement point**
0	Time
1	N41U DC
2	N42U DC
3	N43U DC
4	N44U DC
5	N41L DC
6	N42L DC
7	N43L DC
8	N44L DC
9	N41U AC
10	N42U AC
11	N43U AC
12	N44U AC
13	N41L AC
14	N42L AC
15	N43L AC
16	N44L AC

modes, respectively. The structure of the double peak at 8 Hz looks different from those in the previous cycles. The lower frequency peak is at 6 Hz, i.e. much more separated from the 8 Hz pesk in frequency, is smaller in amplitude and is wider. The APSD of the total signals, without mode separation, resembles to the structure of the spectra of the tilting modes in the previous stage [1]. On the other hand, the two peaks that can be identified with the beam mode and the reactivity mode (corresponding to the noise induced by the individual fuel assembly vibrations) cannot be visibly separated. This will be reflected in the detailed analysis below. As mentioned before, this change in the character of the spectra, as compared to the previous measurements, may be due to the change of the hold-down spring and that the structural conditions for the internal components might be changed after the lifting out and putting back them into the pressure vessel.

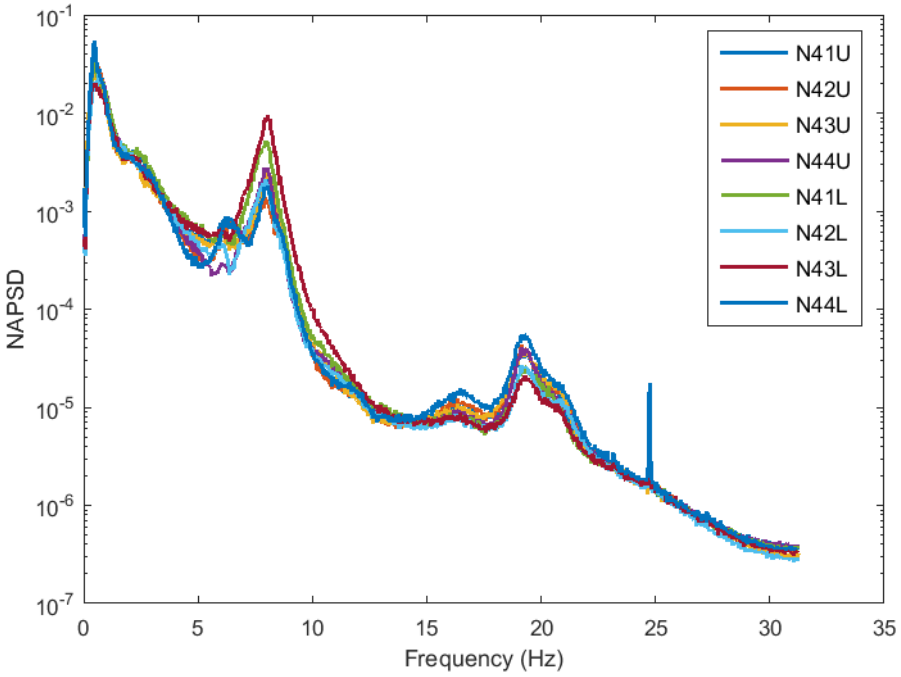

Figure 4.1: APSD of all 8 ex-core detector signals from Measurement 1

.

4.3.2 Results of the mode separation

The beam mode, shell mode, reactivity component and the tilting modes were separated according to the detector signal combination principles as in the previous work. The results are shown for the upper detectors in Fig. 4.2, and for the lower detectors Fig. 4.3. The result of the separation is rather similar for the two cases. It is seen that the amplitude of the beam mode is larger for the lower detectors, as expected, whereas the amplitude of the other components is very similar for the upper and lower detectors. The frequency of the reactivity mode is somewhat higher than that of the beam mode, confirming that they can be identified as Mode 2 and Mode 1 in the previous terminology. Hence the results are in agreement with the

results from the previous stages.

It is worth to note a small peak around 16 Hz in both the upper and the lower detector signals. According to the mode separation technique, this peak is due to a reactivity effect. It is interesting to observe that its frequency is twice that of the pendular fuel vibration frequency at 8 Hz, itself also identified as a reactivity effect. Hence the peak at 16 Hz can be attributed to the higher harmonics of the fuel assembly vibrations at the fundamental frequency 8 Hz.

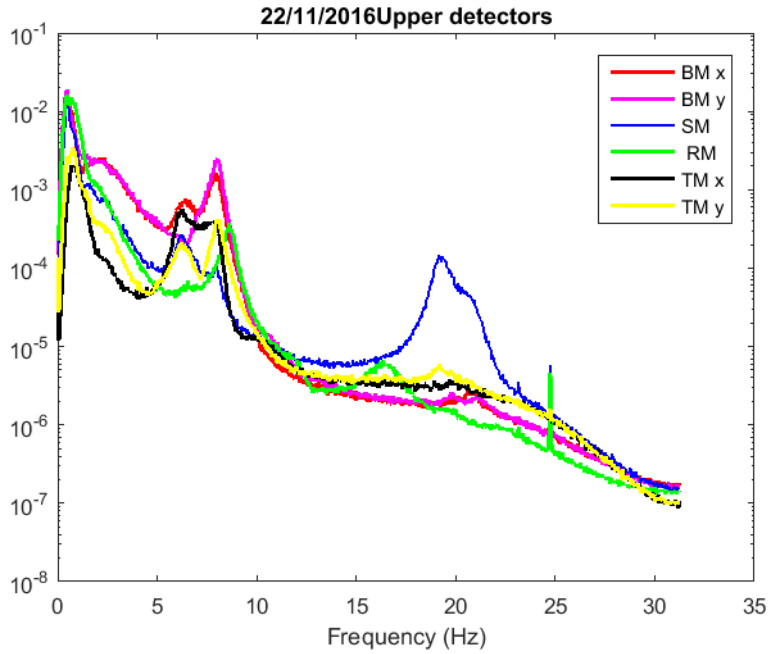

Figure 4.2: APSDs of the beam mode, shell mode, reactivity component and the tilting mode for the upper detectors, extracted from Measurement 1.

4.3.3 Phase and coherence relationships between the upper and lower detectors

An analysis of the coherence and the phase relationships between detectors at the same and different axial levels was performed, similarly to that in the previous stage. The coherence and phase between the diagonally opposite detectors N41 and N42, for both the same and different axial levels, is shown in Fig. 4.4, and the same for detectors N43 and N44 in Fig. 4.5. The coherence and phase between the upper and lower detectors at the same radial position, for all four detectors, is shown in Fig. 4.6.

As it can be seen, apart from some minor differences, the structure of all these plots is similar to that of the previous stages, indicating that no major changes took place in the behaviour of the cores. The coherence is high at 8 Hz and 20 Hz, i.e. at the frequencies of the beam mode, the reactivity componponent and the shell mode, and it is lower, but still showing a peak also at 16 Hz, the reactivity component due to the first harmonic of the fuel assembly vibrations around 8 Hz. On the other

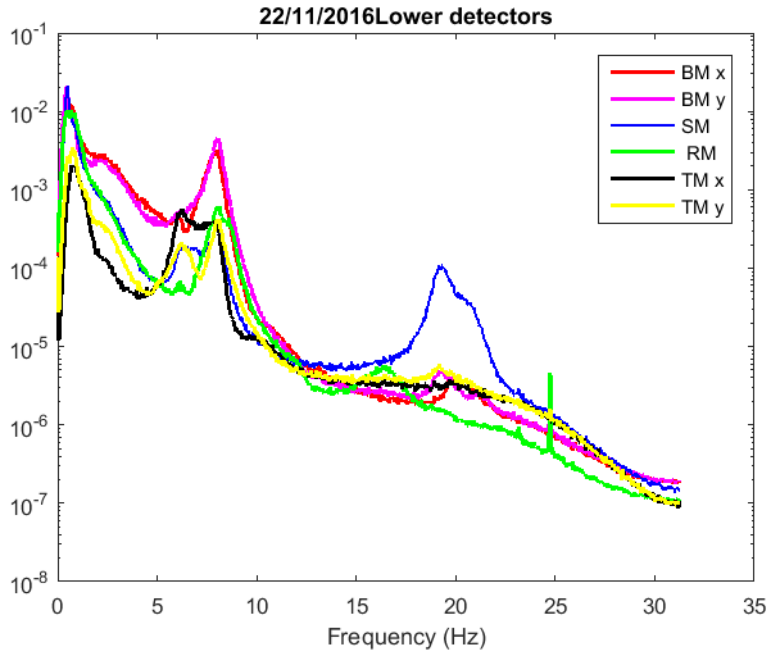

Figure 4.3: APSDs of the beam mode, shell mode, reactivity component and the tilting mode for the lower detectors, extracted from Measurement 1

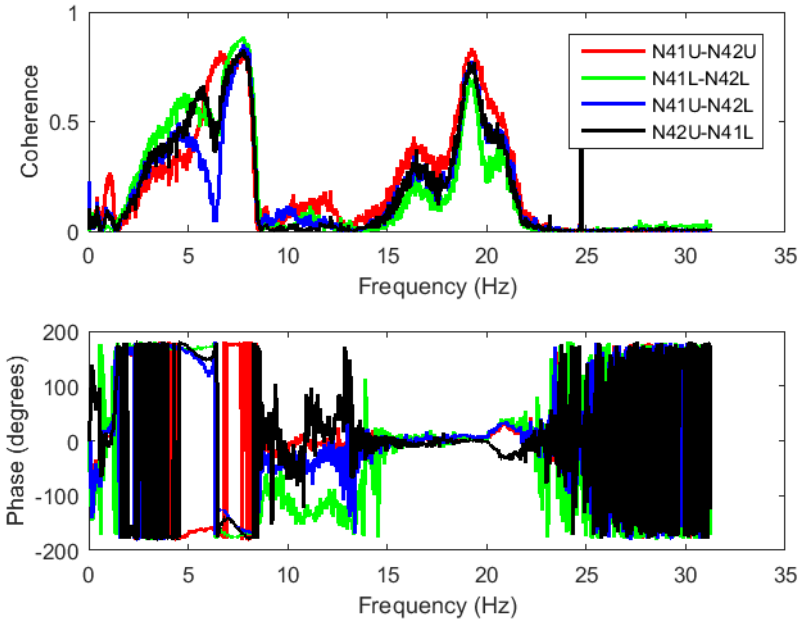

Figure 4.4: The coherence and the phase of the CPSD calculated for the N41U-N42U, N41L-N42L, N41U-N42L and N42U-N41L detector pairs in Measurement 1.

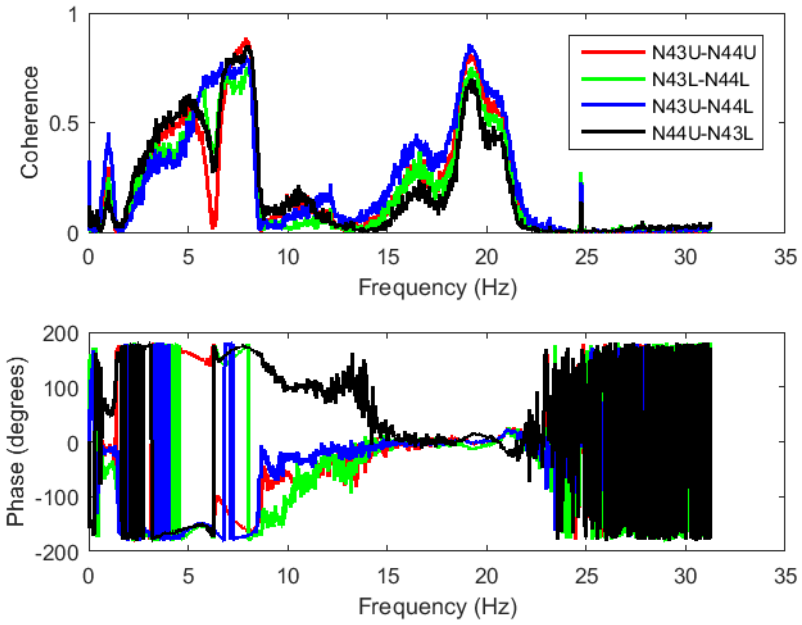

Figure 4.5: The coherence and the phase of the CPSD calculated for the N41U-N41L, N42U-N42L, N43U-N43L and N44U-N44L detector pairs in Measurement 1.

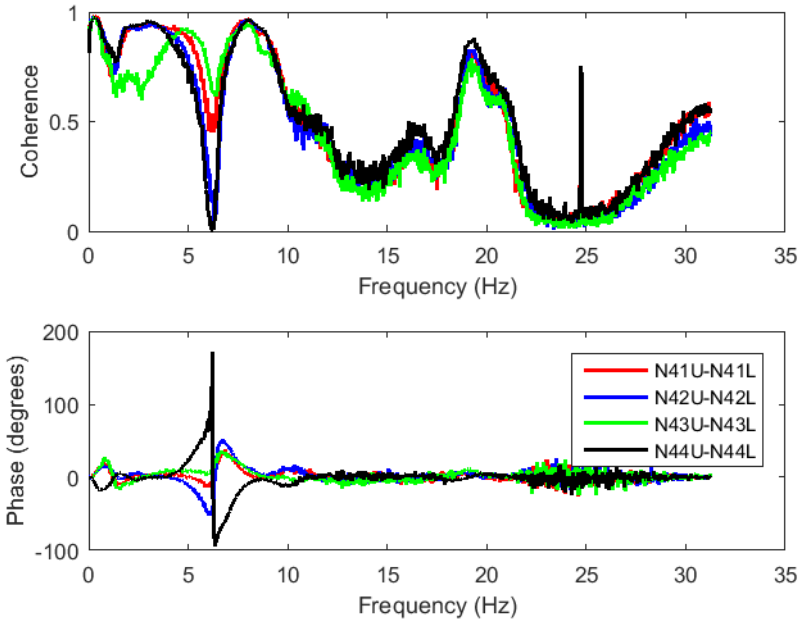

Figure 4.6: The coherence and the phase of the CPSD calculated for the N41U-N42U, N41L-N42L, N41U-N42L and N42U-N41L detector pairs in Measurement 1.

hand, there is a dip at around 6 Hz (except for the pair N41U - N42U), which is the domain where the tilting mode and the beam modes overlap. This dip is the most conspicuous in the coherence between the detector pairs situated above each other, i.e. at the same radial but different axial position.The phase is uniformly zero at 20 Hz for any detector combinations, as expected, and it is 180° at the beam mode. The dip in the phase at 6 Hz though is somewhat different in structure from that in the previous stage [1].

4.4 Analysis of the measurements made on 2017-03-07 (Measurement 2)

4.4.1 Individual spectra of all detectors

The APSDs of all eight individual detector signals are shown in Fig. 4.7. These look very similar to those in Measurement 1. A moderate increase of the amplitude of the 8Hz peak is seen, whereas the peak at 6 Hz is nearly absent.

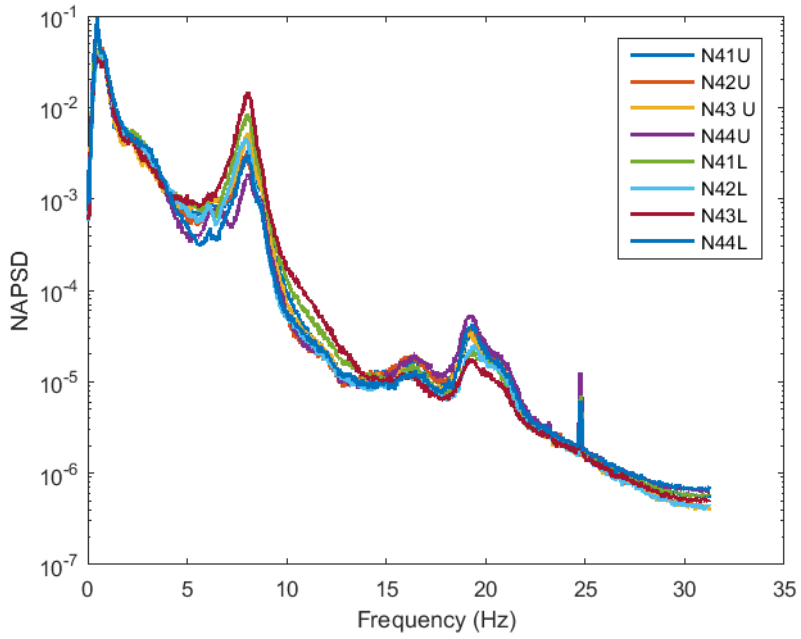

Figure 4.7: APSD of all 8 ex-core detector signals from Measurement 2

.

4.4.2 Results of the mode separation

The results for the separation of the beam mode, shell mode, reactivity component and the tilting modes are shown for the upper detectors in Fig. 4.8, and for the lower detectors in Fig. 4.9. These results are very similar to those of Measurement 1. Like in the prevoius case, the amplitude of the beam mode is larger for the lower detectors, and the frequency of the reactivity mode is somewhat higher than that of the beam mode, as expected.

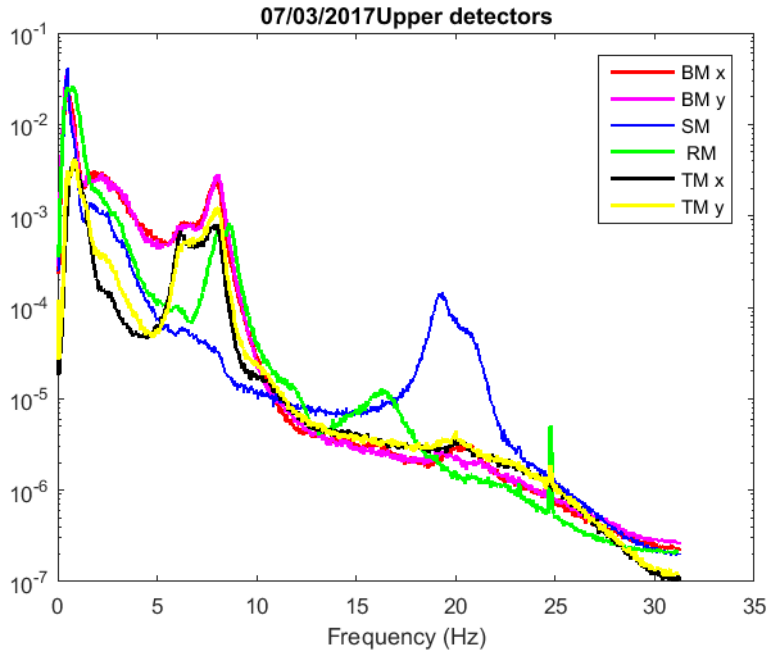

Figure 4.8: APSDs of the beam mode, shell mode, reactivity component and the tilting mode for the upper detectors, extracted from Measurement 2.

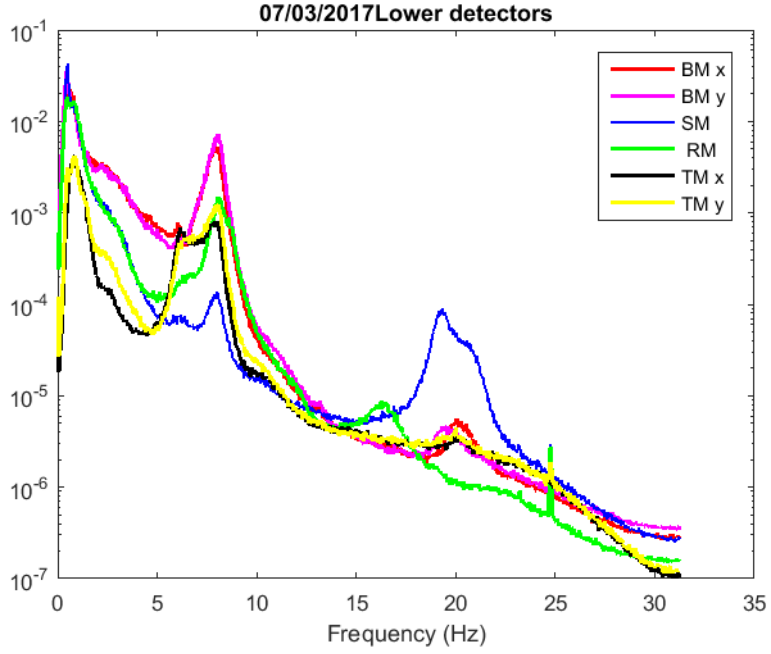

Figure 4.9: APSDs of the beam mode, shell mode, reactivity component and the tilting mode for the lower detectors, extracted from Measurement 2

4.4.3 Phase and coherence relationships between the upper and lower detectors

The coherence and phase between the diagonally opposite detectors N41 and N42, for both the same and different axial levels, is shown in Fig. 4.10, and the same for detectors N43 and N44 in Fig. 4.11. The coherence and phase between the upper and lower detectors at the same radial position, for all four detectors, is shown in Fig. 4.12.

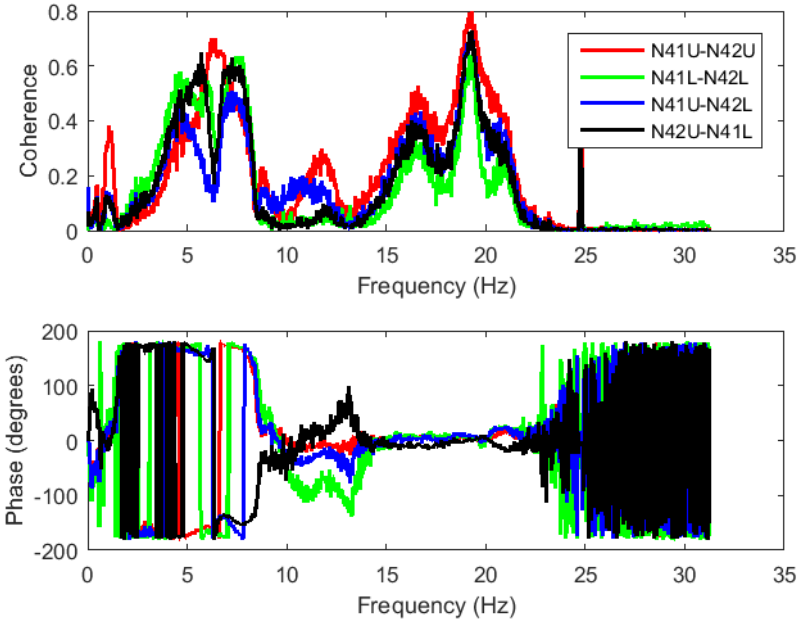

Figure 4.10: The coherence and the phase of the CPSD calculated for the N41U-N42U, N41L-N42L, N41U-N42L and N42U-N41L detector pairs in Measurement 2.

These plots again show a full resemblance to those in Measurement 2. One difference is that in the beam mode, the dip is now missing not only for the pair N41U - N42U, but also for N43U - N44U. Also the behaviour of the phase at 6 Hz for the axial pairs at the same radial position has changed somewhat. For the rest there are no noticeable differences.

4.5 Analysis of the measurements made on 2017-06-20 (Measurement 3)

4.5.1 Individual spectra of all detectors

The APSDs of all eight individual detector signals are shown in Fig. 4.13. These look very similar to those the previous two measurement, somehow being a little 'in between". On one hand, the amplitude of the 8Hz peak has increased further, whereas the peak at 6 Hz is larger than in Measurement 2, but smaller than in Measurement 1.

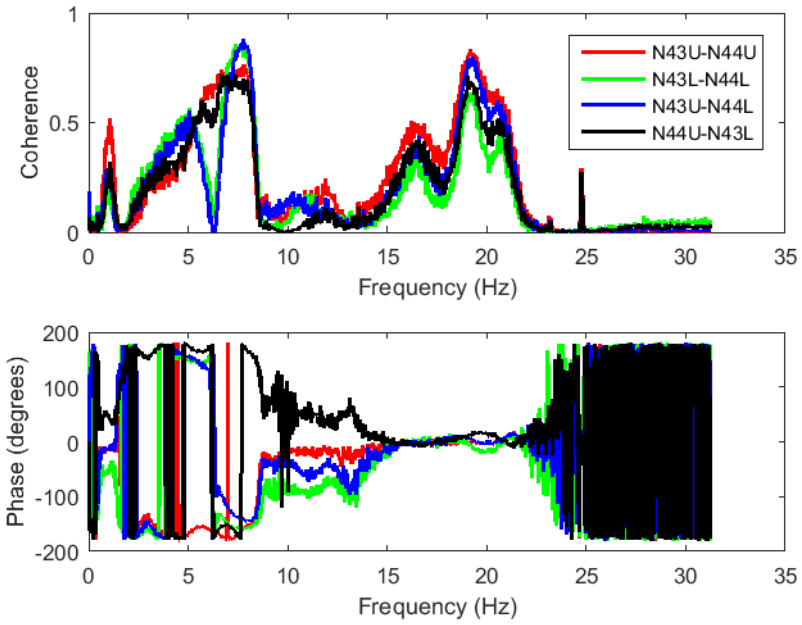

Figure 4.11: The coherence and the phase of the CPSD calculated for the N41U-N41L, N42U-N42L, N43U-N43L and N44U-N44L detector pairs in Measurement 2.

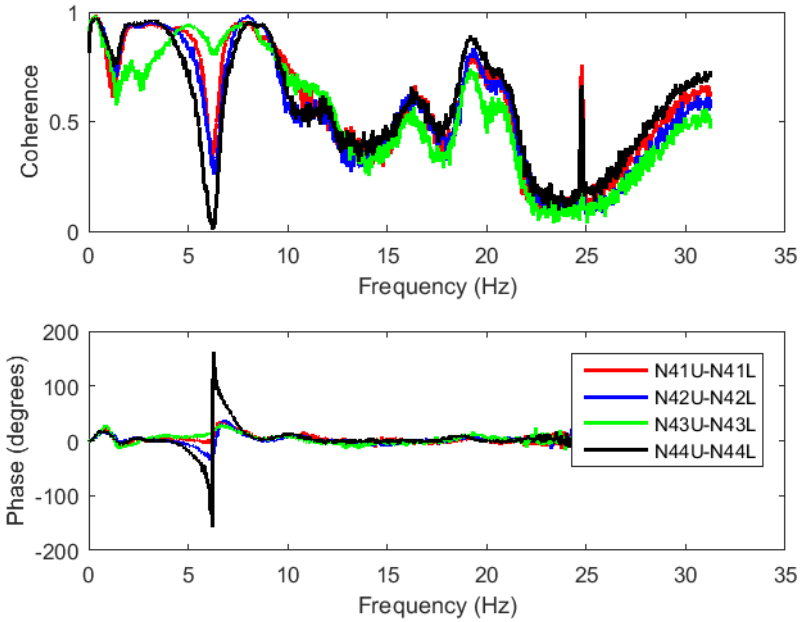

Figure 4.12: The coherence and the phase of the CPSD calculated for the N41U-N42U, N41L-N42L, N41U-N42L and N42U-N41L detector pairs in Measurement 2.

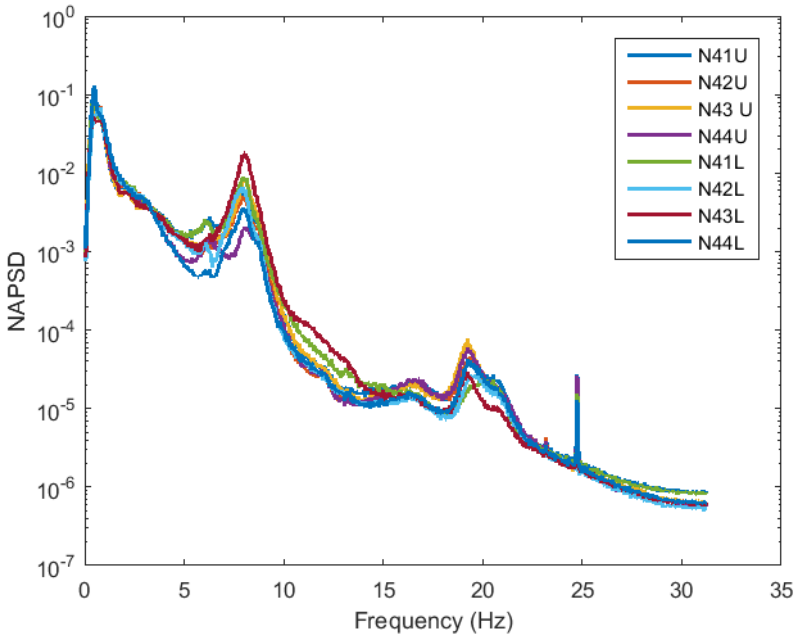

Figure 4.13: APSD of all 8 ex-core detector sigals from Measurement 3

.

4.5.2 Results of the mode separation

The results for the separation of the beam mode, shell mode, reactivity component and the tilting modes are shown for the upper detectors in Fig. 4.14, and for the lower detectors in Fig. 4.15. One difference as compared to the previous measurements is that the double peak structure of the beam and the tilting modes, which could be seen in those, is much less visible in this last measurement.

4.5.3 Phase and coherence relationships between the upper and lower detectors

The coherence and phase between the diagonally opposite detectors N41 and N42, for both the same and different axial levels, is shown in Fig. 4.16, and the same for detectors N43 and N44 in Fig. 4.17. The coherence and phase between the upper and lower detectors at the same radial position, for all four detectors, is shown in Fig. 4.18.

Again, apart from some minor differences, the structure of all these plots is similar to the previous two measurements.

4.6 Trend analysis

Since there were three measurements made during the cycle which is the subject of the investigations the present stage, a trend analysis for the three measurements could be made. However, only the fitting for the beam mode component gave reliable results; this is illustrated in Fig. 4.19 for both the upper and the lower detectors

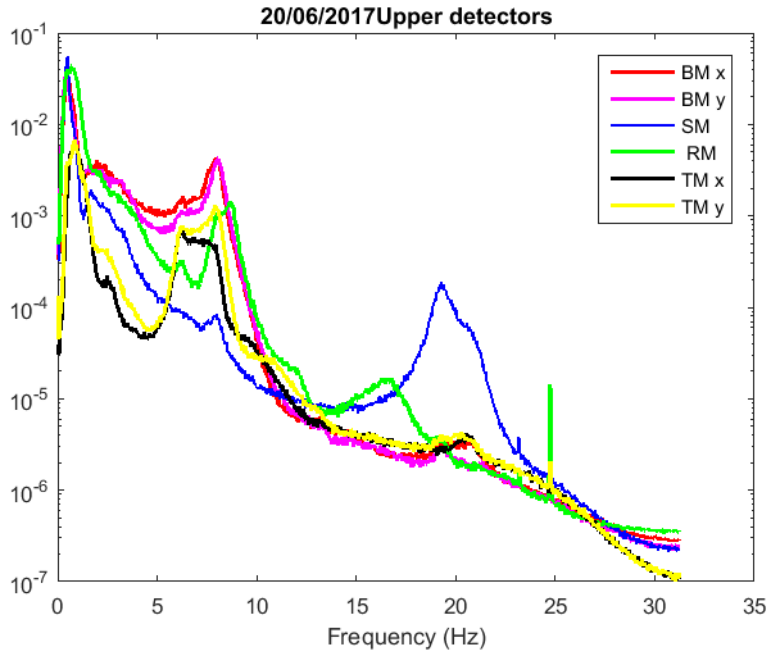

Figure 4.14: APSDs of the beam mode, shell mode, reactivity component and the tilting mode for the upper detectors, extracted from Measurement 3.

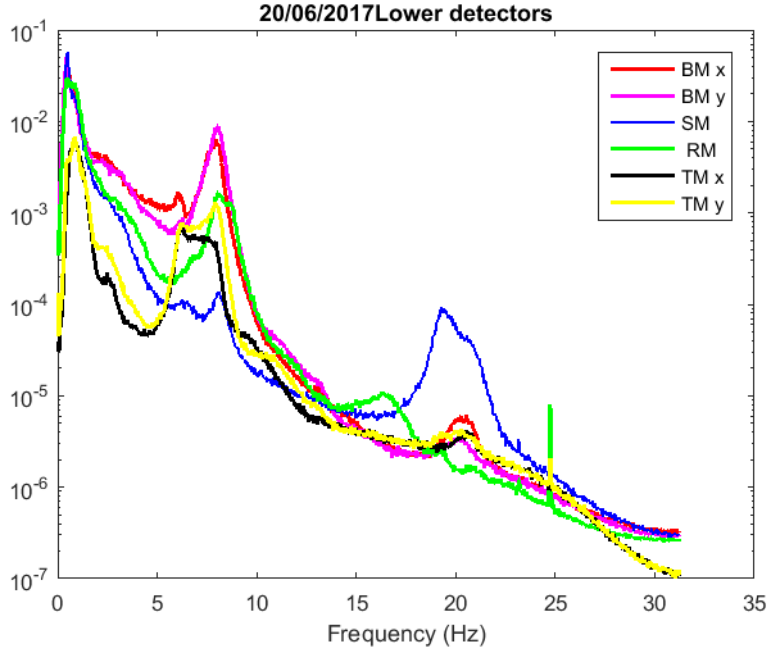

Figure 4.15: APSDs of the beam mode, shell mode, reactivity component and the tilting mode for the lower detectors, extracted from Measurement 3

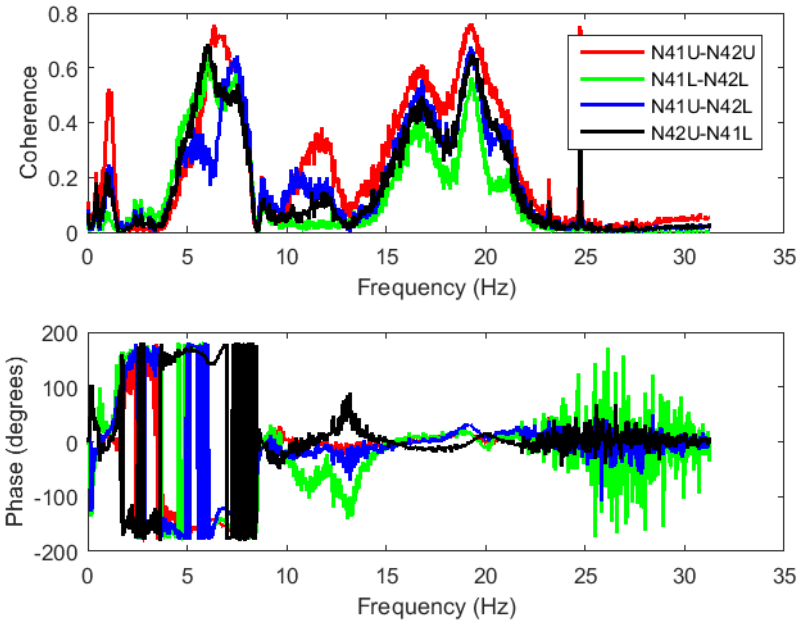

Figure 4.16: The coherence and the phase of the CPSD calculated for the N41U-N42U, N41L-N42L, N41U-N42L and N42U-N41L detector pairs in Measurement 3.

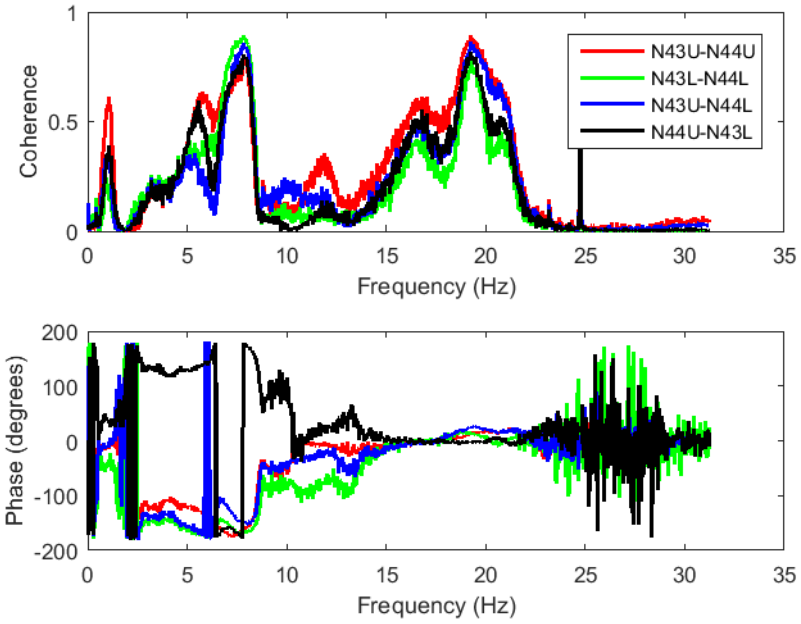

Figure 4.17: The coherence and the phase of the CPSD calculated for the N41U-N41L, N42U-N42L, N43U-N43L and N44U-N44L detector pairs in Measurement 3.

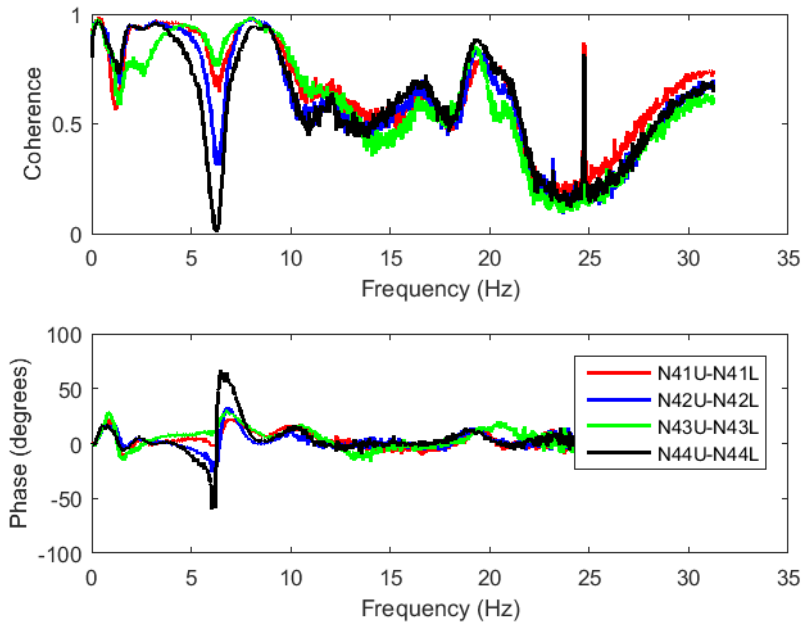

Figure 4.18: The coherence and the phase of the CPSD calculated for the N41U-N42U, N41L-N42L, N41U-N42L and N42U-N41L detector pairs in Measurement 3.

from Measurement 1. The fitting procedure for the reactivity component, which since 2014 we have associated with Mode 2, became unstable, and did not yield reliable results. The most likely reason is that during this cycle, the frequencies of the two modes Mode 1 and Mode 2 lie too close to each other, and the behaviour of the spectra was dominated by Mode 1 which had much larger amplitude than Mode 2. The reason why the frequency structure of the modes was changed was already motivated by the mechanical changes and rearrangements in 2013 and 2014, as described earlier.

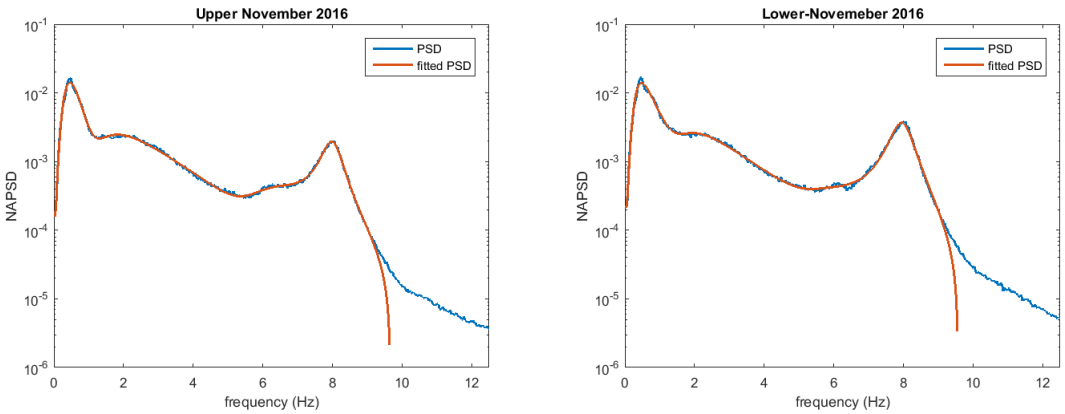

Figure 4.19: Results of the curve fitting to the peak at 8 Hz (beam mode) for Measurement 1 for the upper (left figure) and the lower (right figure) detectors.

Therefore, a trend analysis was made only for the beam mode component, and

the result is shown in Fig. 4.20.

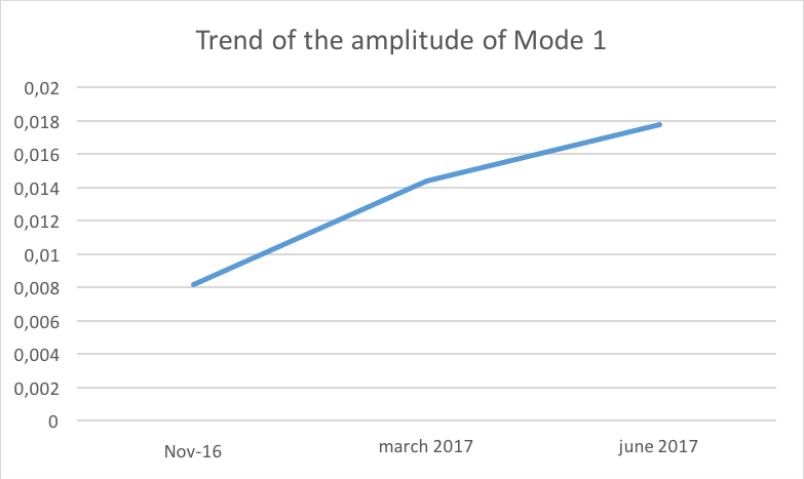

Figure 4.20: Trend analysis of the amplitude of the beam mode at 8 Hz for the three measurements made during the cycle.

It is seen that the amplitude of the beam mode has increased appreciably during the cycle. This is the behaviour that we expect, and have seen earlier, from Mode 2, i.e. the reactivity component, and not from the beam mode component, which was assumed to be more or less constant. However, as mentioned, in this cycle the mode separation method was not reliable, and hence what we identify as the beam mode, is presumably "contaminated" with the noise from the vibration of the individual fuel assemblies, manifested by the reactivity effect. In summary, the trend analysis did not give unambiguous results in the present cycle.

5. FURTHER DEVELOPMENT AND TEST OF THE MODE SEPARATION MODEL AS APPLIED TO 3-D "WOBBLING" TYPE OR "TILTING" TYPE CORE-BARREL VIBRATIONS

The development and test of the mode separation model to detect and confirm the existence of tilting mode vibrations was performed in several stages. As a test of the algorithm, already developed in the previous stage and applied to the R4 measurements, another measurement, made in R2 in 2014, was evaluated, in order to detect and quantify tilting mode vibrations. The result of the analysis was that there was no evidence of tilting mode vibrations seen in the measurements. Since it was only a singular measurement, it does not necessarily mean that tilting mode vibrations do not exist in R2. However, it would not be surprising if there were no tilting mode vibrations of the core barrel in R2, due to the different constructional properties of R2 as compared to R3 and R4.

Another development line was to try to apply a new type of mode separation method, based on the so-called "Variational Mode Decomposition (VMD) Method". This method was brought to us through our visitor, Omar Alejandro Olvera-Guerrero, currently PhD student at the UAM/Autonomus Metropolitan University, Mexico City, Mexico. His advisers, Alfonso Prieto Guerrero and Gilberto Espinosa Paredes, are internationally known experts in non-linear analysis of BWR stability, and in the corresponding analysis methods of resonance peaks, which has some methodological resemblances to the mode separation method we use for separating the various vibration components in the ex-core neutron detector spectra.

Omar Alejandro Olvera-Guerrero stayed at our department between 11 January - 10 July 2017, and worked on the development of the method and its test to the analysis of the current measurements in R4. As it turns out, the VMD method is a rather powerful and effective method, with a high sensitivity and resolution. This incurs that it will identify a large number of modes and separate many spectral peaks, but it requires familiarity with the concrete case and expertise to filter out non-physical peaks, identified by the algorithm. The short time, and lack of experience with the method at Chalmers did not allow to draw concrete conclusions from the analysis. However, in order to archive the effort, as well as for information about the principles and details of the VMD method, a draft report, written by Omar Alejandro Olvera-Guerrero is enclosed at the end of this research report, in Appendix.

Finally, based on the previous development and analysis, a journal publication is prepared about the first evidence of the tilting mode in the Ringhals measurements. A first, incomplete draft of this coming journal publication is enclosed here below, completing this Chapter.

Draft of the planned publication
"SEARCHING FOR EVIDENCE OF THE "TILTING MODE" OF THE CORE BARREL IN THE RINGHALS-4 PWR"
by C. Montalvo, I. Pázsit, H. Nylén and V. Dykin

Abstract

The Nuclear Engineering Group of the Division of Subatomic Physics and Plasma Physics (formerly Division of Nuclear Engineering) in Chalmers, Göteborg, and the Ringhals Nuclear Plant have investigated the core barrel vibrations in the Ringhals PWRs over the last 20 years. Based on the different symmetry properties of the vibration modes, a mode separation technique was developed to enhance the contributions from the different modes. Recent observations of wear at both the lower and upper core-barrel-support structures in the Ringhals PWRs indicated that vibration modes of the core barrel other than pendular (beam mode) and shell mode are likely to occur. A beam mode type movement alone is not able to explain such a wear, and therefore, it is fair to assume that the vibration mode in question is a small amplitude periodic tilting movement of the core barrel around a horizontal, diagonal pivot at the half height of the core. In this work, ex-core data taken in the Ringhals-4 PWR were analysed in order to find evidence of such a tilting movement. First, cross spectra between various ex-core detectors were calculated and analysed to locate the frequency range of the new vibrational mode. Then, a model based on symmetry considerations was derived in order to extract the sought mode from the spectra. The measurements were evaluated by the new mode enhancement technique. The results show that it is possible to enhance such a mode and find it in the spectra by properly combining the signals in the time domain.

Key Words: Beam mode, tilting, ex-core detector, APSD, CPSD

5.1 Introduction

Diagnostics of core barrel vibrations of a PWR can be performed by ex-core neutron detector signals [23]. The signals of these detectors can be analyzed and once the Auto Power Spectral Density (APSD) is obtained, a frequency analysis can be made. In the late 1990's, a method was developed for the separation of the effects of the beam mode (around 8 Hz), shell mode (around 20 Hz), and reactivity terms in the detector signals by making the analysis on three different averaged combinations of the four ex-core detectors at one axial level [24]. The corresponding auto power spectra were calculated on the averaged signal, and the diagnostics of the beam mode vibrations was made on the signal combination corresponding to the symmetry properties of the beam mode with the so-called k-α method [24]. The advantage of the k-α method is that it gives an objective measure of the vibration amplitude, irrespective of the isotropy or anisotropy of the 2D vibration pattern. It was found that the beam mode amplitude increases monotonically during each cycle, and then after refuelling, it starts from the same low level as in the previous cycle. The trend behaviour of the beam mode amplitudes for some past measurements

(spring and autumn 2005 and 2006, spring 2007 and winter 2007/2008) are shown in Fig. 5.1 for Ringhals units 3 and 4.

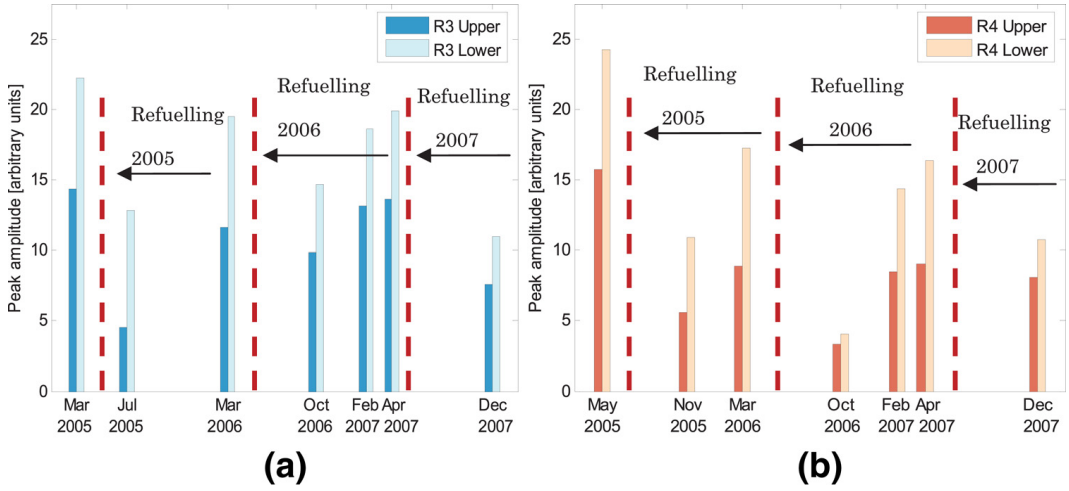

Figure 5.1: Evolution of the peak amplitude of the beam mode for some previous cycles in Ringhals 3 and 4, taken from [10]

.

However, for the trend analysis, the amplitude of the vibration peak was read out manually from the APSD, and hence it was not fully accurate and objective. For this reason, a new development started with applying a curve fitting procedure based on the Breit-Wigner formula by which the amplitude of the vibration peak could be determined more automatically and with better precision. One novelty of the method was a more sophisticated curve fitting procedure, by which strongly overlapping peaks could still be separated. The method came very handy, because, as it has been observed already in the past, in the ex-core detector APSDs, the 8 Hz beam mode peak consists actually of a double peak in the data taken in Ringhals 3 and 4.

By performing both in-core and ex-core measurements, and by studying the development of the amplitudes of the two peaks around 8 Hz separately, a hypothesis was formulated that the double peak corresponds to two vibration modes with different physical origins. According to the hypothesis, the lower frequency peak, called "Mode 1", around 7 Hz, is related to the core barrel motion itself, whereas the higher frequency peak, called Mode 2, around 8 Hz, corresponds to flow induced vibrations of single fuel assemblies.

From previous measurements [16]-[25], out of the two modes, the amplitude of Mode 1 was essentially constant during the cycle, whereas the amplitude of Mode 2 was increasing during the cycle. The increase of the corresponding peak of the detector APSD can be due either to the amplitude increase of the fuel assembly vibrations (which might be due to changed mechanical properties of the fuel pins due to burn-up), or to the change of the conversion factor between mechanical vibrations of fuel assemblies and the induced neutron noise, as measured by ex-core detectors. This latter possibility was suggested by Sweeney et al [7], and its

feasibility was investigated through core physics calculations in Chalmers [26]. The results obtained indicate that the scaling factor between the amplitude of the fuel assembly vibrations and the ex-core neutron noise can indeed increase during the cycle for certain assembly positions and vibration patterns. However, this is not a general trend, and for some other fuel assembly positions and vibration patterns the trend is different. The question of why the vibration peak representing the fuel assembly vibrations increases during the cycle remains unsolved, but is outside of the present project.

5.2 State of the art in beam mode vibrations: Breit-Wigner and enhancing technique in the time domain

The Beam Mode component has been widely researched in many different reactors. It is considered to be related to pendular type motion of the core barrel since the CPSD of opposite detectors present high coherence and out-of-phase relationship [23]-[24]. It is located in the 8 Hz region as it can be seen in the ex-core APSD shown Fig. 5.3

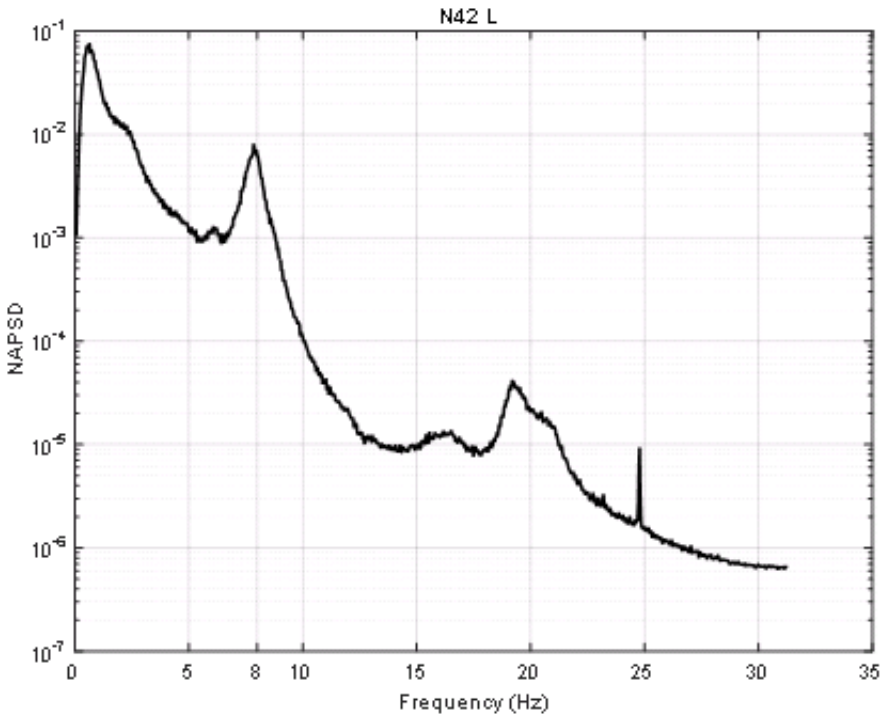

Figure 5.2: NAPSD of an ex-core detector signal

There are other peaks and resonances in the ex-core spectra that can be fitted through a Breit -Wigner formula [27]-[28]:

$$APSD\left(\omega\right)=\sum_{\lambda}\left\{\frac{\mu_{\lambda}A_{\lambda}+\left(\omega-\nu_{\lambda}\right)B_{\lambda}}{\mu_{\lambda}^{2}+\left(\omega-\nu_{\lambda}\right)^{2}}+\frac{\mu_{\lambda}A_{\lambda}-\left(\omega-\nu_{\lambda}\right)B_{\lambda}}{\mu_{\lambda}^{2}+\left(\omega+\nu_{\lambda}\right)^{2}}\right\} \tag{5.1}$$

Being A the pole strength, μ the damping, ν the frequency, B the skewness and λ is the index used to refer to the number of resonances. This formula has proved to be very effective in fitting different spectra from 0 to 20 Hz even if there are overlapping resonances [27], [26]-[29]. Among the different peaks found, the Beam Mode and the Shell Mode are the most relevant mechanical vibrations present in the ex-core neutron spectra. This is why some models have taken into account these two main noise sources and others to reconstructs the ex-core data signals [23]:

$$\begin{array}{l} \delta\phi_1(t) = \delta r_1(t) + \delta P(t) + \mu x(t) + D(t) \\ \delta\phi_2(t) = \delta r_2(t) + \delta P(t) - \mu x(t) + D(t) \\ \delta\phi_3(t) = \delta r_3(t)_1 + \delta P(t) + \mu y(t) - D(t) \\ \delta\phi_4(t) = \delta r_4(t)_1 + \delta P(t) - \mu y(t) - D(t) \end{array} \tag{5.2}$$

Here ϕ_1, ϕ_2, ϕ_3 and ϕ_4 stand for the neutron noise from detectors N41, N42, N43 and N44 of a PWR Westinghouse type reactor. Being δr_i the uncorrelated background noise component, δP the point kinetic or reactivity component, D is the shell mode component and the beam mode vibrations are supposed to happen in two directions x and y with a certain scaling factor μ between neutron noise and mechanical vibrations. By properly combining the equations above in the time domain, it is possible to reinforce certain components as shown in the example that follows for the beam mode:

$$\begin{array}{l} \mu x(t) = \frac{1}{2}\left(\delta\phi_1(t) - \delta\phi_2(t)\right) \\ \mu y(t) = \frac{1}{2}\left(\delta\phi_3(t) - \delta\phi_4(t)\right) \end{array} \tag{5.3}$$

The uncorrelated background noise components are supposed to be small compared to the beam mode components, and the shell and point kinetic components are cancelled out with this combination. Depending on the component that needs to be enhanced, the combination will be different. The spectra of the different combinations are shown in Fig. 5.3 where it can be seen how the searched peaks are enhanced with this technique. By using this methodology and the Breit-Wigner fitting it was possible to demonstrate that the beam mode component in the Ringhals PWRs are composed of two different resonances; one related to the core barrel pendular motion, and the other related to the flow induced fuel vibrations. A complete explanation of this can be found in the recent reference [30].

5.3 Another type of vibration: the tilting mode

Recent observations of wear at both the lower and upper core-barrel-support structures in the Ringhals PWRs indicated that vibration modes of the core barrel other than pendular (beam mode) and shell mode are likely to occur. A beam mode type movement alone is not able to explain such a wear, and therefore, it is fair to assume that the vibration mode in question is a small amplitude periodic tilting movement of the core barrel around a horizontal, diagonal pivot at the half height of the core. In Fig. 5.4 there is an illustration of the type of movement. The ex-core detectors are in grey scale so that the same color in two of them means an in phase

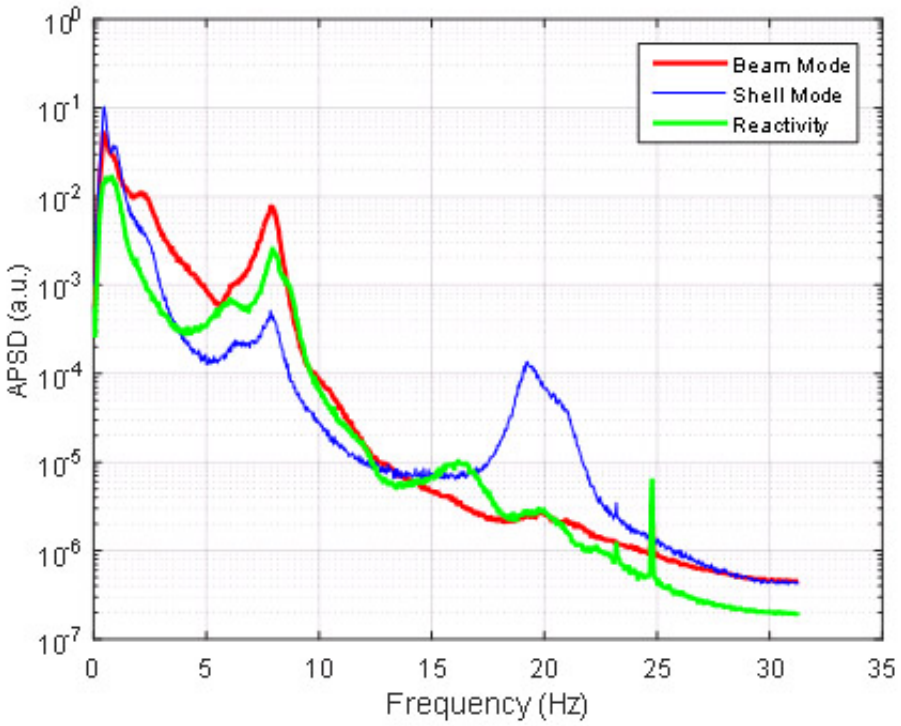

Figure 5.3: APSDs of the different noise sources of an ex-core detector.

relationship.

In order to prove the existence of this movement, ex-core detectors at different axial levels need to be considered in the analysis. A total of four different measurements are used, three within the same cycle and the other one in another cycle. CPSDs between N43U and N44L are calculated so that high coherence and in phase relationship are expected in the frequency region close to beam mode.

As it can be seen in Fig. 5.5, there is a region showing in-phase behavior just above 8 Hz. According to [30], this region is related to flow induced fuel vibrations. The CBM vibration can be seen with an out-of-phase relationship and high coherence. Another region with zero phase is 15-22.5 Hz, but this is widely known as the shell mode region. So, in principle, it is not easy to find traces of tilting movement in the spectra. It is probably due to the fact that the beam mode is a very dominant and preferred vibration. At this point it is necessary to reinforce the searched movement so that it can be enhanced by following the methodology described in the next sections.

5.4 Proposed model and mode enhancement technique

Let us take the model described in the previous section and add to it a new source of noise: the tilting movement vibration. Since this movement implies opposite detectors at different axial levels to be in-phase, the model needs to include both upper and lower detectors. In the equations the model is considering the diagonal

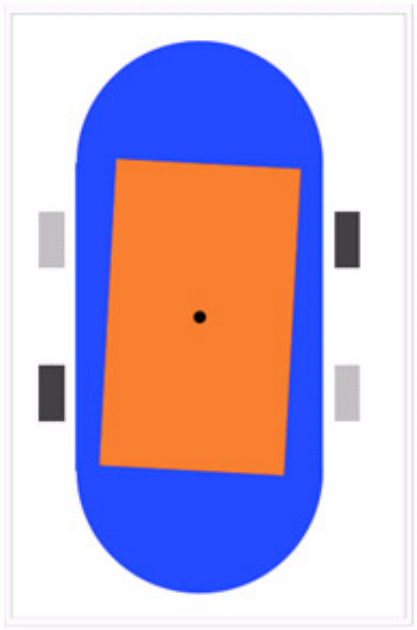

Figure 5.4: Illustration of the tilting mode vibration of the core barrel and the symmetries of the detector signals.

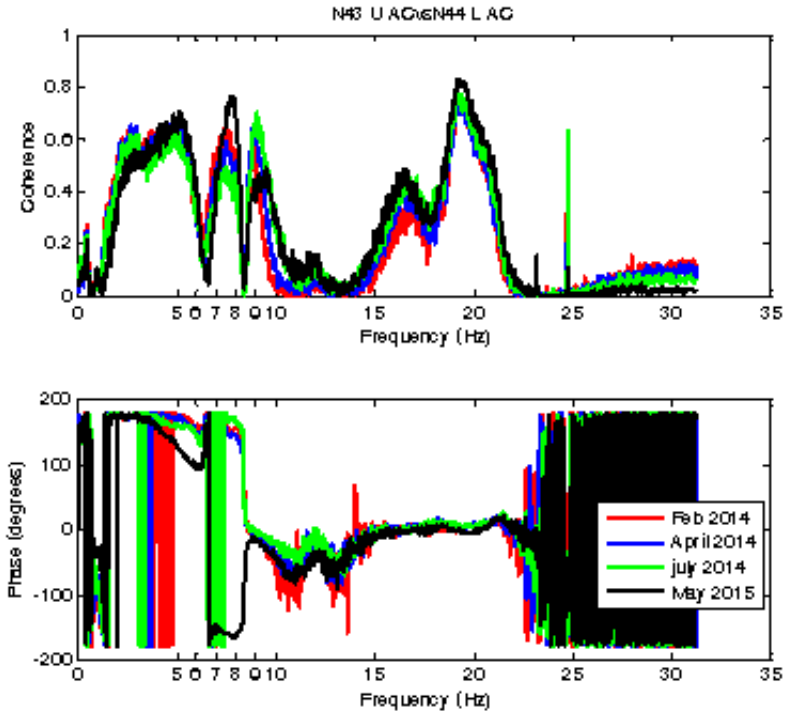

Figure 5.5: Coherence and phase of the CPSD between the ex-core detectors N43U and N44L.

N41-N42:

$$\delta\phi_{N41U} = \delta r_1(t) \quad + P(t) \quad + D(t) \quad - \mu x(t) \quad + \lambda x(t) \tag{5.4}$$

$$\delta\phi_{N42U} = \delta r_2(t) \quad + P(t) \quad + D(t) \quad + \mu x(t) \quad - \lambda x(t) \tag{5.5}$$

$$\delta\phi_{N41L} = \delta r_5(t) \quad + P(t) \quad + D(t) \quad - \mu(1+\alpha)x(t) \quad - \lambda x(t) \tag{5.6}$$

$$\delta\phi_{N42L} = \delta r_6(t) \quad + P(t) \quad + D(t) \quad + \mu(1+\alpha)x(t) \quad + \lambda x(t)\,a \tag{5.7}$$

Besides the components already explained in Section 2, the tilting mode is expressed with the term $\lambda x(t)$. The sign expresses the in-phase behaviour between diagonally opposite detectors at different levels, such as N41U-N42L and N42U-N41L. Since now detectors from both axial levels are involved, one must take into account the fact that the amplitude of the beam mode vibrations is larger for the lower detectors than for the upper detectors. Hence, the amplitude of the beam mode vibrations for the lower detectors is multiplied by the factor $(1+\alpha)$.

The next step is applying an enhancement technique so that the tilting movement mode could be reinforced. This is achieved as shown below:

$$\frac{\delta\phi_{N41U}(t) + \delta\phi_{N42L}(t)}{2} - \frac{\delta\phi_{N42U}(t) + \delta\phi_{N41L}(t)}{2} = \mu\alpha x(t) + 2\lambda x(t) \tag{5.8}$$

As it can been in equation (5.8), a beam mode component $\mu\alpha x(t)$ is still present in the expression above, although with a small weight, whereas the second term on the right hand side will be the enhanced tilting mode. In Fig. 5.5, the spectrum of such combination of signals is plotted for different sets of measurements from the same cycle.

Although the beam mode is still present after the enhancement, a new peak is found at around 6 Hz which is not clearly seen either in the individual detector spectra, or that of the other separated mode components (reactivity, beam and shell modes). Since the beam mode is dominating the signal around 8 Hz, just taking the cross-spectra between two diagonally placed upper and lower detectors, as in Fig. 5.4, will show neither a peak, nor an in-phase behaviour at 6 Hz.

5.5 Joint influence of in-phase and out-of-phase noise sources

Basically the ex-core spectra are composed of different components; some of them being in-phase and others out-of-phase, as it can be seen in the CPSD spectra in Fig. 5.4. According to Mayo [31], also referenced to in the review by Kosály [32], low measured coherence may also be the result of partial cancellation between in-phase and out-of-phase components. In fact, at 6 Hz the coherence shown in Figure 4 reaches zero and the phase has a small shift from 180°.

Between diagonally opposite detectors placed at different axial levels, the tilting movement is an in-phase process, whereas the beam mode is an out-of-phase one.

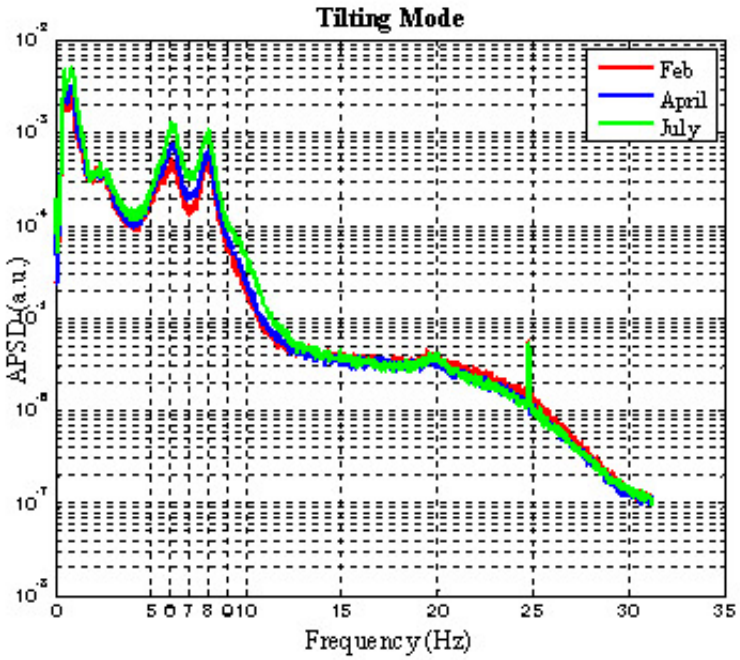

Figure 5.6: Enhanced tilting mode APSD for Ringhals R4 Unit.

Let us assume that in the 5-10 Hz region a certain detector signal is the sum of either in-phase or out-of-phase contributions as:

$$\begin{aligned} S_1(t) &= X(t) + Y(t) + s_1(t) \\ S_2(t) &= X(t) - Y(t) + s_2(t) \end{aligned} \tag{5.9}$$

Here, $S_1(t)$ and $S_2(t)$ representing the respective ex-core signals, $X(t)$ and $Y(t)$ are uncorrelated noise components which contribute to the signals of both detectors, and $s_1(t)$ and $s_2(t)$ influence only one of the ex-core chambers each. By usual techniques, one can obtain the coherence of the CPSD between both detectors as:

$$coh_{12}(\omega) = \frac{|APSD_X(\omega) - APSD_Y(\omega)|}{APSD_X(\omega) + APSD_Y(\omega) + APSD_s(\omega)} \tag{5.10}$$

As (5.10) shows, the coherence can be zero if the APSD of each process is equal to each other, and the phase is zero if the X process dominates over the Y process. Out-of-phase relationship would exist in the opposite case. This can be appreciated in Fig. 5.4 where the coherence goes to zero at around 8 Hz and the phase changes from 180° to 0°. In this case the two processes involved are the core barrel pendular motion and the flow induced fuel vibrations.

It is also possible to derive expressions for the in-phase process and out-of-phase process spectra, APSD_x and APSD_y respectively:

$$\begin{aligned} APSD_X(\omega) &= \left\{ \frac{1 \pm coh_{12}(\omega)}{2coh_{12}(\omega)} \right. |CPSD_{12}(\omega)| \\ APSD_Y(\omega) &= \left\{ \frac{1 \mp coh_{12}(\omega)}{2coh_{12}(\omega)} \right. |CPSD_{12}(\omega)| \end{aligned} \tag{5.11}$$

The above expressions serve to make a difference between the in-phase and-out-of phase noise sources. In the present work, the methodology is applied to two ex-core detectors placed diagonally opposite to each other and at different axial levels of a Ringhals PWR. The in-phase process is the tilting movement and the out-of-phase one is the beam mode pendular core barrel motion. The results and discussion are presented in the next section.

5.6 Results on the separation of the tilting and beam mode components

The in-phase and out-of-phase spectra for the pair N43U-N43L is shown in Fig. 5.7.

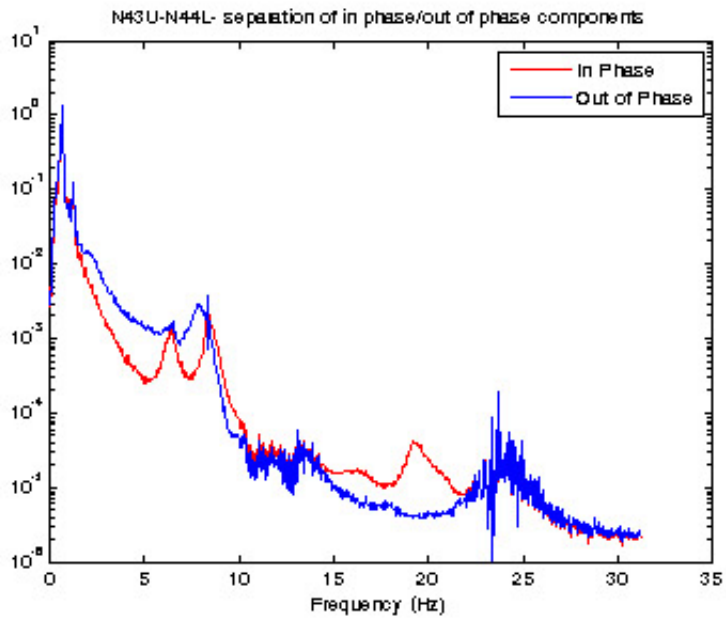

Figure 5.7: In-phase and out-of-phase APSDs for the pair of ex-core detectors N43U-N44L.

The tilting mode at 6 Hz appears as an in-phase process, but its amplitude is lower than that of the beam mode at 8 Hz in the out-of-phase spectra. This is probably the reason why it is not clearly seen in the spectra of individual detectors because the beam mode turns out to be the dominant vibration in this frequency region. It is also possible to see another peak at around 8-9 Hz in the in-phase curve that is probably related to the flow induced fuel vibrations, the second type of vibration part of the beam mode broad peak [30]. The shell mode is clearly an in-phase process, and it is indeed for a pair of detectors located diagonally opposite.

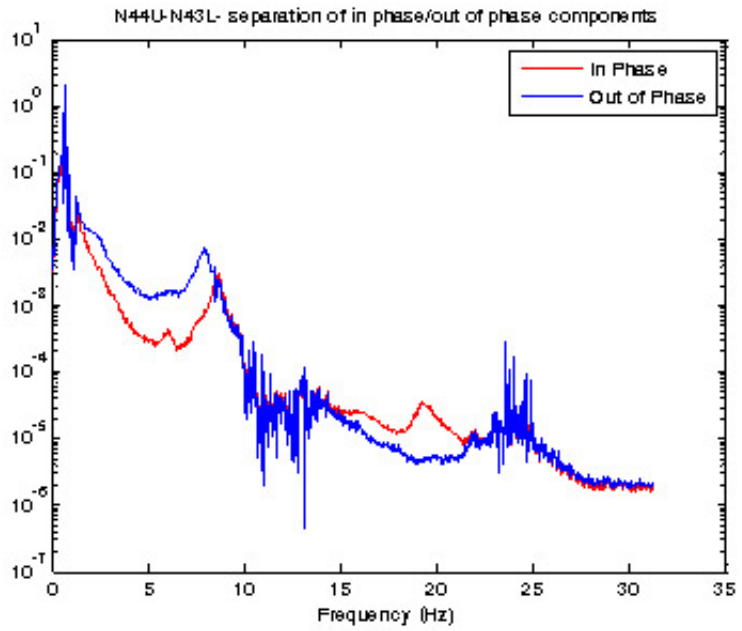

Figure 5.8: In-phase and out-of-phase APSDs for the pair of ex-core detectors N44U-N43L.

Considering another pair of detectors in Fig. 5.8, the results are consistent with the tilting mode hypothesis, since it is also present as in-phase process but its amplitude is very low compared to the out-of-phase spectra. Again, the shell mode is present as an in-phase process and the beam mode is divided into two peaks, one belonging to the out-of-phase profile (core barrel pendular motion) and the other one to the in-phase spectra (flow induced fuel vibrations).

For a pair of detectors at the same radial position and different axial levels, the in-phase process will dominate, but the tilting movement should be present in the out-of-phase spectra. This can be appreciated in Fig. 5.9. The CBM is an out-of-phase process, the fuel vibrations and the shell mode result as an in-phase process.

5.7 Conclusions

The results presented in this section show the existence of a core barrel vibration mode different from the beam and the shell modes. The observations of wear which prompted the investigation as well as the analysis performed in this work support the idea of a small amplitude periodic tilting movement of the core barrel around a horizontal, diagonal pivot at the half height of the core.

The analysis was made based on a model where the detector signals are composed of different sources, one of them being the vibration resulting from the tilting movement. By properly combining the signals of the ex-core detectors in the time domain, such mode is enhanced and it is possible to appreciate as a 6 Hz peak in the spectra of the combined signals.

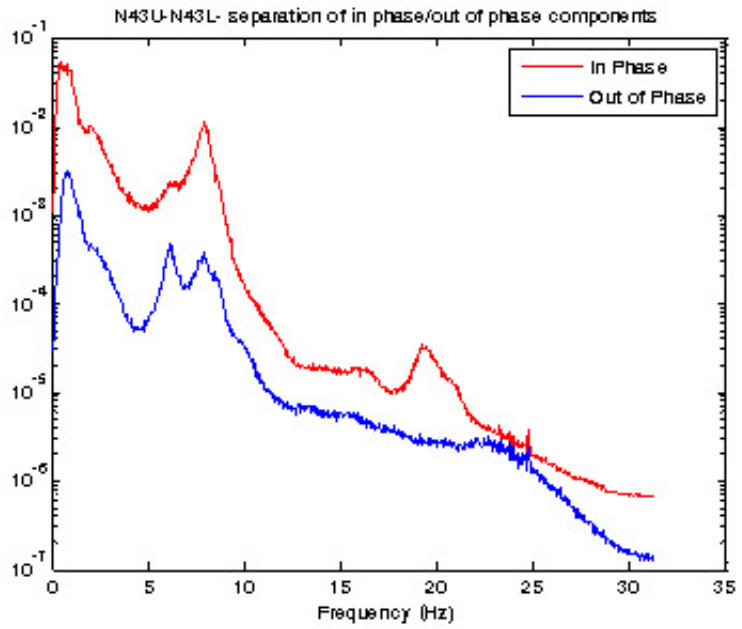

Figure 5.9: In-phase and out-of-phase APSDs for the pair of ex-core detectors N43U-N43L.

In order to validate this procedure, another methodology based on a technique for separating in-phase and out phase processes was used. This method is able to separate the tilting mode from the beam mode and also works to identify other known modes of vibration such as the shell mode or the fuel assemblies vibrations.

6. A BASIC STUDY IN NEUTRON NOISE THEORY WHICH COULD PROVIDE SOME INDIRECT SUPPORT FOR THE DETERMINATION OF THE VOID FRACTION FROM NEUTRON NOISE MEASUREMENTS

A basic study in neutron noise was outlined in the final report of the previous Stage [1]. It showed how the modulation of a moderating or scattering medium, without the presence of fissile material, will induce non-trivial (correlated) fluctuations both in pulse count and current mode of the detectors. It was suggested that an experimental verification of the theoretical predictions be made during the present Stage. As mentioned also in the last report, in addition to its own research value, this study could also give some indirect support to our efforts in the determination of the void fraction from neutron noise measurements.

The idea is that neutrons emitted independently from each other by a source with simple Poisson statistics (Am-Be or Pu-Be source), slowing down and diffusing in a non-multiplying medium, which are hence originally uncorrelated, and would remain uncorrelated in a steady medium, become correlated if the medium in which the slowing down and diffusion takes place is fluctuating (e.g as a result of a perturbation, such as the presence of two-phase flow). A suitable experiment requires a neutron source in a water tank, and at least two neutron detectors. Bubbles introduced in the water between the source and the detectors would act as a suitable perturbation.

At the time when the original idea arose, it appeared possible to construct an experimental setup, and to perform such experiments in Chalmers. Irradiation experiments with much higher complexity were performed during the decades when the reactor and neutron physics activities were performed in a separate building, which housed the department (then called Department of Reactor Physics). For instance, in the frame of the FlowAct project a complex water loop was built for developing a method for high accuracy measurement of the mass flow of water in a pipe with pulsed neutron activation of the water and measuring the gamma-decay of the produced ^{16}N nuclides [33, 34].

However, by moving from our previous building to another place in Chalmers, we lost most of our experimental facilities and possibilities. This, combined with shrinking of technical support and personnel resources in general, lead to the loss of the possibility to build a facility and perform the experiments in Chalmers. Luckily, both interest and practical possibilities exists at our collaboration partners at EPFL Lausanne, in collaboration with PSI. In particular, the CARROUSEL facility is available, which is suitable to perform the planned experiments [35] The work has already started, and preliminary results are available, which will be reported in this Chapter. The material below is largely taken from the corresponding draft report by Oskari Pakari [36].

6.1 Introduction

The considerations regarding the experimental proof of how the effect of the perturbartion will induce correlations between the detector counts with originally independently injected netutrons into a non-multiplying medium were described in the previous report [1]. However, they were formulated in terms of the statistics of the number of neutrons in the system, whereas for the interpretation of the experiments, one needs them to be reformulated in terms of the number of detections, which will be done first.

Basically, there are two straightforward options to prove the influence of the perturbations of the non-multiplying medium on the statistics of the neutron number through the detection statistics. One or them is to use one detector. With independently emitted and detected neutrons, in a stationary case (constant source and system), the number of neutrons N in the system follows a Poisson distribution

$$P(N) = \frac{e^{-\langle N \rangle} \ \langle N \rangle^N}{N!} \tag{6.1}$$

For such a case, the number of detection counts $Z(t)$ during a measurement interval t will also follow Poisson statistics::

$$P(Z,t) = \frac{e^{-\langle Z(t) \rangle} \ \langle Z(t) \rangle^Z}{Z!} \tag{6.2}$$

For a Poisson distribution, the variance is equal to the mean, i.e. one has

$$\frac{\sigma_N^2}{\langle N \rangle} = \frac{\sigma_Z^2(t)}{\langle Z(t) \rangle} = 1 \tag{6.3}$$

However, as described in the previous report, based on the results in [37, 38], in a randomly varying medium, since the fluctuations of the medium influence the number of the neutrons simultaneously, inducing positive correlations, the variance to mean of the neutron number will exceed that of the Poisson distribution, i.e. it will be larger than unity:

$$\frac{\sigma_N^2}{\langle N \rangle} = 1 + Y \tag{6.4}$$

where Y is a positive number. For the number of detections $Z(t)$ during time t, one expects that it can be written as

$$\frac{\sigma_Z^2(t)}{\langle Z(t) \rangle} = 1 + Y(t) \tag{6.5}$$

Formally, (6.5) looks very similar to the expression for the Feynman-alpha formula of reactivity measurement in subcritical source-driven systems, where a concrete functional relationship is known for $Y(t)$. However, it has to be kept in mind that the time-dependence of the Feynman $Y(t)$ function is related to the die-away of the prompt neutron chain, whereas in the present case, there are no chains generated. The time dependence of the $Y(t)$ for the case of non-multiplying, randomly varying

medium is not known. Based on the considerations in [37, 38], it is most likely related to the temporal auto-correlation of the fluctuations of the randomly varying medium, if the modulation is uniform in space. In particular, a similar functional form can be expected for the $Y(t)$ as for the Feynman-method, but the parameter α will correspond to the temporal die-away of the correlations of the state changes of the medium. Performing the modulation of the medium by blowing bubbles into water, the random modulation of the medium becomes space-dependent, and no simple theoretical form of the function $Y(t)$ can be predicted. However, it will be interesting to perform measurements, and see if the time-dependence of $Y(t)$ will show a form similar to the traditional Feynman-alpha formula, and if so, what decay parameter α can be extracted from it.

The second possibility is to use two detectors, and measure the covariance between the counts of the two detectors, i.e. to measure

$$\mathrm{Cov}(Z_1, Z_2) = \langle Z_1 Z_2 \rangle - \langle Z_1 \rangle \langle Z_2 \rangle \tag{6.6}$$

For a non-perturbed non-multiplying medium, the covariance should be zero. For the case of a medium with a perturbation, the covariance should be larger than zero.

This second option is somewhat less simple to apply in practice than the first. This is because in an experiment, the estimate of the covariance will result in a non-zero value even for uncorrelated events, due to finite measurement time, measurement errors etc. Since, due to low count rate (as compared to measurements in a reactor core), the deviations from the Poisson statistics are expected to be low, it may be difficult to judge whether the deviation of the covariance from zero is sufficiently consistent and significant so that it can be regarded as a proof of the existence of the correlations. Nevertheless, both options will be investigated in the measurements.

This experiment originally involved a simple detection setup to measure the temporal correlation between two detectors with and without a bubbly flow in between the source and the detectors. Due to induced electronic noise with the initial acquisition, the experiment was re-arranged and the results were re-evaluated. Data from three setups are discussed:

- I) The original detection setup, with the amplifier that randomly caused additional counts
- II) Setup I with exchanged amplifiers.
- III) Setup II with an aluminium plate set between the bubble flow and the detectors to minimize possible mechanical influences.

6.2 Experimental setup

The CARROUSEL facility consists of a cylindrical aluminium water tank with a diameter of 1.5 meters with a height of 1.6 meters, see Figure 6.1. In the middle at around 78 cm height a Pu-Be source ($\sim 5 \cdot 10^6$ n/s) can be inserted into a thin PVC

tube. On a rail above the tank detector tubes can be attached at various distances to the source.

Figure 6.1: **Left: Wire mesh model of the CARROUSEL facility. Right: Picture from above on the CARROUSEL tank with internals of the experiment visible.**

The experimental setup used is depicted in Figure 6.2, with the associated detectors and electronics sketched in Figure 6.3. Two Helium-3 detectors were installed horizontally at 25 cm from the source tilted into a specifically designed holder that allows for variable horizontal and vertical shift of detector locations. Both detectors were connected to 1100 V high voltage and standard gamma spectroscopy preamplification and amplification hardware, giving an analogue signal to the MCS cards of the noise acquisition PC [39]. A standard aquarium bubble diffuser with a length of around 30 cm and width of 2 cm was installed at the bottom between detectors and source at 10 cm from the source (see Figures 6.1 and 6.2).

The diffuser was connected to the pressurized air access facilities with a manometer in between. This allowed for variable air flow to the diffuser, characterized by litres of air per minute, or "lpm". Fig. 6.4 shows the setup at 0 lpm, i.e. with no bubbles. Figure 6.5 and 6.6 show the setup at 10 and 20 lpm, respectively.

Note: 1 The manometer used to set the flow rate is not calibrated and thus might not accurately reflect a linear increase. Additionally, the flow rate could only be set within 2 lpm uncertainty of reading accuracy.

Note 2: The average bubble velocity at the height of the detectors was estimated using a camera filming the bubbles at 30 fps in front of a ruler. 30 tracks were measured and averaged to find the average velocity

$$\overline{v}_{Bubble} = (0.6 \pm 0.1)\,\mathrm{m/s} \tag{6.7}$$

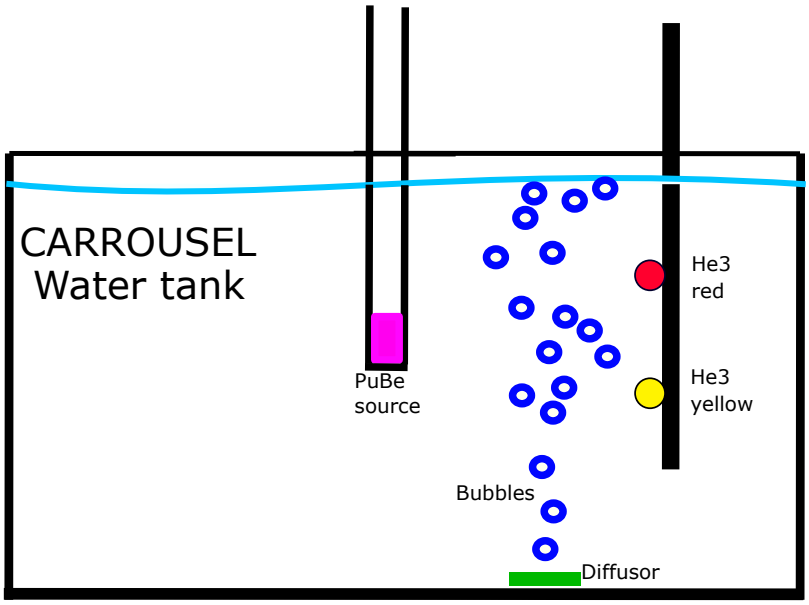

Figure 6.2: **Schematics of the experimental setup in the CARROUSEL facility. A diffuser was installed at the bottom of the tank that allowed for variable bubble output (green).**

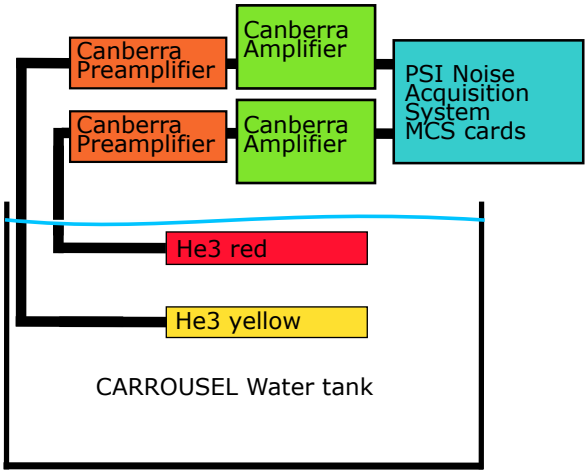

Figure 6.3: **Detection scheme regarding the neutron detectors used and the associated electronics.**

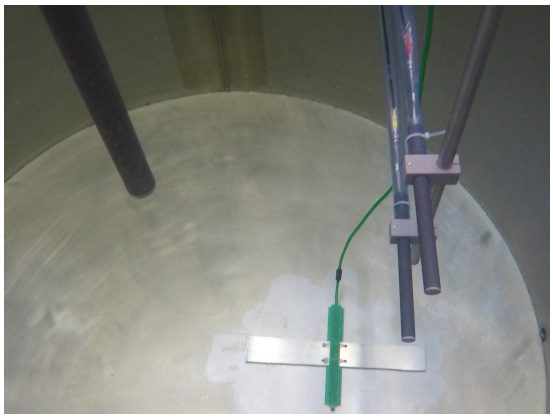

Figure 6.4: **Picture of the experimental setup at 0 lpm.**

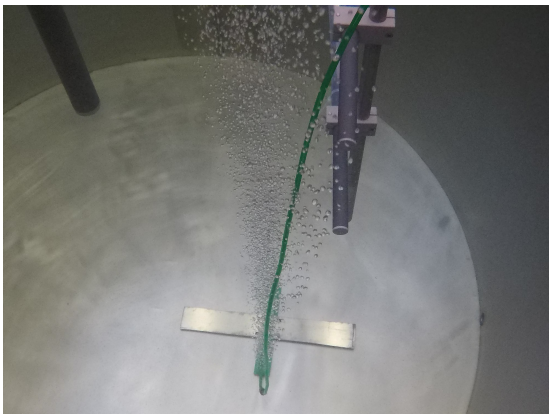

Figure 6.5: **Picture of the experimental setup at 5 lpm.**

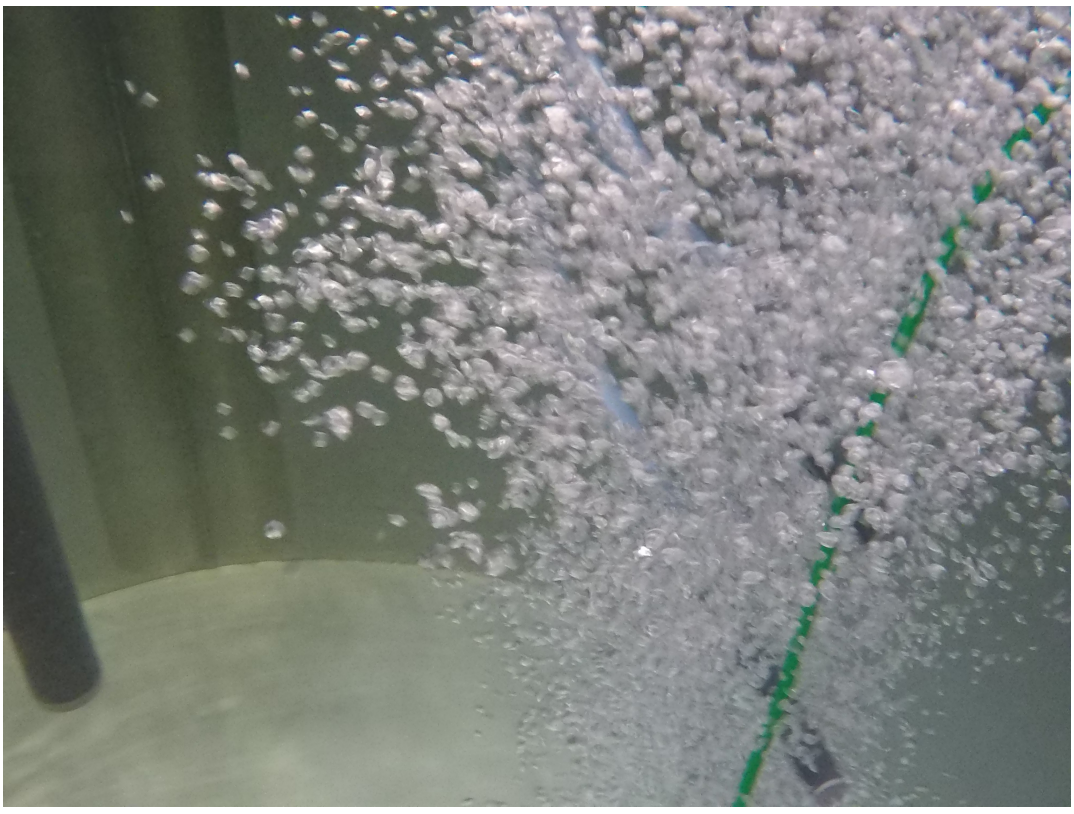

Figure 6.6: **Picture of the experimental setup at 20 lpm.**

6.3 Results and discussion

6.3.1 Setup I

The amplifier used with He-3 yellow was found to randomly add correlated noise. This noise would triple the count rate for up to 30 min and thus cause the previously measured high variance over mean curves (Var/Mean $>$ 100, see Figure 6.7 below). The noise was found to be caused by the output connector of the amplifier and could be reproduced at 0 lpm by wiggling the input cable. This would cause echoes or even cut the signal off completely. For this reason the amplifier was exchanged and all connections were checked for faulty contacts.

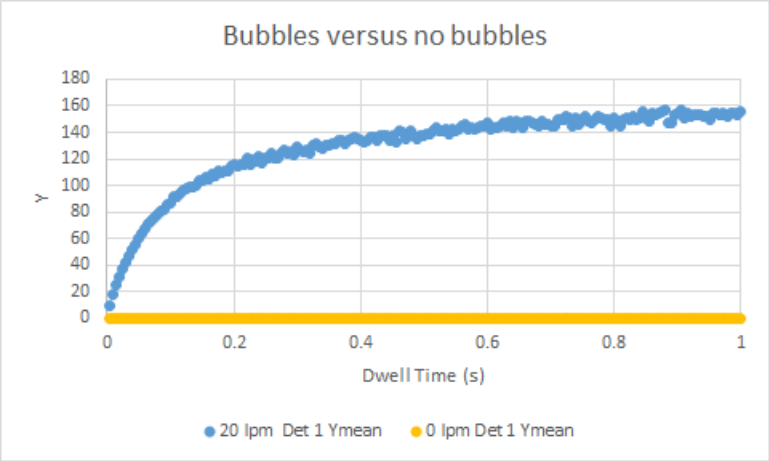

Figure 6.7: **Measured Y-curves for detector 1 (He-3 yellow) in case of 20 lpm air flow and 0 lpm (i.e. no bubbles). The individual sweep data showed that the first 4 sweeps had a tripled count rate compared to the rest of the data.**

6.3.2 Setup II & III

Conduct of experiments

For different flow rates of 0, 5, 12, 20 and 25 lpm the count rates of both detectors were registered over 4 hours with a dwell time of 5 ms per bin. The discriminator threshold was set to a relatively high value of 2 V (usually 0.5 V) to avoid induced noise by the electronics.

During the experiments the hypothesis arose, that the induced correlation could be due to mechanical vibrations induced by the bubbles on the detector cables or connectors. For this purpose an aluminium plate was set between the detectors and bubbles to minimize the effect and to allow for comparison (see Figure 6.8). The experiments with a plate were carried out at 0, 5, 10, 15, 20 and 25 lpm. It has though to be noted that the plate was attached to the detector setup. This means that the possible vibrations of the aluminium plate could be transferred to the detectors, and hence the shielding effect of the plate against flow-induced vibrations

Figure 6.8: **Picture of the experimental setup III at 10 lpm with added aluminium plate with the aim to reduce vibrations induced by the bubbles.**

of the detectors is not perfect.

Comments on uncertainty. The statistical uncertainties for the covariances are below 1%, assuming a standard Poisson distribution. Nonetheless, systematic uncertainties inducing noise appear to have a strong effect on the results. This was shown in the previous measurements to be caused by the amplification stage. Now in the revised experiments, the influence of mechanical vibrations can still not be ruled out as cause for the increased covariance. Further improvements would include more sophisticated mechanically isolated channels for both the bubbles and the detectors.

6.3.3 Results for the covariance

The results for the measurements with and without plate for the covariance between the two detectors are shown in Table 6.1. Furthermore, the data is shown in semilog scale in Figure 6.9.

Table 6.1: **Covariances between the two He-3 detectors at different flow rates, with and without plate in-between.**

lpm	0	5	10	12	15	20	25
$Cov_{1,2}$ with plate	2.0e-5	0.014	0.004		0.010	0.012	11.779
$Cov_{1,2}$ without plate	6.6e-4	0.012		0.003		1.702	0.011

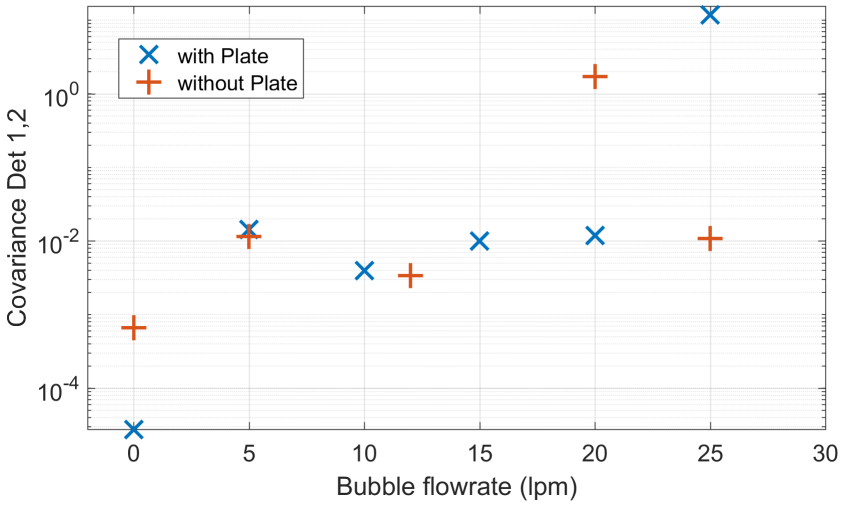

Figure 6.9: **Semilog plot of covariances between the detectors at varying flow rates.**

6.3.4 Discussion

Effect of bubbles A general first observation is that the covariance deviates from (close to) zero for a non-zero flow rate, irrespective of the presence of the plate. In Figure 6.9 a general linearly increasing covariance with flow rate can be observed.

Plate versus no plate The plate and no plate cases appear to agree for low flow rates below 15 lpm. Above 20 lpm we observe two orders of magnitude and more difference. This indicates that the plate might not help in reducing mechanically induced noise, as noise appears to perturb the measurement above 20 lpm in both cases. As mentioned before, this may be due to the fact that the plate is in mechanical contact with the detector setup.

Hypothetical fits Examples of hypothetical linear and quadratic dependences for the two cases of with or without the aluminium plate, for the data in Fig. 6.9 are shown in Fig. 6.10. The question marks denote points which were found to be outliers to the data fitting procedure.

An obvious linear relationship does not appear to apply due to the outlier values at 5 lpm and 20/25 lpm. One could assume, that these values are systematically to be excluded due to noise. In this case a linear relationship for the values for 0, 10 and 12/15 lpm can be seen for both cases.

On the contrary, the values for 5 to 15 lpm appear to agree in both cases within reading accuracy for the flow rate. This raises another possibility: The values above around 20 lpm are unreliable due to induced mechanical noise and a linear depen-

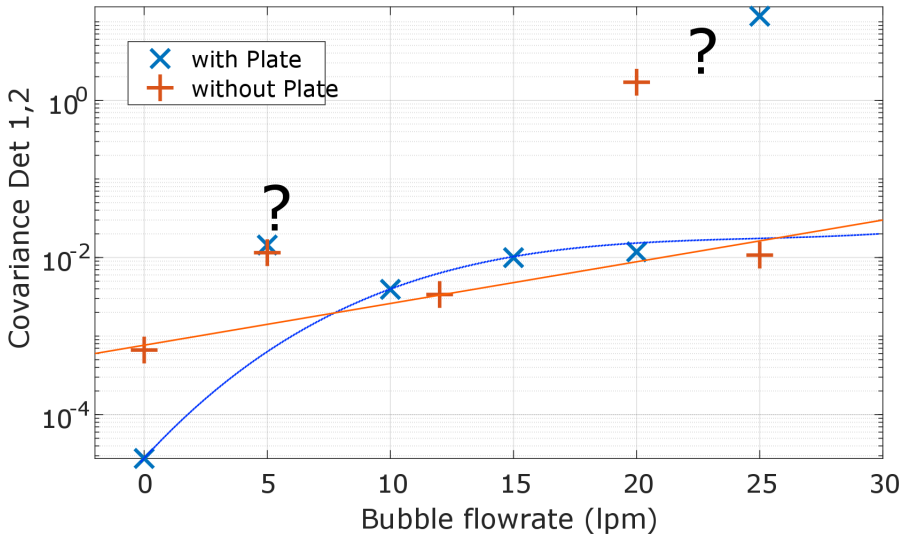

Figure 6.10: **Semilog plot of covariances between the detectors at varying flow rates. Potential trend lines have been added for discussion purposes.**

dence up to that point is found.

6.3.5 PSD estimates

Finally, as a alternative way to visualize the data, the auto and cross power spectra of the measurements were estimated. This was accomplished by the Welch PSD method using a sufficiently long rectangular window to estimate the PSD down to 10^{-2} Hz. The APSDs of He3-yellow for the different flow rates are shown in Figure 6.11 without the plate and in Figure 6.12 with the plate. The CPSDs for the different flow rates are shown in Figure 6.13 without the plate and in Figure 6.14 with the plate.

Discussion Without the plate the APSD and CPSD estimates agree in terms of shape. With increasing flow until 20 lpm a low frequency plateau rises with a cut-off frequency around 0.5 Hz.

With the plate, at 10 and 15 lpm, a peak at around 0.15 Hz can be seen, with a slightly higher value for 15 lpm compared to 10 lpm. This shows an oscillation of unknown origin.

With the plate the estimates also agree in terms of shape. An immediate remark is that the 25 lpm PSDs show a sink structure. The source of this behaviour is believed to be an error on the PSD estimation, e.g. due to the rectangular window being incompatible with the data.

In conclusion, further investigatons are need on the PSD shapes.

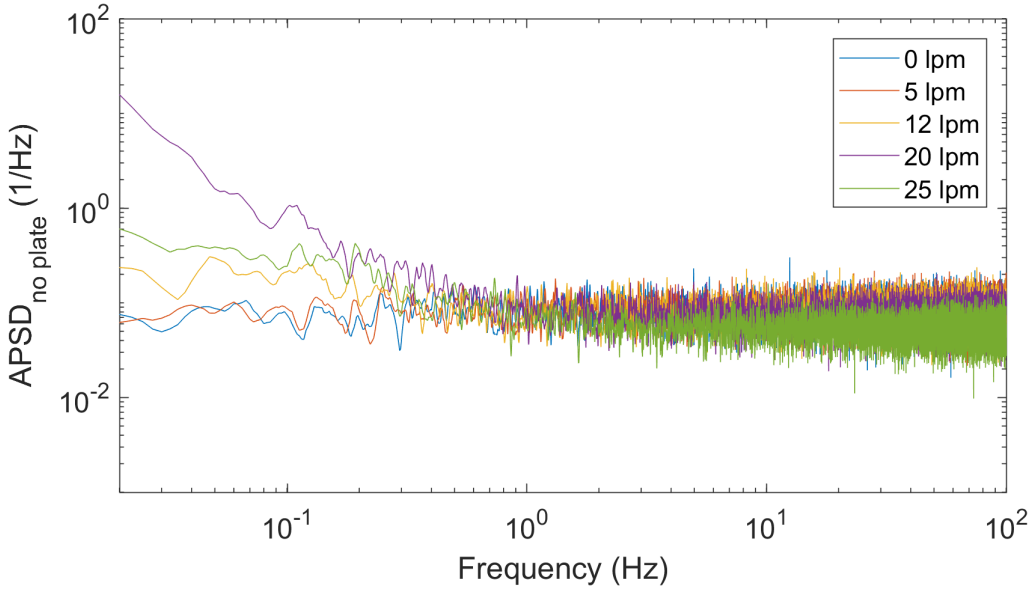

Figure 6.11: **Auto power spectral density of He3-yellow at varying flow rates without the plate.** At higher flow rates a cut off frequency at ∼0.5 Hz becomes visible.

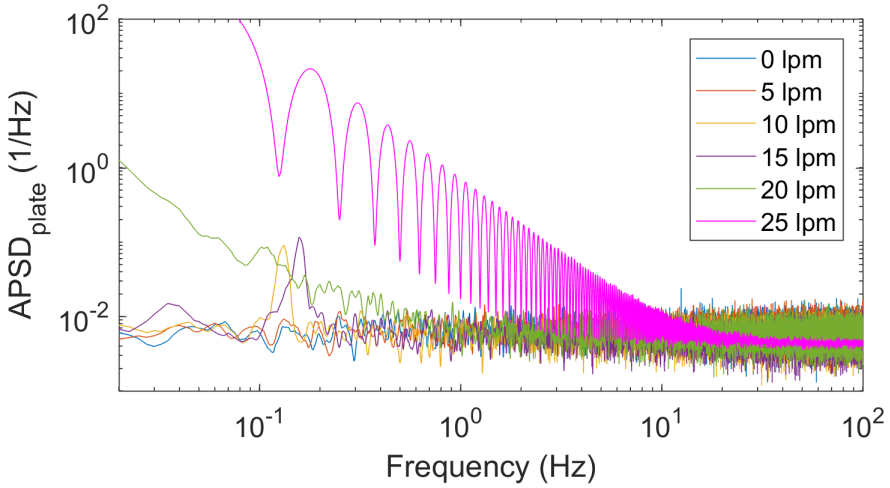

Figure 6.12: **Auto power spectral density of He3-yellow at varying flow rates with the plate.** At 10 and 15 lpm a peak at 0.05 Hz is visible.

6.4 Summary

The bubble experiment in the CARROUSEL facility in its revised form has been conducted. Using a (Poisson) PuBe source in a water tank, a bubble diffuser and two He-3 detectors, the effect of induced correlation due to a stochastic medium was investigated. The analysis methods include covariance and PSD estimation. Results indicate an effect on correlation of neutrons due to the bubbles in dependence of

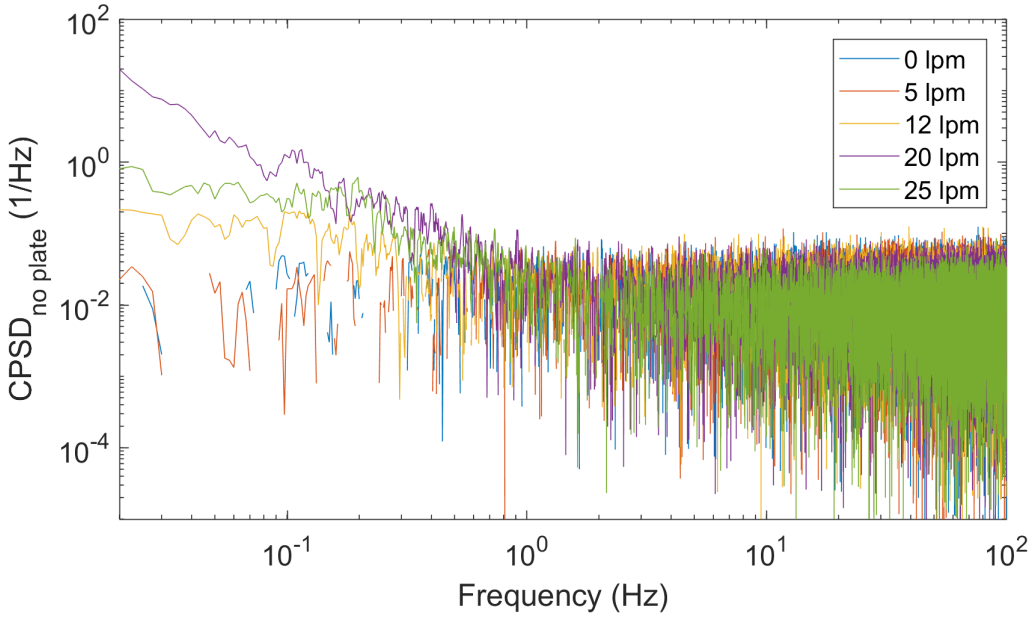

Figure 6.13: **Cross power spectral density at varying flow rates without the plate.** The shapes are consistent with the APSD shapes without the plate.

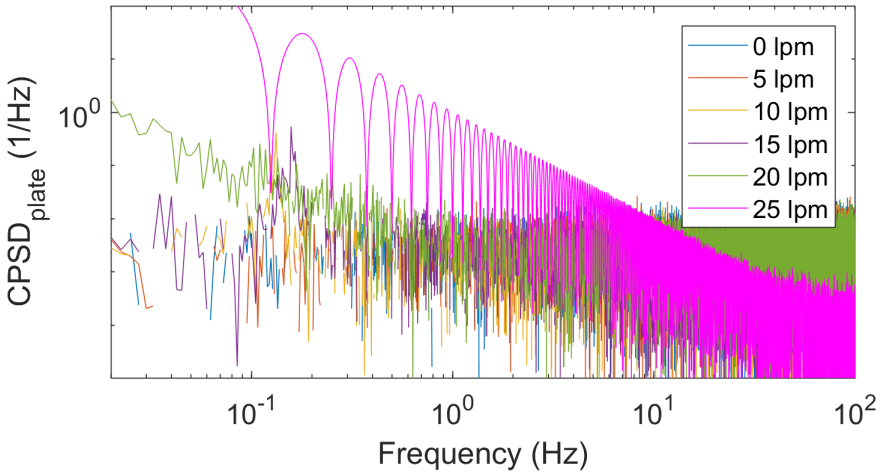

Figure 6.14: **Cross power spectral density at varying flow rates with the plate. The shapes are consistent with the APSD shapes without the plate.**

flow rate. The behaviour of said dependence is not clearly quantifiable from the data.

7. A PILOT STUDY OF THE POSSIBILITY OF USING FISSION CHAMBERS FOR ZERO POWER NOISE EXPERIMENTS

In zero power noise experiments, the subcritical reactivity of a core is determined from the statistics of the individual detector counts: either from the time correlations between two consecutive counts (Rossi-alpha method) or from the relative variance of the number of detections as a function of the measurement time (variance to mean or Feynman-alpha method). These methods have been elaborated a long time ago, and have been used routinely for monitoring subcritical reactivity during start-up, or during the operation of an accelerator-driven system (ADS).

However, there are incentives for seeking alternative methods for supplying the same information. One reason is that pulse counting methods encounter difficulties at higher neutron fluxes (high count rates), due to dead-time problems. Whereas it is easy to correct for the dead-time what regards the mean count rate (the first statistical moment), such corrections are incomparably more complicated for the higher moments, such as the variance.

The second incentive arises from the fact that the archetype of detectors for pulse counting is the He-3 detector. There is a global shortage of He-3 worldwide, making replacement of old detectors and acquiring new detectors difficult.

One possible alternative, which would remedy both problems, is to use fission chambers. They do not suffer from the shortage of detector material; further, by operating them at high count rates in the so-called Campbell mode, or in the current mode, they are insensitive to dead time problems. However, since in the current mode the individual counts are not distinguishable, the statistics of the number of pulses cannot be extracted from the signals, only the statistics of the continuous detector current (its mean, variance and higher moments) at a time point can be measured (and also calculated from suitable models). Therefore, a substantial theory development has to be made in order to extract the same information from the statistics of the continuous current of the fission chambers as from the pulse counting methods.

Very recently we succeeded in developing a powerful formalism for the statistical theory of fission chamber currents in reactor measurements, based on the master equation formalism [40, 41]. This opens up the possibility to investigate whether the prompt neutron decay constant $\alpha = (\rho - \beta)/\Lambda$ can be extracted from the statistics of the continuous current signals of fission chambers. This is the subject of this Chapter. It will be shown that the temporal covariance of the detector signal (an analogue of the Rossi-alpha function of the traditional discrete pulse counting) contains, among others, the prompt neutron decay constant in form of an exponential function of the time difference, similarly to the traditional Rossi-alpha measurement. Hence, there is a possibility, at least in principle, to determine the prompt neutron decay constant. However, the covariance function is much more involved than a Rossi-alpha curve, and contains other time-dependences, such as that of the

detector pulse shape. Therefore extraction of the prompt neutron decay constant is less straightforward. On the other hand, as mentioned before, the method is free from dead time problems.

The derivation of the covariance function of the detector signal is considerably more complicated than the derivation of the Rossi-alpha method. Hence, in the continuation, the principles of the model, the main steps of the derivation, and the final result will be given. All details can be found in the journal publications [40] and [41].

7.1 The principles of the model

7.1.1 Signal statistics for a single source event

The goal is to determine the probability distribution of the random process $\boldsymbol{\eta}(t)$, represented by the detector signal (detector current). To this end we will use an extended version of the formalism applied in [40] to account for the statistics of the incoming particles.

Although the signal of the detector at any given time is the sum of the signals of all previous random detections, the starting point is, just as in [40], to specify the properties of the detector signal after the *detection* of *one neutron*. In [40], from these, it was immediately possible to write down a backward master equation for the probability distribution of the detector signals, due to the independence of the detection events. In the present case, it will not be possible to directly specify the probability of the arrival of the neutrons at the detector; we can only specify the probability (intensity) of the source neutron emission and hence write down a master equation for the probability distribution of the detector signal for *one source neutron*. After that, as is usual in the backward theory of branching processes, another master equation needs to be written down to connect the detector signal distribution due to one single starting neutron, with that induced by a continuous source of neutrons, which induces the stationary neutron distribution in the system (and hence the stationary distribution of the detection events).

Let $\varphi(\boldsymbol{\xi}, t)$ denote the detector signal which exists in the detector at time $t \geq 0$ after the arrival of one neutron at $t = 0$. It will be assumed that this signal depends also on random parameters, which is indicated by the random variable $\boldsymbol{\xi}$ as the argument of φ[1].

Keeping the general notation $\varphi(\boldsymbol{\xi}, t)$, we will assume that the probability distribution $W(x)$ of the random variable $\boldsymbol{\xi}$ is known:

$$\mathcal{P}\left\{\boldsymbol{\xi} \leq x\right\} = \int_{-\infty}^{x} w(x')\, dx' = W(x). \tag{7.1}$$

Further, we will need the probability $H(y, t)$ of the event that for any possible

[1] In our previous work [40] it was assumed that $\varphi(\boldsymbol{\xi}, t) = \boldsymbol{\xi}\, f(t)$, where $f(t)$ was a deterministic, decreasing function of its argument, whereas $\boldsymbol{\xi}$ was the random amplitude of the signal. The same assumption will be used in this paper in the concrete examples, but with a deterministic (constant) amplitude.

realisation $\{\boldsymbol{\xi} = x\}$ of the random variable $\boldsymbol{\xi}$, the random function $\varphi(\boldsymbol{\xi}, t)$ is not larger than y. This can be expressed by

$$H(y,t) = \int_{-\infty}^{+\infty} \Delta[y - \varphi(x,t)]\, w(x)\, dx. \tag{7.2}$$

where $\Delta(x)$ stands for the unit step function. The probability density of $H(y,t)$ is given by the generalised function $h(y,t)$ as

$$h(y,t) = \int_{-\infty}^{+\infty} \delta\left[y - \varphi(x,t)\right]\, w(x)\, dx. \tag{7.3}$$

The extension we need to make compared to [40] is to specify the quantities needed to describe the neutron multiplication. We assume an infinite multiplying medium with an infinite fission chamber embedded into it. It is assumed that there are only two possible neutron reactions. Either the neutron is absorbed in the detector, in which case it induces a signal but no new neutrons are generated, or it is absorbed in the material, in which case new neutrons can be generated by fission, but no detector signal is generated. Obviously, the condition that there are no new neutrons generated in the detection process can be abandoned easily. At any rate, since as usual it is assumed that only a small fraction of all reactions in the system takes place in the detector, this simplification has no practical consequences to the results. Delayed neutrons will not be taken account, all fission neutrons will be assumed to be prompt. This simplification was made to make the treatment more transparent, and can also be abandoned. Some of the consequences of this simplification will be touched upon when discussing the results.

Hence, the parameters used will be the intensity of the detection, λ_d, and the intensity of reaction in the material, $\lambda_m = \lambda_c + \lambda_f$. The reaction in the material (absorption included with intensity λ_c) will lead to k new neutrons with probability $f(k)$ which is different from the probability $p(k)$ of the number of neutrons from a fission event, since in this latter the pure absorption events are not included. The total intensity of neutron reaction (either detection or reaction in the material) is

$$\lambda_d + \lambda_m = \lambda_r.$$

First, we will be dealing with the probability density function of the detector signal, existing in the detector at time t, assuming one single source neutron in the system at $t = 0$. From the above, the probability that no neutron reaction occurs in the time interval $[0, t]$ is given by $e^{-\lambda_r t}$. We will seek the probability of the event that the detector signal $\boldsymbol{\eta}(t) \geq 0$ is less than or equal to y, if its value was zero at $t = 0$ and that the number of neutrons $\mathbf{n}(t)$ in the multiplying system is equal to n, if its value at $t = 0$ was one:

$$\mathcal{P}\left\{\boldsymbol{\eta}(t) \leq y, \mathbf{n}(t) = n | \boldsymbol{\eta}(0) = 0, \mathbf{n}(0) = 1\right\} = P_1(y, n, t\,|0, 1) = \int_{-\infty}^{y} p_1(y', n, t\,|0, 1)\, dy'. \tag{7.4}$$

For the density $p_1(y,n,t|0,1)$ the following integral backward equation can be written down[2]

$$p_1(y,n,t\,|0,1) = e^{-\lambda_r t}\,\delta(y)\,\delta_{n,1} + \delta_{n,0}\lambda_d \int_0^t e^{-\lambda_r(t-t')} h(y,t')\;dt' +$$

$$\lambda_m \sum_k f(k) \int_0^t e^{-\lambda_r(t-t')}\;dt' \int_{y_1+y_2\cdots+y_k=y} \cdots \int \sum_{n_1+\cdots+n_k=n} \prod_{\ell=1}^{k} p_1(y_\ell, n_\ell, t'\,|0,1)\;dy_\ell. \tag{7.5}$$

Introducing the characteristic functions

$$\widetilde{p}_1(\omega,n,t\,|0,1) = \int_{-\infty}^{+\infty} e^{\imath\,\omega\,y}\,p_1(y,n,t\,|0,1)\;dy, \tag{7.6}$$

and

$$\chi(\omega,t) = \int_{-\infty}^{+\infty} e^{\imath\,\omega\,y}\,h(y,t)\;dy =$$

$$\int_{-\infty}^{+\infty}\int_{-\infty}^{+\infty} e^{\imath\omega y}\,\delta\left[y-\varphi(x,t)\right]\;dy\,w(x)\;dx = \int_{-\infty}^{+\infty} e^{\imath\omega\varphi(x,t)}\,w(x)\;dx, \tag{7.7}$$

one obtains from (7.5) the following equation:

$$\widetilde{p}_1(\omega,n,t\,|0,1) = e^{-\lambda_r t}\,\delta_{n,1} + \lambda_d \int_0^t e^{-\lambda_r(t-t')}\chi(\omega,t')\;dt'\;\delta_{n,0} +$$

$$\lambda_m \sum_k f(k) \int_0^t e^{-\lambda_r(t-t')}\;dt' \sum_{n_1+\cdots+n_k=n} \prod_{\ell=1}^{k} \widetilde{p}_1(\omega,n_\ell,t'\,|0,1). \tag{7.8}$$

Defining the generating function

$$g_1(\omega,z,t\,|0,1) = \sum_{n=0}^{\infty} \widetilde{p}_1(\omega,n,t\,|0,1)\,z^n, \tag{7.9}$$

one arrives at the equation

$$g_1(\omega,z,t\,|\,0,1) = z\,e^{-\lambda_r t} + \lambda_d \int_0^t e^{-\lambda_r(t-t')}\,\chi(\omega,t')\;dt' +$$

$$\lambda_m \int_0^t e^{-\lambda_r(t-t')}\,q[g_1(\omega,z,t'\,|\,0,1]\;dt', \tag{7.10}$$

where

$$q(z) = \sum_{k=0}^{\infty} f(k)\;z^k. \tag{7.11}$$

[2]The subscript "1" here refers to the fact that $p_1(y,n,t|0,1)$ is a "one-point" density, concerning the distribution or density of the random variables at one given time point. This is to distinguish from the case of two-point densities, which will be later needed to treat the covariance function, and which will be denoted by a subscript "2".

Since we are only interested in the probability distribution of the detector signal whereas the number of the neutrons in the system is uninteresting, we introduce the characteristic function[3]

$$\pi_1(\omega, t|0, 1) = g_1(\omega, 1, t \,|\, 0, 1) = \int_{-\infty}^{+\infty} e^{\imath\omega y}\, p_1(y, t \,|\, 0, 1)\, dy, \tag{7.12}$$

where

$$p_1(y, t \,|\, 0, 1) \equiv \sum_{n=0}^{\infty} p_1(y, n, t \,|\, 0, 1)$$

for which one obtains

$$\pi_1(\omega, t \,|\, 0, 1) = e^{-\lambda_r t} + \lambda_d \int_0^t e^{-\lambda_r (t-t')}\, \chi(\omega, t')\, dt' +$$

$$\lambda_m \int_0^t e^{-\lambda_r (t-t')}\, q[\pi_1(\omega, t' \,|\, 0, 1)]\, dt'. \tag{7.13}$$

It is worth noting that (7.13) could have been derived in a simpler way, by starting directly with a backward-type master equation for $p_1(y, t \,|\, 0, 1)$. This would have simplified both the formalism and the derivation. However, the more general equation for $p_1(y, n, t \,|\, 0, 1)$ was derived to show the full potentials of the formalism. From the density $p_1(y, n, t \,|\, 0, 1)$, also the mixed moments, such as the covariance between the neutron number in the system and the detector current, can be calculated.

From the integral equation (7.13) one can also derive a full differential equation by derivation. Relationships between the various moments of the density function $p_1(y, t\,|0, 1)$ with respect to y can be calculated by taking the derivatives of (7.13) w.r.t. ω at $\omega = 0$. However, we will need the relationships for the case when the neutron distribution in the system is maintained by a stationary neutron source, hence we have to connect the above, single-particle induced distributions, to the source-induced distribution, and then deriving the equations for the first two moments and for the auto-covariance of the stationary detector current.

7.1.2 Subcritical system driven by a stationary source

We assume a subcritical system in the point model description, i.e. the detector and the source homogeneously embedded into the system. The source has a homogeneous Poisson distribution and intensity s_0. In the previous Section we derived an equation for the characteristic function $\pi_1(\omega, t \,|\, 0,\, 1)$ of the detector signal $\boldsymbol{\eta}(t)$ at time $t \geq 0$ which is induced by emitting one single neutron to the system at time $t = 0$. Let us now determine the one-point density $P_1(y, t \,|\, 0)$ of the event that, assuming a continuous neutron source, the value of the detector signal $\boldsymbol{\eta}(t)$ at $t \geq 0$ will lie in the interval $(y, y + dy)$, on the condition that at $t = 0$ the value of the signal was zero.

[3]In the continuation we will use the convention that the single-particle induced densities will be denoted by p and their characteristic functions by π, whereas the source-induced densities by P and their characteristic function by Π.

It is easy to confirm that $P_1(y,t\,|\,0)$ obeys the equation

$$P_1(y,t\,|\,0) = e^{-s_0 t}\,\delta(y) +$$

$$s_0 \int_0^t e^{-s_0(t-t')} \int_0^y p_1(y-y',t'\,|\,0,\,1)\,P_1(y',t'\,|\,0)\;dy'\;dt'. \tag{7.14}$$

From this one obtains for the characteristic function

$$\Pi_1(\omega,t\,|\,0) = \int_{-\infty}^{+\infty} e^{\imath\, y\,\omega}\,P_1(y,t\,|\,0)\;dy \tag{7.15}$$

the equation

$$\Pi_1(\omega,t\,|\,0) = e^{-s_0 t} + s_0 \int_0^t e^{-s_0(t-t')}\,\pi_1(\omega,t'\,|0,\,1)\,\Pi_1(\omega,t'\,|\,0)\;dt'. \tag{7.16}$$

With differentiation one obtains the equation

$$\frac{d\Pi_1(\omega,t\,|\,0)}{dt} = -s_0\,\Pi_1(\omega,t\,|\,0) + s_0\,\pi_1(\omega,t\,|0,\,1)\,\Pi_1(\omega,t\,|\,0) \tag{7.17}$$

whose solution, accounting for the initial condition

$$\Pi_1(\omega,0\,|\,0) = 1$$

reads as

$$\Pi_1(\omega,t\,|\,0) = \exp\left\{-s_0 \int_0^t [1-\pi_1(\omega,t'\,|\,0,\,1)]\;dt'\right\}. \tag{7.18}$$

It is practical to introduce the logarithmic characteristic function

$$\mathbb{K}(\omega,t) = \ln\Pi_1(\omega,t\,|\,0) = s_0 \int_0^t [\pi_1(\omega,t'\,|\,0,\,1)-1]\;dt', \tag{7.19}$$

from which the cumulants of the detector signal $\boldsymbol{\eta}(t)$ can be derived as

$$\kappa_n(t\,|\,0) = \frac{1}{\imath^n}\left[\frac{\partial^n \mathbb{K}(\omega,t)}{\partial\omega^n}\right]_{\omega=0} = \frac{1}{\imath^n}\,s_0 \int_0^t \left[\frac{\partial^n \pi_1(\omega,t'\,|0,\,1)}{\partial\omega^n}\right]_{\omega=0} dt'. \tag{7.20}$$

In a subcritical system with a stationary source, we need the stationary values of these quantities, which is given by the asymptotic formula

$$\lim_{t\to\infty}\Pi_1(\omega,t\,|\,0) = \Pi_1^{(st)}(\omega) = \exp\left\{-s_0 \int_0^\infty [1-\pi_1(\omega,t\,|\,0,\,1)]\;dt\right\}. \tag{7.21}$$

From (7.21) and (7.13), the various moments of the detector current can be calculated by expressing the source induced moments as integrals over the single-particle induced moments, and deriving equations for the latter by differentiating (7.13) w.r.t. ω. Since our goal is to calculate the temporal covariance function, these derivations will not be given here. Instead, for the details the reader is referred to [41].

7.2 Auto-covariance of the stationary detector current

In order to explore the temporal correlations between the incoming events, we need to determine the auto-covariance of the stationary detector signal,

$$\lim_{t\to\infty} \mathbf{Cov}\left\{\boldsymbol{\eta}(t-\theta)\,\boldsymbol{\eta}(t)\right\} = \mathbf{Cov}(\theta),$$

which is expected to carry information on the multiplying medium. Hence, it is clearly of interest to derive it, despite an involved formalism and complicated derivation. For the calculation of the auto-covariance, one has to determine the two-point probability[4]

$$P_2\left(y_1, y_2, n_1, n_2, t_1, t_2\,|0\right)\; dy_1\; dy_2 \tag{7.22}$$

of the event that at time $t_1 = t-\theta$ the detector current is in the interval (y_1, y_1+dy_1) and the number of the neutrons is n_1; and that at $t_2 = t$ the detector current is in the interval (y_2, y_2+dy_2) while the number of neutrons is n_2, for the case that the system was driven by a stationary source which was switched on at time $t=0$ when there were no neutrons in the system and the detector current was equal to zero. To write down an equation for P_2, one will also need the probability $p_2\left(y_1, y_2, n_1, n_2, t-\theta, t\,|1\right)$ which is the same as above, but for the case that the process was generated by one single neutron, emitted into the system at time $t=0$. With the help of Fig. 7.1,

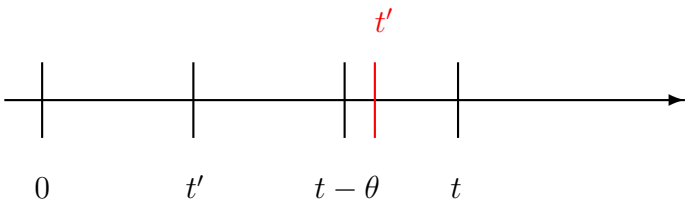

Figure 7.1: Arrangement of the time points t', $t_1 = t-\theta$, and $t_2 = t$, for two possible values of t': one lying in $[0, t-\theta]$, shown in black, and one lying in $[t-\theta, t]$, shown in red in the on-line version. These two alternatives correspond to two different terms in Eq. (7.23).

the following master equation can be written down:

$$P_2\left(y_1, y_2, n_1, n_2, t-\theta, t\,|0\right) = e^{-s_0 t}\,\delta(y_1)\,\delta(y_2)\,\delta_{n_1,0}\,\delta_{n_2,0} +$$

$$s_0 \int_0^t e^{-s_0 t'} \Bigg[\Delta(t-\theta-t') \int_0^{y_1}\int_0^{y_2} \sum_{n_1'=0}^{n_1}\sum_{n_2'=0}^{n_2} p_2\left(y_1', y_2', n_1', n_2', t-\theta-t', t-t'\,|1\right) \times$$

$$P_2\left(y_1-y_1', y_2-y_2', n_1-n_1', n_2-n_2', t-\theta-t', t-t'\,|0\right)\; dy_1'\, dy_2' +$$

$$+\Delta(t'-t+\theta)\,\delta(y_1)\delta_{n_1,0} \times \tag{7.23}$$

$$\int_0^{y_2} \sum_{n_2'=0}^{n_2} p_1\left(y_2', n_2', t-t'\,|1\right)\; P_1\left(y_2-y_2', n_2-n_2', t-t'\,|0\right)\; dy_2' \Bigg]\; dt',$$

[4] As mentioned previously, the subscript "2" here stands to indicate that we are dealing with a two-point distribution or density, whereas the use of capital P indicates that the distribution was induced by a stationary source.

which, after the change of variables $t' \to t - t'$ and $t - t' \to t'$ takes the form

$$P_2\,(y_1, y_2, n_1, n_2, t-\theta, t\,|0) = e^{-s_0 t}\,\delta(y_1)\,\delta(y_2)\,\delta_{n_1,0}\,\delta_{n_2,0} +$$

$$s_0 \int_0^t e^{-s_0(t-t')} \Bigg[\Delta(t'-\theta) \int_0^{y_1} \int_0^{y_2} \sum_{n_1'=0}^{n_1} \sum_{n_2'=0}^{n_2} p_2\,(y_1', y_2', n_1', n_2', t'-\theta, t'\,|1) \times$$

$$P_2\,(y_1 - y_1', y_2 - y_2', n_1 - n_1', n_2 - n_2', t'-\theta, t'\,|0)\; dy_1'\, dy_2' +$$

$$\Delta(\theta - t')\,\delta(y_1)\;\delta_{n_1,0}\;\times \tag{7.24}$$

$$\int_0^{y_2} \sum_{n_2'=0}^{n_2} p_1\,(y_2', n_2', t'\,|1)\;\; P_1\,(y_2 - y_2', n_2 - n_2', t'\,|0)\;\; dy_2' \Bigg]\; dt'.$$

For the two-point, single particle induced density $p_2\,(y_1, y_2, n_1, n_2, t-\theta, t\,|1)$ appearing in (7.24) one can write, similarly to (7.5) the equation

$$p_2\,(y_1, y_2, n_1, n_2, t-\theta, t\,|1) = e^{-\lambda_r t}\,\delta(y_1)\,\delta(y_2)\,\delta_{n_1,1}\,\delta_{n_2,1} +$$

$$\lambda_d \int_0^t e^{-\lambda_r(t-t')}\,[\Delta(t'-\theta)\,h(y_1, t'-\theta)\,h(y_2, t') +$$

$$\Delta(\theta - t')\,\delta(y_1)\,h(y_2, t')]\;\delta_{n_1,0}\,\delta_{n_2,0}\;dt' +$$

$$\lambda_m \int_0^t e^{-\lambda_r(t-t')} \Bigg[\Delta(t'-\theta) \sum_{k=0}^{\infty} f(k) \int\cdots\int_{y_{1,1}+\cdots+y_{1,k}=y_1} \int\cdots\int_{y_{2,1}+\cdots+y_{2,k}=y_2} \times$$

$$\sum_{n_{1,1}+\cdots+n_{1,k}=n_1} \sum_{n_{2,1}+\cdots+n_{2,k}=n_2} \prod_{\ell=1}^{k} p_2\,(y_{1,\ell}, y_{2,\ell}, n_{1,\ell}, n_{2,\ell}, t'-\theta, t'\,|1)\;\; dy_{1,\ell}\, dy_{2,\ell} +$$

$$\Delta(\theta - t')\,\delta(y_1)\;\delta_{n_1,0}\;\times \tag{7.25}$$

$$\sum_{k=0}^{\infty} f(k) \int\cdots\int_{y_{2,1}+\cdots+y_{2,k}=y_2} \sum_{n_{2,1}+\cdots+n_{2,k}=n_2} \prod_{\ell=1}^{k} p_1\,(y_{2,\ell}, n_{2,\ell}, t'\,|1)\;\; dy_{2,\ell} \Bigg]\; dt'.$$

The one-point, source-induced density $P_1\,(y_2, n_2, t'\,|0)$ appearing in (7.24) is defined by the equation

$$P_1\,(y, n, t\,|0) = e^{-s_0 t}\delta(y)\,\delta_{n,0} +$$

$$s_0 \int_0^t e^{-s_0(t-t')} \int_0^{y} \sum_{n'=0}^{n} p_1(y', n', t'\,|0, 1)\,P_1\,(y - y', n - n', t;\,|0)\;\; dt', \tag{7.26}$$

in which the single-particle induced one-point density $p_1(y_1, n_1, t'\,|0, 1)$ is given by the equation, derived from (7.5) as

$$p_1(y, n, t\,|0, 1) = e^{-s_0 t}\,\delta(y)\delta_{n,1}\; + \lambda_d\,\delta_{n,0} \int_0^t e^{-s_0(t-t')}\,h(y, t')\;dt' +$$

$$\lambda_m \sum_k f(k) \int_0^t e^{-s_0(t-t')} \int\cdots\int_{y_1+\cdots+y_k=y} \sum_{n_1+\cdots+n_k=n} \prod_{\ell=1}^{k} p_1(y_\ell, n_\ell, t' \,|0,1)\; dy_\ell\; dt'. \qquad (7.27)$$

Introducing the characteristic function

$$\widetilde{P}_1(\omega, n, t|0) = \int_{-\infty}^{+\infty} e^{\imath\omega y}\, P_1(y, n, t|0)\; dy$$

and its generating function

$$\mathbb{G}_1(\omega, z, t\,|0) = \sum_{n=0}^{\infty} \widetilde{P}_1(\omega, n, t|0)\; z^n, \qquad (7.28)$$

by employing the procedure of Sect. 7.1.2, one can write

$$\mathbb{G}_1(\omega, z, t\,|\,0) = e^{-s_0 t} + s_0 \int_0^t e^{-s_0(t-t')}\, g_1(\omega, z, t'\,|1)\, \mathbb{G}_1(\omega, z, t'\,|\,0)\; dt' \qquad (7.29)$$

whose solution is obtained as

$$\mathbb{G}_1(\omega, z, t\,|0) = \exp\left\{-s_0 \int_0^t [1 - g_1(\omega, z, t'\,|0,1)\; dy]\right\}. \qquad (7.30)$$

Here, following from (7.10), $g_1(\omega, z, t|0, 1)$ is given as

$$g_1(\omega, z, t|0,1) = z\, e^{-\lambda_r t} +$$

$$\lambda_d \int_0^t e^{-\lambda_r(t-t')}\, \chi(\omega, t')\; dt' + \lambda_m \int_0^t e^{-\lambda_r(t-t')}\, q[g_1(\omega, z, t'\,|\,0,1)]\; dt'. \qquad (7.31)$$

It is worth noting that by the substitutions

$$g_1(\omega, 1, t'\,|0,1) = \pi_1(\omega, t'\,|0,1) \qquad \text{and} \qquad \mathbb{G}_1(\omega, 1, t\,|0) = \Pi_1(\omega, t\,|\,0)$$

Eq. (7.30) reverts to (7.18), as is expected.

7.2.1 Derivation of the generating function

To derive the auto-covariance of the detector signal we will use the generating function

$$\mathbb{G}_2(\omega_1, \omega_2, z_1, z_2, t-\theta, t\,|0) =$$

$$\int_{-\infty}^{+\infty}\int_{-\infty}^{+\infty} e^{\imath\omega_1 y_1}\, e^{\imath\omega_2 y_2} \sum_{n_1=0}^{\infty}\sum_{n_2=0}^{\infty} P_2\,(y_1, y_2, n_1, n_2, t-\theta, t\,|0)\;\; z_1^{n_1}\, z_2^{n_2}\; dy_1\; dy_2 \qquad (7.32)$$

which obeys the integral equation

$$\mathbb{G}_2(\omega_1, \omega_2, z_1, z_2, t-\theta, t\,|0) = e^{-s_0 t} +$$

$$s_0 \int_0^t e^{-s_0(t-t')}\; [\Delta(t'-\theta)\, g_2(\omega_1, \omega_2, z_1, z_2, t'-\theta, t'\,|1)\, \mathbb{G}_2(\omega_1, \omega_2, z_1, z_2, t'-\theta, t'\,|0) +$$

$$\Delta(\theta - t')\, g_1(\omega_2, z_2, t'\,|1)\, \mathbb{G}_1(\omega_2, z_2, t'\,|0)]\ dt'. \tag{7.33}$$

From (7.25) it is seen that g_2 obeys the equation

$$g_2(\omega_1, \omega_2, z_1, z_2, t-\theta, t\,|1) = e^{-\lambda_r t}\, z_1\, z_2 +$$

$$\lambda_d \int_0^t e^{-\lambda_r(t-t')}\, [\Delta(t'-\theta)\, \chi(\omega_1, t'-\theta)\, \chi(\omega_2, t') + \Delta(\theta - t')\, \chi(\omega_2, t')]\ dt' + \tag{7.34}$$

$$\lambda_m \int_0^t e^{-\lambda_r(t-t')}\, \{\Delta(t'-\theta)\, q\, [g_2(\omega_1, \omega_2, z_1, z_2, t'-\theta, t'\,|1)] + \Delta(\theta - t')\, q\, [g_1(\omega_2, z_2, t'\,|1)]\}\ dt',$$

whereas the one-point generating functions g_1 and $\mathbb{G}_1$ are given by (7.31) and (7.30).

Since we are only interested in the covariance of the detector current irrespective of the neutron number, we need the generation functions only for the cases $z_1 = z_2 = 1$. Introduce the notations

$$\begin{aligned} g_1(\omega, 1, t\,|1) &= \pi_1(\omega, t\,|1), & (7.35)\\ g_2(\omega_1, \omega_2, 1, 1, t-\theta, t\,|1) &= \pi_2(\omega_1, \omega_2, t-\theta, t\,|1), & (7.36)\\ \mathbb{G}_1(\omega, 1, t\,|\,0) &= \Pi_1(\omega, t\,|\,0), & (7.37)\\ \mathbb{G}_2(\omega_1, \omega_2, 1, 1, t-\theta, t\,|0) &= \Pi_2(\omega_1, \omega_2, t-\theta, t\,|0). & (7.38) \end{aligned}$$

For the derivation of the auto-covariance, the following generator function equations will be used:

$$\pi_1(\omega, z, t|0, 1) = e^{-\lambda_r t} +$$

$$\lambda_d \int_0^t e^{-\lambda_r(t-t')}\, \chi(\omega, t')\ dt' + \lambda_m \int_0^t e^{-\lambda_r(t-t')}\, q[\pi_1(\omega, t'\,|\,0, 1)]\ dt', \tag{7.39}$$

$$\pi_2(\omega_1, \omega_2, t-\theta, t\,|1) = e^{-\lambda_r t} +$$

$$\lambda_d \int_0^t e^{-\lambda_r(t-t')}\, [\Delta(t'-\theta)\, \chi(\omega_1, t'-\theta)\, \chi(\omega_2, t') + \Delta(\theta - t')\, \chi(\omega_2, t')]\ dt' + \tag{7.40}$$

$$\lambda_m \int_0^t e^{-\lambda_r(t-t')}\, \{\Delta(t'-\theta)\, q\, [\pi_2(\omega_1, \omega_2, t'-\theta, t'\,|1)] + \Delta(\theta - t')\, q\, [\pi_1(\omega_2, t'\,|1)]\}\ dt',$$

$$\Pi_1(\omega, t\,|\,0) = e^{-s_0 t} + s_0 \int_0^t e^{-s_0(t-t')}\, \pi_1(\omega, t'\,|1)\, \Pi_1(\omega, t'\,|\,0)\ dt', \tag{7.41}$$

$$\Pi_2(\omega_1, \omega_2, t-\theta, t\,|0) = e^{-s_0 t} +$$

$$s_0 \int_0^t e^{-s_0(t-t')}\ [\Delta(t'-\theta)\, \pi_2(\omega_1, \omega_2, t'-\theta, t'\,|1)\, \Pi_2(\omega_1, \omega_2, t'-\theta, t'\,|0) +$$

$$\Delta(\theta - t')\, \pi_1(\omega_2, t'\,|1)\, \Pi_1(\omega_2, t'\,|0)]\ dt'. \tag{7.42}$$

From these, together with the substitutions $\omega_1 = \omega_2 = 0$ as well as accounting for the elementary relations

$$s_0 \int_0^t e^{-s_0(t-t')}\, \Delta(\theta - t')\ dt' = -e^{-s_0 t} + e^{-s_0(t-\theta)}$$

and

$$(\lambda_d + \lambda_m) \int_0^t e^{-\lambda_r (t-t')}\, \Delta(\theta - t')\, dt' = -e^{-\lambda_r t} + e^{-\lambda_r (t-\theta)},$$

we obtain

$$\pi_2(0, \omega_2, t-\theta, t\,|1) = \pi_1(\omega_2, t\,|1), \tag{7.43}$$

$$\pi_2(\omega_1, 0, t-\theta, t\,|1) = \pi_1(\omega_1, t-\theta\,|1), \tag{7.44}$$

$$\Pi_2(0, \omega_2, t-\theta, t\,|0) = \Pi_1(\omega_2, t\,|0), \tag{7.45}$$

$$\Pi_2(\omega_1, 0, t-\theta, t\,|0) = \Pi_1(\omega_1, t-\theta\,|0). \tag{7.46}$$

Our goal is the calculation of the auto-covariance function of the stationary detector signal,

$$\mathbf{Cov}(\theta) = \lim_{t\to\infty} \left\{ \frac{1}{\imath^2} \left[\frac{\partial^2 \Pi_2(\omega_1, \omega_2, t-\theta, t\,|0)}{\partial\omega_1 \partial\omega_2} \right]_{\substack{\omega_1=0 \\ \omega_2=0}} \right\} -$$

$$\lim_{t\to\infty} \left\{ \left[\frac{1}{\imath} \frac{\partial \Pi_1(\omega_1, t-\theta\,|0)}{\partial\omega_1} \right]_{\omega_1=0} \left[\frac{1}{\imath} \frac{\partial \Pi_1(\omega_2, t\,|0)}{\partial\omega_2} \right]_{\omega_2=0} \right\}. \tag{7.47}$$

One immediately obtains

$$\lim_{t\to\infty} \left\{ \left[\frac{1}{\imath} \frac{\partial \Pi_1(\omega_1, t-\theta\,|0)}{\partial\omega_1} \right]_{\omega_1=0} \left[\frac{1}{\imath} \frac{\partial \Pi_1(\omega_2, t\,|0)}{\partial\omega_2} \right]_{\omega_2=0} \right\} = \left[I_1^{(st)} \right]^2, \tag{7.48}$$

since one has that

$$\lim_{t\to\infty} \left[\frac{1}{\imath} \frac{\partial \Pi_1(\omega, t\,|0)}{\partial\omega} \right]_{\omega=0} = s_0 \int_0^\infty i_1(t)\, dt = s_0\, \frac{\lambda_d}{\alpha}\, \widetilde{\phi}(0) = I_1^{(st)},$$

where $\widetilde{\phi}(0)$ is defined as

$$\widetilde{\phi}(0) = \int_0^\infty \phi(t)\, dt.$$

To simplify the formalism, introduce the notations

$$\mathbf{M}(t, \theta) = \frac{1}{\imath^2} \left[\frac{\partial^2 \Pi_2(\omega_1, \omega_2, t-\theta, t\,|0)}{\partial\omega_1 \partial\omega_2} \right]_{\omega_1=\omega_2=0} \tag{7.49}$$

and

$$\mathbf{m}(t, \theta) = \frac{1}{\imath^2} \left[\frac{\partial^2 \pi_2(\omega_1, \omega_2, t-\theta, t\,|0)}{\partial\omega_1 \partial\omega_2} \right]_{\omega_1=\omega_2=0}. \tag{7.50}$$

Accounting for (7.43) - (7.46), from the integral equation (7.42) one obtains

$$\mathbf{M}(t, \theta) = s_0 \int_0^t \Delta(t'-\theta) \left\{ \mathbf{m}(t', \theta) + \frac{1}{\imath} \left[\frac{\partial \pi_1(\omega_1, t'-\theta\,|1)}{\partial\omega_1} \right]_{\omega_1=0} \frac{1}{\imath} \left[\frac{\partial \Pi_1(\omega_2, t'\,|0)}{\partial\omega_2} \right]_{\omega_2=0} + \right.$$

$$\left. \frac{1}{\imath} \left[\frac{\partial \pi_1(\omega_2, t'\,|1)}{\partial\omega_2} \right]_{\omega_2=0} \frac{1}{\imath} \left[\frac{\partial \Pi_1(\omega_1, t'-\theta\,|0)}{\partial\omega_1} \right]_{\omega_1=0} + \mathbf{M}(t', \theta) \right\} dt'. \tag{7.51}$$

From the definitions in Sect. 7.1.2 it follows that

$$\frac{1}{\imath}\left[\frac{\partial\pi_1(\omega,t\,|1)}{\partial\omega}\right]_{\omega=0} = i_1(t) \qquad \text{and} \qquad \frac{1}{\imath}\left[\frac{\partial\Pi_1(\omega,t\,|1)}{\partial\omega}\right]_{\omega=0} = I_1(t), \tag{7.52}$$

with which (7.51) can be brought to the simpler form

$$\mathbf{M}(t,\theta) = s_0 \int_\theta^t \left[\mathbf{m}(t',\theta) + i_1(t'-\theta)\, I_1(t') + i_1(t')\, I_1(t'-\theta) + \mathbf{M}(t',\theta)\right]\, dt', \tag{7.53}$$

from which it is seen that

$$\mathbf{M}(\theta,\theta) \equiv 0. \tag{7.54}$$

Differentiation of the integral equation (7.53) w.r.t. t yields

$$\frac{d\mathbf{M}(t,\theta)}{dt} = s_0\, \left[\mathbf{m}(t,\theta) + i_1(t-\theta)\, I_1(t) + i_1(t)\, I_1(t-\theta)\right], \tag{7.55}$$

which can easily be solved by quadrature. One can immediately write

$$\mathbf{M}(\infty,\theta) = s_0 \int_\theta^\infty \mathbf{m}(t,\theta)\, dt + \left[I_1^{(st)}\right]^2, \tag{7.56}$$

since

$$\int_\theta^\infty \left[i_1(t-\theta)\, I_1(t) + I_1(t-\theta)\, i_1(t)\right]\, dt = \int_\theta^\infty \frac{d}{dt}\, \left[I_1(t-\theta)\, I_1(t)\right]\, dt = \left[I_1^{(st)}\right]^2.$$

From (7.47) then it follows that

$$\mathbf{Cov}(\theta) = s_0 \int_\theta^\infty \mathbf{m}(t,\theta)\, dt. \tag{7.57}$$

It remains to calculate the mixed moment $\mathbf{m}(t,\theta)$. From the definition (7.50) and accounting for the relations (7.43) one obtains

$$\mathbf{m}(t,\theta) = \lambda_d \int_\theta^t e^{-\lambda_r(t-t')}\, \phi(t'-\theta)\, \phi(t')\, dt' +$$

$$\lambda_m \int_\theta^t e^{-\lambda_r(t-t')}\, \left[q_1\, \mathbf{m}(t',\theta) + q_2\, i_1(t')\, i_1(t'-\theta)\right]\, dt', \tag{7.58}$$

in which the function $\phi(t)$ is defined by the second relationship of (**??**). It is seen that

$$\mathbf{m}(\theta,\theta) \equiv 0, \tag{7.59}$$

as expected. Differentiating Eq. (7.58), which is valid for $t \geq \theta$, w.r.t. t leads to the simple differential equation

$$\frac{d\mathbf{m}(t,\theta)}{dt} = -(\lambda_r - q_1\, \lambda_m)\, \mathbf{m}(t,\theta) + \lambda_m\, q_2\, i_1(t-\theta)\, i_1(t) + \lambda_d\, \phi(t-\theta)\, \phi(t), \tag{7.60}$$

in which

$$\lambda_r - q_1\, \lambda_m = \lambda_d + (1-q_1)\lambda_m = \alpha \tag{7.61}$$

is the inverse of the average lifetime of the neutrons. It is practical to solve Eq. (7.60) for a concrete case of the fundamental signal function $\phi(t)$. Such an illustration will be given in the next subsection.

Illustration via a concrete case

We will calculate the stationary value of the auto-covariance function of the detector signal again for the concrete case treated in the foregoing, i.e. when assuming that one fission in the ionisation chamber induces a current

$$\phi(t) = Q\,\alpha_e^2\,t\,e^{-\alpha_e t}. \tag{7.62}$$

In this case one has

$$i_1(t) = \lambda_d\,Q\,\left[\frac{\alpha_e}{\alpha-\alpha_e}\right]^2\,\left\{e^{-\alpha t} - \left[1-(\alpha-\alpha_e)\;t\right]\;e^{-\alpha_e t}\right\}, \tag{7.63}$$

hence all necessary information is available to write down the solution of the differential equation (7.60), satisfying the initial condition $\mathbf{m}(\theta,\theta) = 0$, from which the auto-covariance $\mathbf{Cov}(\theta)$ can be calculated. Performing the calculations with Mathematica [42] one obtains the result

$$\mathbf{Cov}(\theta) = \frac{1}{4}\,\frac{s_0\,\lambda_d\,\alpha_e\,Q^2}{\alpha\left(\alpha_e^2-\alpha^2\right)^2}\,\left\{\frac{2q_2\,\alpha_e^3\,\lambda_d\,\lambda_m}{\alpha}\,e^{-\alpha\theta} + \right.$$

$$\left.\left[(\alpha_e^2-\alpha^2)^2\,(1+\alpha_e\theta) + q_2\,\left(\alpha^2\,(1+\alpha_e\theta) - \alpha_e^2\,(3+\alpha_e\theta)\right)\,\lambda_d\,\lambda_m\right]\,e^{-\alpha_e\theta}\right\}. \tag{7.64}$$

Eq. (7.64) shows that the auto-covariance of the detector signal exhibits a partial resemblance to the traditional Rossi-alpha formula in that it contains an exponentially decaying term with the prompt neutron decay constant α being the exponent. Further, this term is proportional to the second factorial moment q_2 of the number of neutrons generated in the fission process. At the same time, unlike in the Rossi-alpha formula, there is another exponential term, in which the exponent is related to the pulse shape of the detector response. The coefficient of this term is not constant, rather it contains terms linear in the time lag θ. This indicates that extraction of the parameter α is in principle possible, but is more complicated than in the pulse counting-based Rossi-alpha measurement. The covariance of the Campbelling technique depends on the detector pulse shape, its time constant, and most likely also on the amplitude distribution of the individual pulses (which is not considered in (7.64)).

However, some qualitative and quantitative considerations may be made at this point. The values of α and α_e can be taken from realistic cases. In a measurement of subcritical reactivity, with some representative data of a research reactor, for the deep subcritical reactivity of $\rho = -2.72\,\$$, the value of α was found to be about 600 s^{-1}, and for the lower subcriticality of $\rho = -0.65\,\$$, one had about $\alpha = 250\,s^{-1}$ [37, 43]. On the other hand, with a detector response time between 1 msec to 1μsec, α_e is in the range of 1000 - 10^6. This is valid even if the fluctuations in the charge collection time due to the fluctuations in the fission fragment mass etc. are taken into account. That is, usually one has $\alpha_e >> \alpha$. Hence the system decay constant is sufficiently separated from the detector decay constant, and they should be distinguishable.

The possibility of extracting the sought parameter α depends of course on the relative weight of the corresponding exponential term in Eq. (7.64). This, in turn, depends on the actual values of α, α_e, λ_d and λ_m. However, it is seen from (7.64) that, due to the occurrence of α in the denominator of the first term, when approaching criticality ($\alpha = 0$), this term, from which the prompt neutron time constant can be determined, becomes dominating. This dominance is hence due to the divergence of the first term, whose reason has already been discussed in Sec. **??**. In other words, in the important case of approaching criticality, the influence of the properties of the detector response function in the detector auto-covariance become negligible.

It is also worth noting that, similarly to the case of the conventional Campbell theorems, the auto-covariance formula (7.64) is also valid whether the pulses are separated or overlapping. Hence the current results may also be said to create a bridge between the pulse and current mode of reactivity determination from the statistical characteristics of the branching process (out of which the current mode was first introduced in this paper). It would be an interesting exercise to evaluate and compare the performance and domain of validity of pulse counting based vs Campbell-like current-mode based reactivity determination methods both by simulations and experiment.

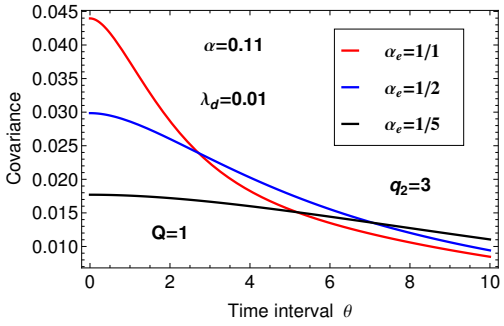

Figure 7.2: The auto-covariance function of the stationary detector signal for three different values of the detector parameter α_e, for the case $\alpha = 0.11$.

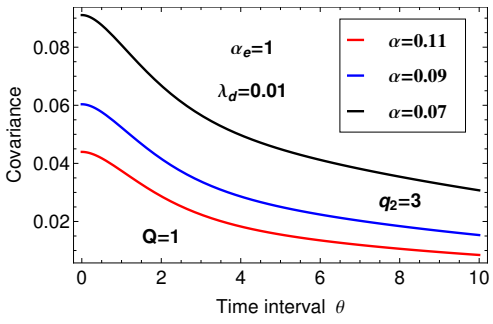

Figure 7.3: The auto-covariance function of the stationary detector signal for three different values of the system parameter α, for the case $\alpha_e = 1$.

For some illustration via model cases, the dependence of the auto-covariance on the time lag θ between two consecutive registrations is shown in Figs 7.2 and 7.3.

Fig. 7.2 shows the effect of the variation of the detector time constant α_e in a medium with fixed system property α, whereas Fig. 7.3 shows three cases with the same α_e, but different system properties α. It is remarkable to note the sensitive dependence of the results on the value of the detector constant α_e, indicating the need for stable detector performance during the measurements. On the other hand, this dependence also gives a possibility to use it to monitor the "healthy" status of the detector from its own signal ("smart detector") in that a change of the shape of the detector autocorrelation signal, or its Fourier transform, the auto power spectral density, can be used to detect deterioration of the detector performance. It has though to be noted that the cases above do not correspond to the approach of criticality, where one of the exponential terms (belonging to the system parameter) becomes dominating.

7.3 Conclusions

The purpose of this study was to investigate the possibility of extracting parameters of interest of the multiplying medium, in particular the prompt neutron decay constant of subcritical cores, from current mode measurements with a fission chamber, similar to that of the pulse counting methods (Rossi-alpha method). It was found that the prompt neutron decay constant can be extracted from the auto-covariance of the detector signal since, similarly to the Rossi-alpha method, it appears as an exponential term in the expression. However, the auto-covariance also contains another exponential that depends on the detector time constant, the pulse shape, and probably also on the amplitude distribution of the individual pulses. Hence, the extraction of the prompt neutron decay constant is not trivial, and requires that the detector pulse shape and time constant are known.

It was also seen, however, that for systems close to critical, the auto-covariance is dominated by the term depending on the prompt neutron time constant, hence knowledge of the detector signal properties is not essential for such measurements. In addition, for all subcriticalities, in principle, the method is applicable for separated and overlapping pulses alike, hence it can be used from low to high fluxes.

In order to be able to apply the method in practice, further theoretical studies and numerical simulations are needed, which is suggested to be performed in the next stage. Inclusion of the delayed neutrons into the model is a logical next step, as well as the exploration of the possibility of deriving formulas that are analogue to the Feynman-alpha measurement. Possibly some experimental studies, or verification of the method, can also be included in later stages, either in Ringhals, or at some of our collaborating partners (such as the Technical University of Budapest, the University of Florida, or CEA).

8. PROPOSAL FOR 2018

1. Investigation of possible baffle jetting in R3 with noise analysis of in-core and ex-core detector signals. The goal is to identify and elaborate suitable methods for detection of incipient baffle jetting, and its localisation inside the core, as well as to monitor its development once its presence is identified.

2. Analysis of vibrations of thimble tubes with axially dependent in-core measurements in various radial positions.

3. Development of a method to use the Eigenvalue Separation in noise analysis for characterising of regional power oscillations and understanding the role of loosely coupled cores in the development of regional instabilities.

4. Further investigations of the possibilities of using fission chamber signals for measurement of subcritical reactivity, such as elaboration of the equivalent of the Feynman-alpha method of pulse counting, and accounting for delayed neutrons.

5. Evaluation of new ex-core measurements for beam mode and tilting mode vibrations in R3 or R4.

9. ACKNOWLEDGEMENT

This one-year contract was performed by funding from Ringhals Vattenfall AB, contract No. 663628-054. Contact person from Ringhals was Dr. Henrik Nylén. The measurements reported in Chapter 6 were designed and executed by our collaborating partners in EPFL Lausanne/PSI: Mathieu Hursin, Oskari Pakari and Vincent Lamirand.

REFERENCES

[1] V. Dykin, C. Montalvo, N. Tran, H. Nylén, and I. Pázsit, "*Ringhals Diagnostics and Monitoring, Annual Research Report 2015*," CTH-NT-319/RR-20, Chalmers University of Technology, Göteborg, Sweden, December 2015.

[2] H.-N. Tran, I. Pázsit, and H. Nylén, "Investigation of the ex-core noise induced by fuel assembly vibrations in the Ringhals-3 PWR," *Annals of Nuclear Energy*, vol. 80, pp. 434–446, 2015.

[3] K. A. T. Hoang, V.-C. Cao, V.-K. Hoang, and H.-N. Tran, "Calculation of the ex-core neutron noise induced by individual fuel assembly vibrations in two PWR cores," *Nucl. Sci. Tech.*, vol. 27:86, pp. 1 – 11, 2016.

[4] C. Demazière, "CORE SIM: A multi-purpose neutronic tool for research and education," *Annals of Nuclear Energy*, vol. 38, no. 12, pp. 2698–2718, 2011.

[5] I. Pázsit and C. Demazière, Noise Techniques in Nuclear Systems, vol. 3 of *Handbook of Nuclear Engineering*, ch. 14, pp. 1629–1737. Springer Verlag, Berlin, 2010.

[6] I. Pázsit and O. Glöckler, "On the Neutron Noise Diagnostics of Pressurized Water Reactor Control Rod Vibrations II. Stochastic Vibrations," *Nuclear Science and Engineering*, vol. 88, no. 1, pp. 77–87, 1984.

[7] F. Zylbersztejn, H. N. Tran, I. Pázsit, C. Demazière, and H. Nylén, "On the dependence of the noise amplitude on the correlation length of inlet temperature fluctuations in PWRs," *Annals of Nuclear Energy*, vol. 57, pp. 134–141, 2013.

[8] J. A. Thie, "Core motion monitoring," *Nucl. Technol.*, vol. 45, pp. 5–45, 1979.

[9] I. Pázsit, C. Montalvo-Martin, A. Hernandez-Solis, P. Bernitt Cartemo, and H. Nylén, "Diagnostics of core barrel and fuel assembly vibrations in the Ringhals PWRs," in *In: Proc. NPIC& HMIT 2010*, vol. 2, (Las Vegas, Nevada), pp. 833–844, Nov. 2010.

[10] I. Pázsit, C. Montalvo-Martin, H. Nylén, T. Anderson, A. Hernandez-Solis, and P. Bernitt Cartemo, "Developments in core-barrel motion monitoring and applications to the Ringhals PWR units," *Nuclear Science and Engineering*, vol. 182, no. 2, pp. 213–227, 2016.

[11] I. Pázsit (Ed.), "*Final Report on the Research Project Ringhals Diagnostics and Monitoring, Stage 1*," CTH-RF-122/RR-3, Chalmers University of Technology, Göteborg, Sweden, September 1996.

[12] I. Pázsit, J. Karlsson, and N. Garis, "*Final Report on the Research Project Ringhals Diagnostics and Monitoring, Stage 2*," CTH-RF-132/RR-4, Chalmers University of Technology, Göteborg, Sweden, October 1997.

[13] J. K.-H. Karlsson and I. Pázsit, "*Final Report on the Research Project Ringhals Diagnostics and Monitoring, Stage 3: Analysis of core barrel vibrations in Ringhals 2, 3 and 4 for several fuel cycles*," CTH-RF-135/RR-5, Chalmers University of Technology, Göteborg, Sweden, October 1998.

[14] M. Pázsit and I. Pázsit, "*Final Report on the Analysis of Core Barrel Vibrations in Ringhals PWRs R2, R3 and R4 from Measurements Made in 2005*," Internal report, Chalmers University of Technology, Göteborg, Sweden, 2006.

[15] C. Sunde, C. Demazière, and I. Pázsit, "*Final Report on the Research Project Ringhals Diagnostics and Monitoring, Stage 11*," CTH-NT-206/RR-13, Chalmers University of Technology, Göteborg, Sweden, February 2007.

[16] I. Pázsit, C. Demazière, C. Sunde, P. Bernitt, and A. Hernández-Solís, "*Final Report on the Research Project Ringhals Diagnostics and Monitoring, Stage 12*," CTH-NT-220/RR-14, Chalmers University of Technology, Göteborg, Sweden, August 2008.

[17] I. Pázsit, C. Montalvo Martín, V. Dykin, and T. Tambouratzis, "*Final Report on the Research Project Ringhals Diagnostics and Monitoring, Stage 13*," CTH-NT-230/RR-15, Chalmers University of Technology, Göteborg, Sweden, March 2010.

[18] I. Pázsit, C. Montalvo Martín, V. Dykin, and H. Nylén, "*Final Report on the Research Project Ringhals Diagnostics and Monitoring, Stage 14*," CTH-NT-253/RR-16, Chalmers University of Technology, Göteborg, Sweden, December 2011.

[19] V. Dykin, C. Montalvo Martín, H. Nylén, and I. Pázsit, "*Ringhals Diagnostics and Monitoring, Final Research Report 2012 - 2014*," CTH-NT-304/RR-19, Chalmers University of Technology, Göteborg, Sweden, December 2014.

[20] M. Nilsson, "*Brusmätning för att söka lågfrekventa störningar i R3, Annual Research Report 2015*," Ringhals internal report UH-rapport 2099930 / 2.0, Ringhals AB, Göteborg, Sweden, October 2010.

[21] B. Severinsson, "*"Brusmätningar för analys av härdhöljesvibrationer på Ringhals 3. Utförda mellan 2013-02-26 och 2013-07-05*," Ringhals internal report UH-rapport 2245846 / 2.0, Ringhals AB, Göteborg, Sweden, July 2013.

[22] B. Severinsson, "*Brusmätning för analys av Härdhöljesvibrationer på utförda under 2013*," Ringhals internal report UH-rapport 2233461 / 2.0, Ringhals AB, Göteborg, Sweden, July 2013.

[23] J. A. Thie, *Power Reactor Noise*. La Grange Park, Illinois, USA: American Nuclear Society, 1981.

[24] I. Pázsit, J. Karlsson, and N. S. Garis, "Some developments in core-barrel vibration diagnostics," *Annals of Nuclear Energy*, vol. 25, pp. 1079–1093, 1998.

[25] C. Montalvo-Martin, I. Pázsit, A. Hernandez-Solis, P. Bernitt Cartemo, and H. Nylén, "Surveillance and Diagnostics of the Beam Mode Vibrations of the Ringhals PWRs," in *In: Proc. Int. Conf. PHYSOR 2012 - Advances in Reactor Physics*, (Knoxville, Tennessee, USA), April 2012.

[26] I. Pázsit, H. N. Tran, V. Dykin, and A. Jonsson, "*Research and Development Program in Reactor Diagnostics and Monitoring with Neutron Noise Methods, Stage 18*," Internal Report SSM Internal Report No. 2013:04 ISSN: 2000-0456, Chalmers University of Technology, Göteborg, Sweden, 2013.

[27] M. Pázsit and I. Pázsit, "*Final Report on the Analysis of Core Barrel Vibrations in Ringhals PWRs R2, R3 and R4 from the Measurements Made in 2007/2008*," Internal report, NUCLEUS DATORFYSIK report NDF-09, Göteborg, Sweden, 2008.

[28] F. J. Sweeney, J. March-Leuba, and C. M. Smith, "Contribution of fuel vibrations to ex-core neutron noise during the first and second fuel cycles of the Sequoyah-1 pressurized water reactor," *Prog. Nucl. Energy*, vol. **15**, pp. 283–290, 1985.

[29] R. Perez and D. Wood, "Modeling and Analysis of Neutron Noise from an Ex-Core Detector at a PWR," in *In: Proc. Int. Conf. SMORN-VI*, (Gatlinburg, Tennessee, USA), 1991.

[30] A. Garcia-Berrocal, J. Blázquez, C. Montalvo, and M. Balbás, "Resolving Mechanical Resonances with the Breit-Wigner Formula," *J. Vibr. Control*, vol. 15, pp. 1267–1280, 2009.

[31] C. W. Mayo, "Detailed neutron noise analysis of pressurized water reactor internal vibrations," *Atomkernenergie*, vol. 29, pp. 9–13, 1977.

[32] G. Kosály, "Noise investigations in boiling-water and pressurized-water reactors," *Prog. nucl. Energy*, vol. 5, pp. 145–199, 1980.

[33] P. Lindén and I. Pázsit, "Study of the possibility of determining mass flow of water from neutron activation measurements with flow simulations and neural networks," *Kerntechnik*, vol. 63, pp. 188 – 196, 1998.

[34] P. Lindén, G. Grosshög, and I. Pázsit, "FlowAct, flow rate measurements in pipes with the pulsed-neutron activation method," *Nucl. Technology*, vol. 124, pp. 31 – 51, 1998.

[35] R. Früh, "*Cuve Carrousel*," Annexe au rapport de sécurité IGA LPR 154, École Politechnique Fédérale de Lausanne, Lausanne, Switzerland, 1987.

[36] O. Pakari, "*Induced temporal correlation by bubbles in CARROUSEL*," Internal Report RT-100-113-17-52, École Politechnique Fédérale de Lausanne, Lausanne, Switzerland, August 2017.

[37] I. Pázsit and L. Pál, *Neutron Fluctuations: a Treatise on the Physics of Branching Processes*. New York: Elsevier, 2008.

[38] L. Pál and I. Pázsit, "Theory of neutron noise in a temporally fluctuating multiplying medium," *Nucl. Sci. Engng*, vol. 155, pp. 425 – 440, 2007.

[39] G. Perret, G. Girardin, P. Frajtag, and M. Hursin, "Decay constant and delayed neutron fraction measurements in CROCUS," Tech. Rep. TM-41-14-02 Rev. 1., Paul Scherrer Institut, Villigen, 5232 Switzerland, 2014.

[40] L. Pál, I. Pázsit, and Z. Elter, "Comments on the stochastic characteristics of fission chamber signals," *Nuclear Instruments and Methods in Physics Research Section A: Accelerators, Spectrometers, Detectors and Associated Equipment*, vol. 763, no. 0, pp. 44–52, 2014.

[41] L. Pál and I. Pázsit, "Campbelling-type theory of fission chamber signals generated by neutron chains in a multiplying medium," *Nuclear Instruments and Methods in Physics Research Section A: Accelerators, Spectrometers, Detectors and Associated Equipment*, vol. **794**, no. 1, pp. 90–101, 2015.

[42] "Wolfram Research, Inc., Mathematica, Version 10.0." Champaign, IL., 2014.

[43] I. Pázsit, Y. Kitamura, J. Wright, and T. Misawa, "Calculation of the pulsed Feynman-alpha formulae and their experimental verification," *Annals of Nuclear Energy*, vol. **6**, pp. 896 – 1007, 2005.

APPENDIX

Core-Barrel Motion Monitoring based on the Variational Mode Decomposition

Olvera-Guerrero Omar Alejandro.
División de Ciencias Básicas e Ingeniería, Universidad Autónoma Metropolitana-Iztapalapa, Av. San Rafael Atlixco 186, Col. Vicentina, Cd. de México 09340, México;
oaog@xanum.uam.mx

1. INTRODUCTION

Core-barrel motion monitoring is an area of study related to the observation of stochastic processes in nuclear reactors, and primarily that of the neutron noise, for the purposes of reactor diagnostics. Our main activity in this field is strongly connected with the Ringhals nuclear power plant. Ringhals is the largest nuclear facility in Sweden, with one boiling water reactor (Ringhals-1 or R1), and 3 PWRs (R2-R4). Since 1995 a collaboration project started between Ringhals and the Subatomic and Plasma Physics (earlier: Division of Nuclear Engineering). The long-term goal of this project is to develop, test and apply reactor diagnostic methods by using the measurements from the power plant. This co-operation resulted in the development of methods to solve concrete problems in Ringhals on the one hand, and in publications, conference contributions and PhD exams on the other. A large amount of experience was collected on the various properties of the Ringhals reactors, as well as a large experimental data base is available at our disposal, which was collected during the years. These results have been reported annually. The goal of this work is to study the core-barrel vibrations, and in particular the properties of the pendular (beam mode) vibrations have been performed by Chalmers during a long period, starting in the mid-90's. Currently, the works developed in Chalmers surpasses the performance of previously existing methods significantly by introducing combinations of the time signals of the various ex-core detectors that take into account the symmetries of the various vibration modes, and curve fitting methods to extract the amplitude of the vibration peaks with the highest accuracy. Long term (several cycles) and short-term (during one cycle) behavior of the amplitudes, as well as the influence of the change of the hold-down springs in two units have been monitored for several cycles.

The goal of this internship is to observe new measurements through a Core-Barrel motion methodology (CBM) based on the Variational Mode Decomposition (VMD, a method to decompose a signal into band limited, narrow band intrinsic mode functions (IMFs or simply *modes*)), in order to investigate the effects of the recent power upgrade by 18.6%, which was achieved in R4 in 2015. A comparison with the results from last year could give the first step in a starting trend analysis. The studied CBM-VMD methodology splits the signal of interest into short segments of 15 minutes, these segments are decomposed via the VMD into IMFs, the two IMFs *modes* related to the beam mode are selected for further processing (whereas the remaining extracted *modes* are ignored), a peak detection method is used to detect the local maxima of these selected IMFs, to later infer the amplitude of the maximum peak and the central frequency of the two *modes* of interest (trend analysis). Which from now on are labeled as MODE 1 and MODE 2.

2. Preliminaries

2.1 The Empirical Mode Decomposition (EMD) and its limitations

In 1998, Huang et al., introduced the Hilbert Huang Transform (HHT), also known as the Empirical Mode Decomposition (EMD) [1]. A method to decompose non-stationary signals that stem from non-linear systems. The EMD recursively decomposes a signal into different *modes* known as Intrinsic Mode Functions (IMFs), which are unknown beforehand. The HHT/EMD is a widely used algorithm today. However, there is no exact mathematical model corresponding to this algorithm, and, consequently, the exact properties and limitations of the EMD are unknown. A few limitations of this technique can be highlighted:

i. It has been observed that the EMD is highly sensitive to noise and sampling frequency of the targeted signal.
ii. The EMD has difficulties separating tones of similar frequencies.
iii. The EMD suffers from a serious problem that is known as *mode mixing* [2] and its presence might spoil IMF acquisition.
iv. As mentioned before, a lack of rigorous mathematical theory hinders the properties and limitations of the EMD.

The EMD decomposes a signal into principal *modes*, which are signals with compact support Fourier spectrum. This algorithm is given by the next steps, but first, let x be the signal of interest to decompose into IMFs:

Step 1. Set $k = 0$ and find all extrema of $r_o = x$.

Step 2. Interpolate between minima (maxima) of r_k to obtain the lower (upper) envelope $e_{\min}(e_{\max})$.

Step 3. Compute the mean envelope $m = (e_{\min} + e_{\max})/2$.

Step 4. Compute the IMF candidate $d_{k+1} = r_k - m$.

Step 5. Is d_{k+1} an IMF?

- Yes. Save d_{k+1}, compute the residue $r_{k+1} = x - \sum_{i=1}^{k} d_i$, do $k = k+1$, and treat r_k as input data in step 2.
- No. Treat d_{k+1} as input data in step 2.

Step 6. Continue until the final residue r_k satisfies some predefined stopping criterion.

The refinement process (steps 2 to 5) needed to extract every *mode*, requires a certain number of iterations named as *siftings*. The extracted *modes* d_k, $j = 1, 2, ...N$ decompose x and are in theory, nearly orthogonal to each other. Nonetheless, the resulting decomposition is highly dependent on methods of extremal point finding, interpolation of extremal points into carrier envelopes, and the stopping criteria imposed. The lack of mathematical theory and the aforementioned degrees of freedom reducing the EMD's robustness, leave room for theoretical development and improvement on the robustness of the decomposition [3], [4]. Besides, in

some experiments it has been shown that the EMD shares similarities with wavelets and adaptive filter banks [5].
Despite the limited mathematical understanding and some obvious shortcomings, the EMD method, has had tremendous impact and is widely used in a broad variety of time-frequency signal analysis applications. Such as: Audio engineering analysis [6], Climate signal analysis [7], Boiling Water Reactor stability analysis [8], among many others.

2.2 Intrinsic Mode Functions (IMFs)

With EMD, the core assumption on the individual extracted *modes* is that they have compact Fourier support. In the original description, in such IMFs or *modes*, the number of local extrema and zero-crossings must differ at most by one [1]. The Intrinsic Mode Functions are amplitude-modulated-frequency-modulated (AM-FM) signals, written as:

$$d_k(t) = A_k(t)\cos(\phi_k(t)) \tag{1}$$

Where the phase $\phi_k(t)$ is a non-decreasing function, $\phi'_k(t) \geq 0$, the envelope is non-negative $A_k(t) \geq 0$, and, very importantly, both the envelope $A_k(t)$ and the instantaneous frequency $\omega_k(t) = \phi'_k(t)$ vary much slower than the phase $\phi_k(t)$ [9,10]. On a sufficiently long interval $[t-\delta, t+\delta]$, $\delta \approx 2\pi/\phi'_k(t)$ the mode $d_k(t)$ can be considered to be a pure harmonic signal with amplitude $A_k(t)$ and instantaneous frequency $\phi'_k(t)$ [9] . This definition of IMF is slightly more restrictive than that related to the EMD. The immediate consequence of this IMF assumption is limited bandwidth.

if ω_k is the mean frequency of a mode, then its practical bandwidth increases both, with the maximum deviation of the instantaneous frequency, $\Delta f \sim \max(|\omega_k(t) - \omega_k|)$, and with the rate of change of the instantaneous frequency, $f_{FM} \sim \omega'(t)$, according to Carson's rule: $BW = 2(\Delta f + f_{FM})$ [11]. In addition to this comes the bandwidth of the envelope modulating the amplitude of the FM signal, given by its highest frequency f_{AM} . Hence, the total bandwidth of an IMF is given by:

$$BW = 2(\Delta f + f_{FM} + f_{AM}) \tag{2}$$

Depending on the actual IMF, either of these terms may be dominant, as illustrated in Figure 1. To address the handicaps of the EMD method, Dragomiretskiy and Zosso [12] developed and entirely new, fully intrinsic and adaptive, Variational Mode Decomposition (VMD) method, the minimization leads to a decomposition of a signal into its principal IMFs or *modes*. The variational model they proposed, determines the relevant bands adaptively, and estimates the corresponding modes concurrently, thus properly balancing errors between them. Motivated by the narrow-band properties corresponding to the previously defined IMF definition, the variational model looks for an ensemble of modes that reconstruct the given input signal optimally (either exactly or in a least-squares sense), while each being band-limited about a center frequency estimated on-line. The variational model can address the presence of noise in the input signal. The close relationship between the VMD optimization scheme and the Wiener filter suggests that this variational model has optimality in dealing with noise.

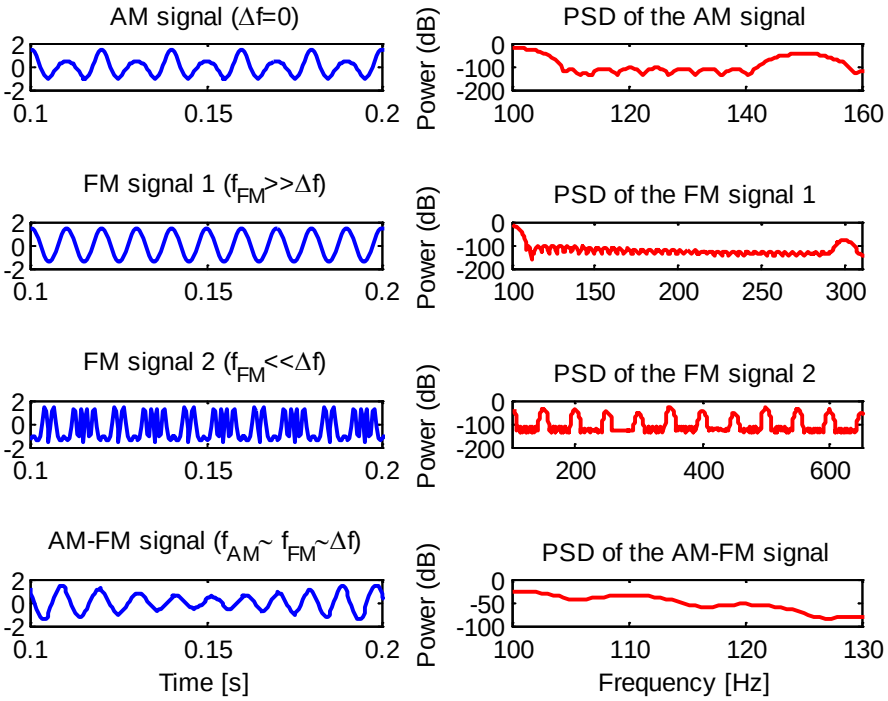

Figure 1. AM-FM signals with limited bandwidth. Here, the signal that was used is $f(t) = (1 + 0.5\cos(2\pi f_{AM} t))\cos(2\pi f_c t + (\Delta f / f_{FM})\cos(2\pi f_{FM} t))$. a) Pure AM signal. b) Pure FM signal with little but rapid frequency deviations. c) Pure FM signal with slow but important frequency oscillations. d) Combined AM-FM signal. The band limits can be estimated as $f_c \pm BW/2$ based on equation (2). $f_c = 100$ Hz in all four examples, and only the upper band limit ($f_c + BW/2$) is shown in the Power Spectral Density (PSD) estimates.

The VMD assesses the bandwidth of the *modes* as H1-norm, after shifting the Hilbert-complemented, analytic signal down into baseband by complex harmonic mixing. Each *mode* is iteratively updated directly in Fourier domain, as the narrow-band Wiener filter corresponding to the current estimate of the mode's center-frequency being applied to the signal estimation residual of all other modes: then the center frequency is re-estimated as the center-of-gravity of the mode's power spectrum. Before introducing the steps of the VMD algorithm, lets introduce the notions of the Wiener filter, the Hilbert transform and analytic signal. Also, the concept of frequency shifting through harmonic mixing is also reviewed. Such concepts are the very building blocks of the VMD.

2.3 Tools from signal processing

In this subsection, some key VMD concepts are reviewed. First, a Wiener filter case for image denoising is given. Next, the Hilbert transform and its use in the construction of single-sided band analytic signals is given. Finally, multiplications with pure complex harmonics for signal frequency shifting are also given.

2.3.1 Gaussian regularizer and Wiener filtering

Consider the next simple denoising problem. Let $f_0(t)$ be the estimate of the original signal $f(t)$ affected by an additive zero-mean Gaussian noise :

$$f_0(t) = f(t) + \eta(t) \tag{3}$$

Recovering the unknown signal $f(t)$ is a typical ill-posed inverse problem. If the original signal is known to vary smoothly, one would use the following Tikhonov regularized minimization problem in order to estimate a noise free signal [13]:

$$\underbrace{\min}_{f} \left\{ \left\| f(t) - f_o(t) \right\|_2^2 + \alpha \left\| \partial_t f(t) \right\|_2^2 \right\} \tag{4}$$

This is a standard, Gaussian regularized minimum mean squares, i.e., *L2-H1* problem, of which the Euler-Lagrange (EL) equations are easily obtained as:

$$f(t) - f_0(t) = \alpha \partial_t^{\,2} f(t) \tag{5}$$

These EL equations are typically solved in Fourier domain:

$$\hat{f}(\omega) = \frac{\hat{f}_0}{1 + \alpha\omega^2} \tag{6}$$

where $\hat{f}(\omega)$, is the Fourier transform of the signal $f(t)$. Clearly, the recovered signal $f(t)$ is a low pass narrow-band selection of the input signal $f_0(t)$ around $\omega = 0$. This solution corresponds to a convolution with a Wiener filter, where α represents the variance of the white noise, and the signal has a lowpass $1/\omega^2$ power spectrum prior [14]-[15].

2.3.2 Hilbert transform and analytic signal

The 1-D Hilbert transform [16] is the linear, shift-invariant operator H that maps all 1-D cosine functions into their corresponding sine functions. It is an all-pass filter that is characterized by the transfer function $\hat{h}(\omega) = -j\,\mathrm{sgn}(\omega) = -j\omega / |\omega|$. Thus, the Hilbert transform is a multiplier operator in the spectral domain. Its impulse response is $h(t) = 1/(\pi t)$. Because $h(t)$ is not integrable the integrals defining the convolution do not converge. Thus, the Hilbert transform $Hf(t)$ of a signal $f(t)$ is therefore obtained as the Cauchy principal value (p.v.) , given by:

$$Hf(t) = \frac{1}{\pi}\,\mathrm{p.v.}\int_{\mathbb{R}} \frac{f(v)}{t-v}\,dv \tag{7}$$

The inverse Hilbert transform is given by its negative, $H^{-1} = -H$, thus:

$$H^2 f(t) = -f(t) \tag{8}$$

The most prominent use of the Hilbert transform is in the construction of an analytic signal from a purely real signal. Let $f(t)$ be a purely real signal. The complex analytic signal is now defined as:

$$f_A(t) = f(t) + jHf(t) = A(t)e^{j\phi(t)} \tag{9}$$

This analytic signal has the following important properties. The complex exponential term $e^{j\phi(t)}$ is a phasor describing the rotation of the complex signal in time, $\phi(t)$ being the phase, while the amplitude is governed by the real envelope $A(t)$. This representation is particularly useful in the analysis of time-varying amplitude and instantaneous frequency, defined as $\omega(t) = d\phi(t)/dt$. The second property is the unilateral spectrum of the analytic signal, that consists only of non-negative frequencies, hence its use in single-sideband modulation. The original signal is easily retrieved as the real part of $f_A(t)$.

2.3.3 Frequency mixing and heterodyne demodulation

The last concept that must be recalled before introducing the proposed VMD, is the concept of frequency mixing. Mixing is the process of combining two signals non-linearly, thus introducing cross-frequency terms in the output. The simplest mixer is multiplication. Multiplying two real signals with frequencies f_1 and f_2, respectively, creates mixed frequencies in the output at $f_1 - f_2$ and $f_1 + f_2$, which is easily illustrated by the next identity:

$$2\cos(2\pi f_1 t)\cos(2\pi f_2 t) = \cos(2\pi(f_1 + f_2)t) + \cos(2\pi(f_1 - f_2)t) \tag{10}$$

Typical applications are the heterodyne downmixing of the modulated high-frequency carrier signal with a local (heterodyne) oscillator in a radio receiver. In such devices, the selection of either of the two output terms is achieved by filtering. However, in this case, instead of filtering the output, two analytic signals are mixed:

$$e^{j2\pi f_1 t}e^{2\pi f_2 t} = e^{j2\pi(f_1+f_2)t} \tag{11}$$

i.e., the mixed signal is automatically "mono-tone" (constituted of a single frequency only). In the Fourier domain, this is known by the next transforming pair:

$$f_A(t)e^{-j\omega_0 t} \leftrightarrow \hat{f}_A(\omega) * \delta(\omega + \omega_0) = \hat{f}_A(\omega + \omega_0) \tag{12}$$

where δ is the Dirac distribution and $*$ denotes convolution. Thus, multiplying an analytic signal with a pure exponential results in simple frequency shifting.

2.4 The Variational Mode Decomposition (VMD) principle

The VMD method is essentially based on the three concepts discussed in the previous section. The VMD decomposes any input signal into a discrete number of sub-signals (IMFs or simply *modes*), that have sparsity properties while reproducing the input. The sparsity prior of each mode is chosen to be its bandwidth in spectral domain. Each mode k to be mostly compact around a center pulsation ω_k , which is to be determined along with the decomposition. To assess the bandwidth of a mode, in [12] the following scheme is proposed:

1. For each mode u_k, compute its analytic signal via the Hilbert transform in order to obtain a unilateral frequency spectrum.

2. For each mode, shift the mode's frequency spectrum to *baseband*, by mixing with an exponential tuned to the respective estimated center frequency.

3. The bandwidth is now estimated through the H^1 Gaussian smoothness of the demodulated signal, i.e., the squared L^2 -norm of the gradient. The resulting constrained variational problem is the following:

$$\underbrace{\min}_{u_k,\omega_k}\left\{\sum_k \left\|\partial_t\left[\left(\delta(t)+\frac{j}{\pi t}\right)*u_k(t)\right]e^{-j\omega_k t}\right\|_2^2\right\} \tag{13}$$

$$s.t.\sum_k u_k = f$$

The reconstruction constraint can be addressed in many different ways. But, in [12] a quadratic penalty term and Lagrangian multipliers were used in order to render the problem in equation (13) unconstrained. Therefore, the next augmented Lagrangian L was proposed:

$$L(u_k,\omega_k,\lambda)=\alpha\sum_k \left\|\partial_t\left[\left(\delta(t)+\frac{j}{\pi t}\right)*u_k(t)\right]e^{-j\omega_k t}\right\|_2^2+\left\|f-\sum u_k\right\|_2^2+\left\langle\lambda,\, f-\sum u_k\right\rangle \tag{14}$$

Where α is a parameter balancing variational minimization term and constrain term. λ is the Lagrange multiplier. Minimization of (14) can be solved with an ADMM (Alternating Direction Method of Multipliers) method. The initial value of ω_k can be set uniformly or randomly. The ADMM method is given by the next steps:

Algorithm 1 ADMM optimization concept for VMD

Input: Initialize u_k^1, ω_k^1 , λ^1, $u \leftarrow 0$

1. **repeat**
2. n= n + 1
3. **for** $k = 1:K$ **do**
4. Update u_k:

$$u_k^{n+1} = \arg\min_{u_k} \left(L\left(\{u_{i<k}^{n+1}\}, \{u_{i\geq k}^{n}\}, \{\omega_i^n\}, \lambda^n\right)\right) \tag{15}$$

5. **end for**
6. **for** $k = 1:K$ **do**
7. Update ω_k :

$$\omega_k^{n+1} = \arg\min_{\omega_k} \left(\left\{u_i^{n+1}\right\}, \left\{\omega_{i<k}^{n+1}\right\}, \left\{\omega_{i\geq k}^{n}\right\}, \lambda^n \right) \tag{16}$$

8. **end for**
9. Dual ascent :

$$\lambda^{n+1} = \lambda^n + \tau\left(f - \sum_k u_k^{n+1} \right) \tag{17}$$

10. **Until** convergence : $\sum_k \left\| u_k^{n+1} - u_k^n \right\|_2^2 \Big/ \left\| u_k^n \right\|_2^2 < \varepsilon$

Output : Decomposed IMFs or *modes*.

Where equation (15) is first written as:

$$u_k^{n+1} = \arg\min_{u_k \in X} \alpha \left\| \partial_x \left[u_k(x) e^{-j\omega_k x} \right] \right\|_2^2 + \left\| f(x) - \sum_i u_i(x) + \frac{\lambda(x)}{2} \right\|_2^2 \tag{18}$$

Equation (18) can be solved in the Fourier domain and there exists an explicit solution:

$$u_k^{n+1}(\omega) = \frac{\hat{f}(\omega) - \sum_{i\neq k} \hat{u}_i(\omega) + \frac{\hat{\lambda}(\omega)}{2}}{1 + \frac{\alpha}{2}\left(\omega - \omega_2\right)^2} \tag{19}$$

Minimization (16) can be written as:

$$\omega_k^{n+1} = \arg\min_{\omega_k} \left\| \partial_x \left[u_k(x) e^{-j\omega_k x} \right] \right\|_2^2 \tag{20}$$

And also solved in the Fourier domain as:

$$\omega_k^{n+1} = \frac{\int_{-\infty}^{\infty} \omega \left\| \hat{u}(\omega) \right\|^2 d\omega}{\int_{-\infty}^{\infty} \left\| \hat{u}_k(\omega) \right\|^2 d\omega} \tag{21}$$

In practice, the VMD scheme outperforms the EMD [12] with regards to tone detection, tone separation, and noise robustness. However, the most important limitation of the VMD model lies with its boundary effects and sudden signal onset in general. Another inconvenient is the required explicit selection of the number of active *modes* in the decomposition.

3. Results: Methodologies performances and discussion

Before introducing the Core barrel monitoring methodology based on VMD (CBM-VMD). The VMD algorithm is first tested with an artificial signal (the sum of two harmonics, whose frequencies dwell very close to each other), with the goal of highlighting the strengths of the VMD for tone separation over those of the classic Empirical mode decomposition (EMD) method for this task.

3.1 Assessment of the VMD for harmonic separation

As a first example, the next synthetic signal is used:

$$f(t) = \cos(2\pi f_1 t) + \cos(2\pi f_2 t) + \eta(t) \tag{22}$$

The signal is the sum of two harmonics of $f_1 = 6.8$ Hz and $f_2 = 7.9$ (the frequencies f_1 and f_2 lie very close to each other) Hz plus a zero mean additive white Gaussian noise $\eta(t)$ of standard deviation $\sigma = 0.1$ (to attain a signal to noise ratio (SNR) of 20 dBs) . The time series consists of a total of 640 points (the sampling frequency is $F_s = 128$ Hz).This composite signal is shown in Figure 2 and its Power Spectral Density is shown in figure 3. This signal is decomposed into $K = 3$ *modes* via the VMD for the next parameters : $\alpha = 2000$ the ω_k are initialized uniformly, the tolerance of the VMD method ε (step 10 of algorithm 1) is

fixed at $\varepsilon = 10^{-7}$. The VMD of this signal is shown in Figure 4, in which the 3 extracted modes are shown, the first IMF 1 is related to the recovered harmonic of 6.8 Hz, the second one (IMF 2) is the recovered harmonic of 7.9 Hz and the last *mode* (IMF 3) is related to the additive white Gaussian noise $\eta(t)$. From *visual* inspection, the recovered harmonics where properly extracted from the signal $f(t)$, except near the boundaries, where the VMD had difficulties to recover the harmonics of interest, see Figures 5 and 6.

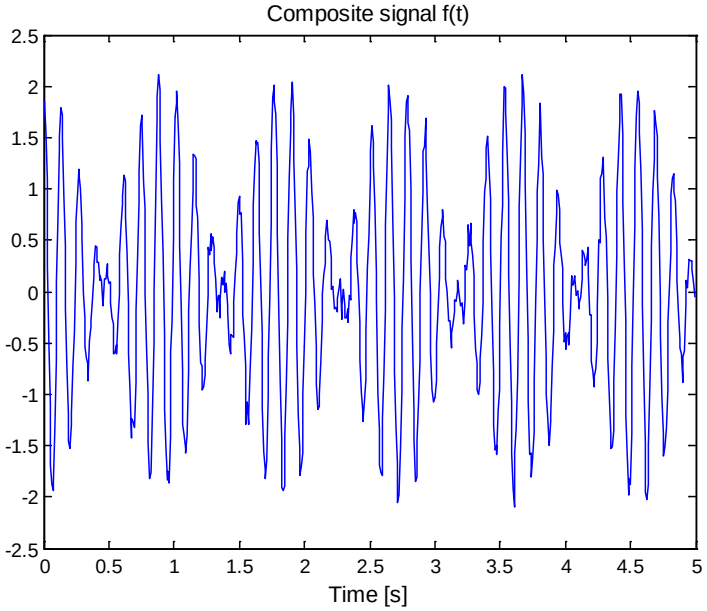

Figure 2. Original synthetic composite signal $f(t) = \cos(2\pi f_1 t) + \cos(2\pi f_2 t) + \eta(t)$.

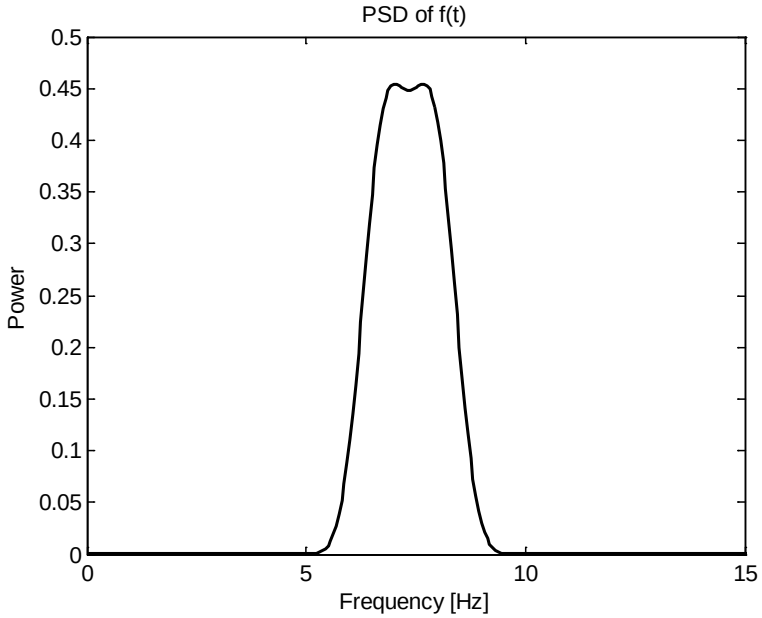

Figure 3. PSD estimate of the signal $f(t)$ shown in Figure 2.

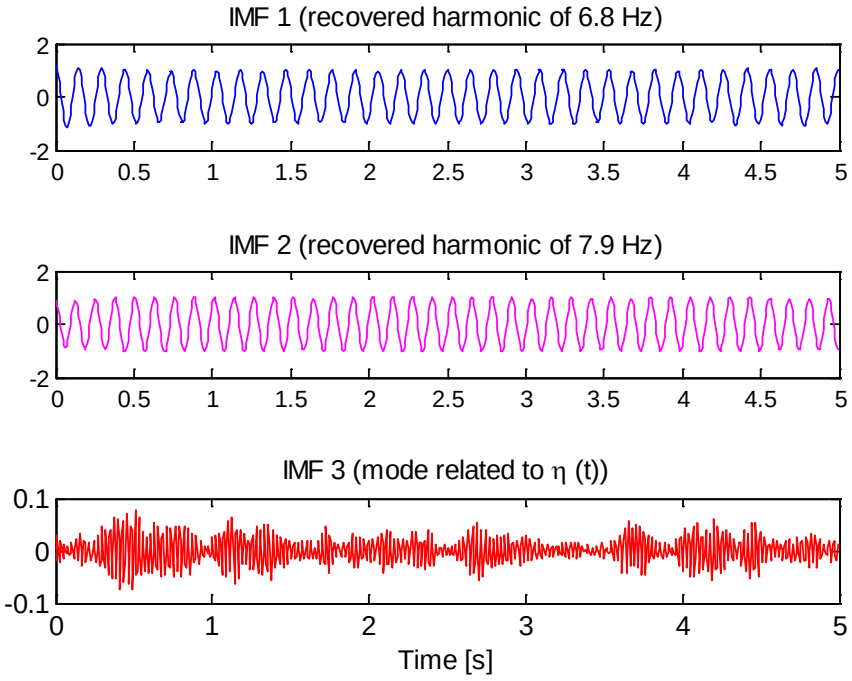

Figure 4. VMD decomposition of the composite signal $f(t)$.

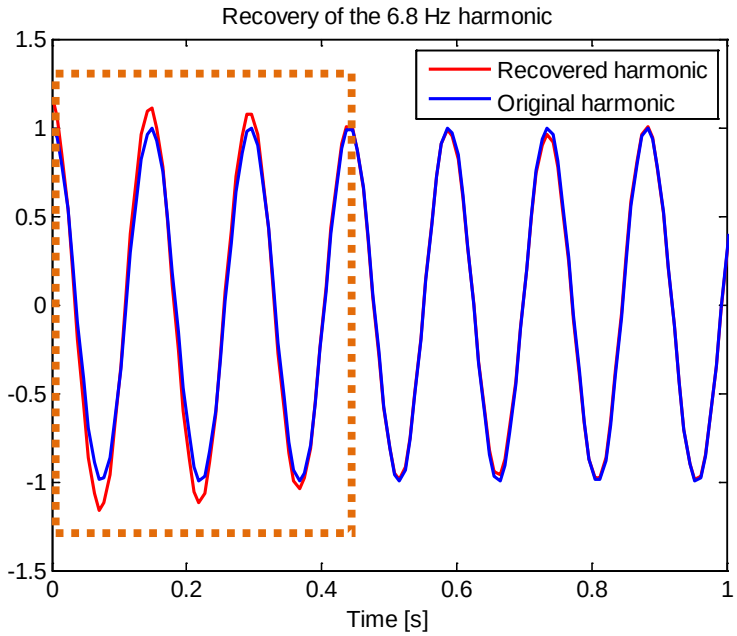

Figure 5. Recovered harmonic of 6.8 Hz (IMF 1). The dotted orange box highlights the time interval, where the VMD has slight difficulties to fully recover the harmonic of interest.

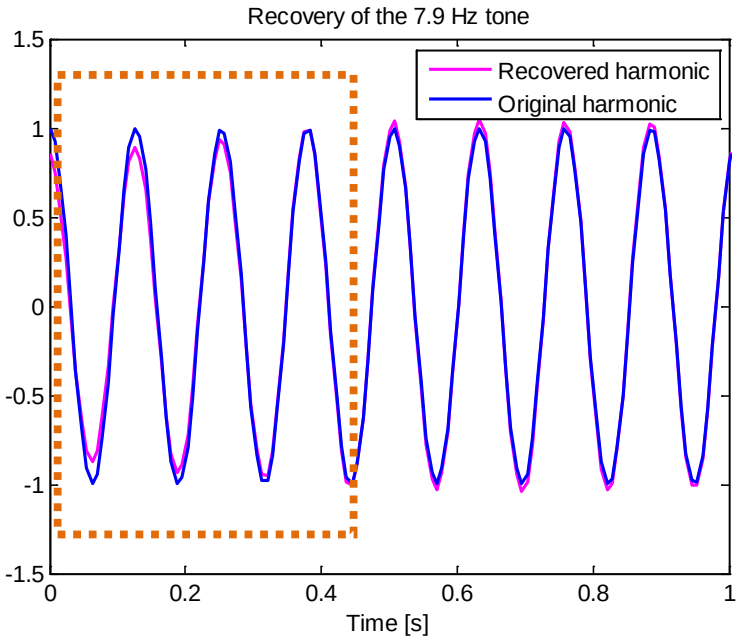

Figure 6. Recovered harmonic of 7.9 Hz (IMF 2). The dotted orange box highlights the time interval, where the VMD has slight difficulties to fully recover the harmonic of interest.

Figure 7 shows the PSD estimate of the 3 extracted intrinsic mode functions IMFs via the VMD model to highlight in the Fourier domain the accuracy of the decomposition to recover the two harmonics of interest. The mean square error (MSE) between the original harmonics and their respective IMFs (reconstruction error) is given below, in Table 1. The MSE errors are *small* (smaller than $<1\%$) , an indication of the potential of the variational mode decomposition (VMD) for separating composite signals that have frequencies lying very close to each other.

VMD - Intrinsic Mode Functions (IMFs) of interest related to the harmonics of interest.	MSE between the original harmonic $\cos(2\pi f_1 t)$ of 6.8 Hz and the extracted IMF 1.	MSE between the original harmonic $\cos(2\pi f_2 t)$ of 7.9 Hz and the extracted IMF 2.
IMF 1	0.1742 %	n/a
IMF 2	n/a	0.1330 %

Table 1. Mean squared error (MSE) comparison between the original harmonics and their corresponding extracted IMFs via the VMD model.

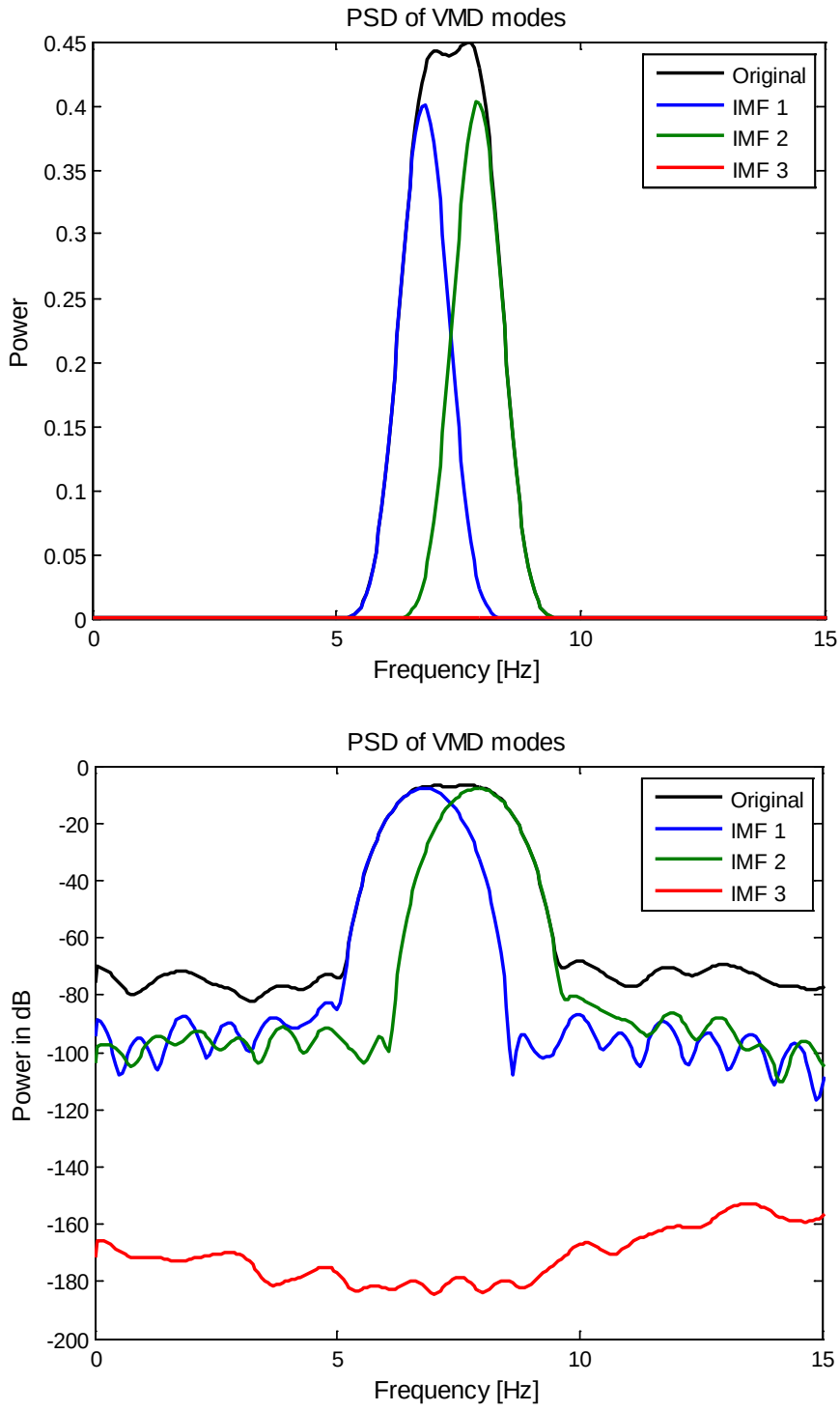

Figure 7. PSD of the VMD - IMFs of the extracted modes of the composite signal given in equation (22) .

Now, the same signal given in equation (22) and depicted in Figure 2 is decomposed via the classic EMD [1]. Figure 8 shows its EMD decomposition into IMFs. Only the first 3 IMFs are shown from a total of 7 IMFs obtained adaptatively (in a data driven way). Nonetheless, the popular EMD method failed to extract the two harmonics of interest (one of 6.8 Hz and the other of 7.9 Hz) that lie very close to each other and the IMFs do not resemble harmonics signals. Figure 9 shows the PSD estimate of the three IMFs shown in Figure 8, most of the spectral content of the signal $f(t)$ is kept in IMF 2, the PSD of IMF 2 shows that the EMD separation wasn't accurate. Thus, another method must be used to separate harmonics that lie close to each other, and the method that thus far can accomplish that, is the VMD model. Thus, the VMD is the method of choice to analyze the Core Barrel motion signals of PWR facilities for its unparalleled frequency resolution.

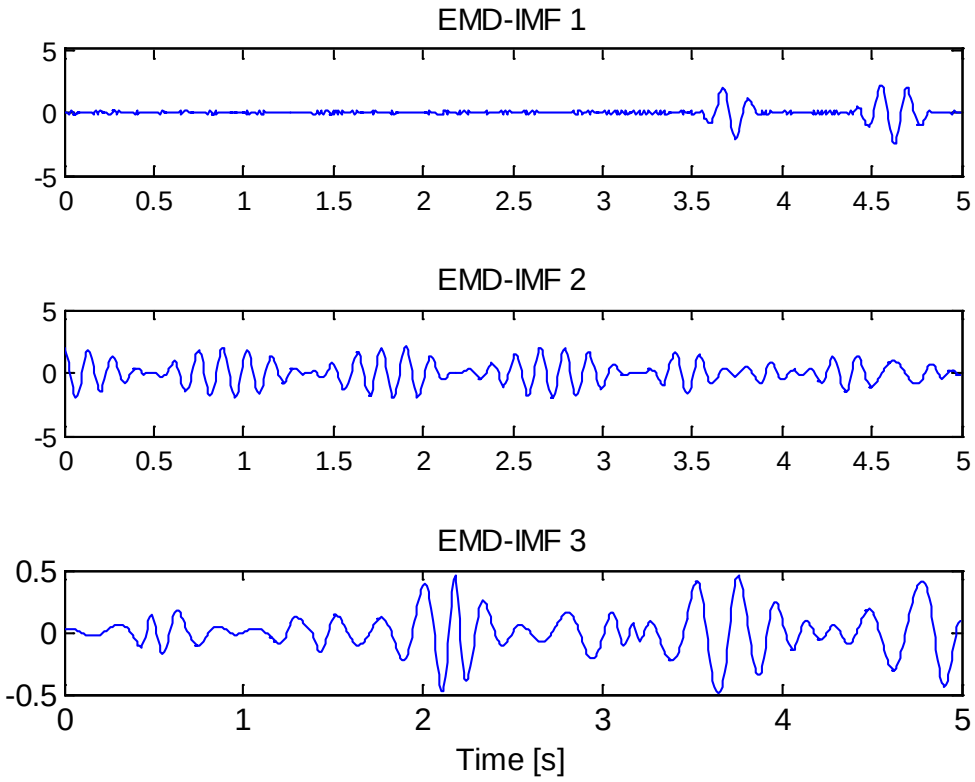

Figure 8. EMD decomposition of the signal $f(t)$ given in equation (22) . Only 3 IMFs are shown out of a total of 8 IMFs, all of them were extracted in a data driven way (in the EMD method, the user has no control of the amount of IMFs that will be extracted). However, the EMD decomposition failed to recover the two harmonics of interest. IMF 2 resembles the original signal $f(t)$. An indication of an unsuccesful separation of data.

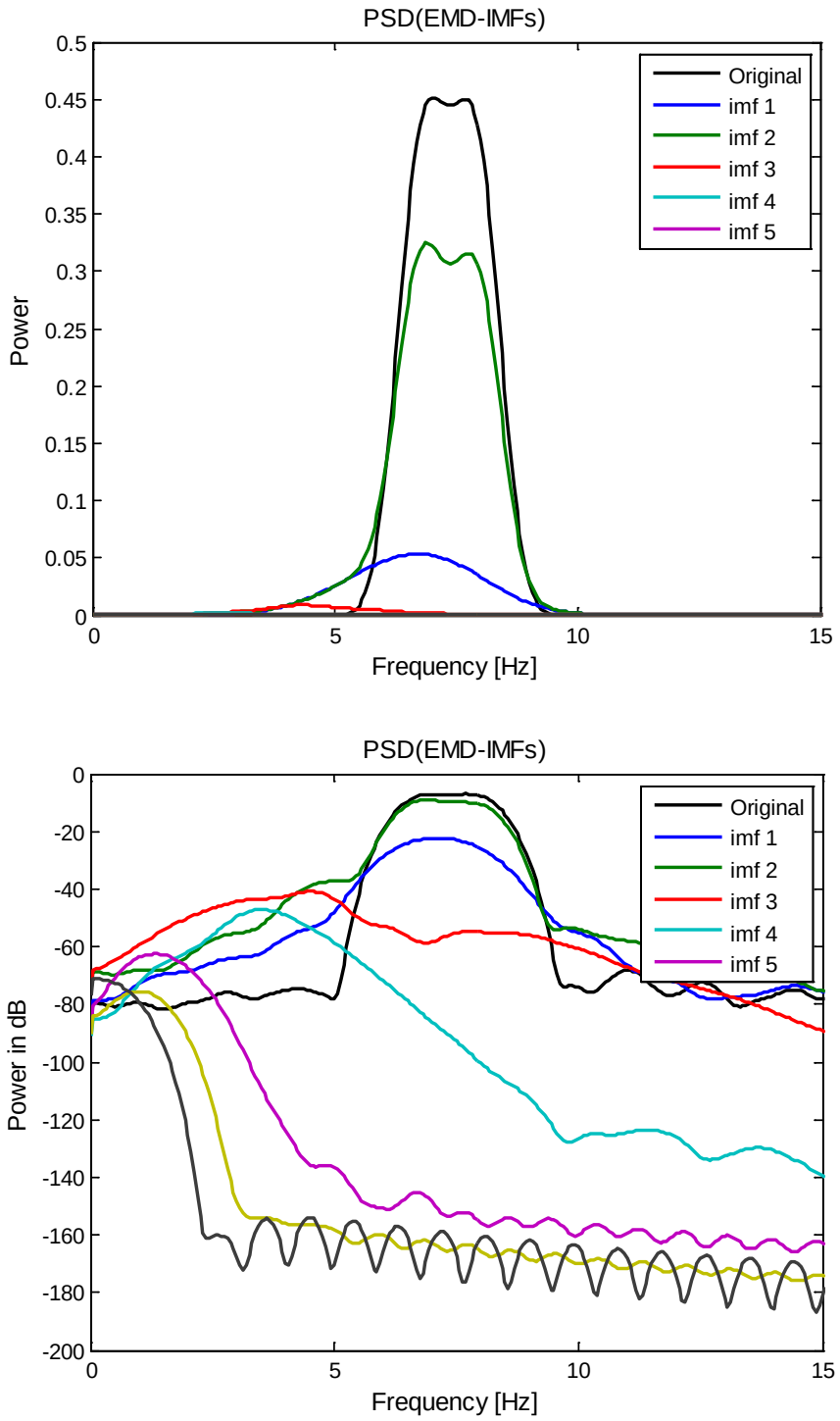

Figure 9. PSD of the EMD - IMFs of the extracted modes of the composite signal given in equation (22). Only 5 IMFs are shown out of a total of 7 IMFs plus a residue signal $r(t)$.

3.2 Core-Barrel Motion monitoring methodology based on the VMD model (CBM - VMD)

The proposed methodology for Core-Barrel monitoring analysis based on the Variational Mode Decomposition (VMD) is tested with Ringhals CMB measurements of the years 2016 and 2017 from *upper* detectors N41U-N44U and from *lower* detectors N41L-N44L. The CBM-VMD methodology is given by the next steps:

Methodology 1 : CMB -VMD

1. The considered signal ($\mu_x(t)$ or $\mu_y(t)$) obtained from, for instance, from the Upper detectors (or Lower detectors) is segmented in windows of 15 minutes of duration.

2. The studied segment is decomposed via the VMD into $K=15$ *modes* for the next parameters : $\alpha=2000$, the ω_k are initialized uniformly and the tolerance ε (step 10 of algorithm 1) remains fixed as before at $\varepsilon=10^{-7}$

3. The PSD is estimated for each extracted *mode* via the the Welch method [17] . A method for the estimation of power spectra based on time averages over short modified periodograms. Later, a peak detection method is used to locate the local maxima of the PSD of all of the extracted K *modes* (all of the modes are expressed in dB for this step) with the goal of finding the central frequency of each individual mode. This frequency matches the position of the global maxima of the PSD estimates.

4. When tracking these frequencies, it is possible to get the two *modes* associated to the **beam mode** (one *mode* located around 6.8 Hz and the second one, located around 7.9 Hz and labeled from now on as MODE 1 and MODE 2, respectively). In this way, only the *modes* (IMFs) linked to the physical processes of interest are selected for further processing whereas the remaining modes are discarded.

5. The central frequencies (f_1 and f_2) and the Amplitudes (A_1 and A_2) of the two chosen IMFs are stored. The amplitude estimate A_1 (or A_2) is calculated with the next formula (to make this estimate less arbitrary):

$$A_1=\frac{1}{2J+1}\left(\sum_{i=1}^{J}\rho(l_\tau-i)+\tau+\sum_{i=1}^{J}\rho(l_\tau+i)\right) \tag{23}$$

Where $\rho(l)$ is the function that denotes the detected peaks of the PSD estimates of the chosen *modes* (linked to the **beam mode**) and the index l denotes their location along time. τ is the value of the global maxima (the value of the highest peak), l_τ, is its location and J is a number of peaks around τ that are taken to make the estimate of A_1 (or of A_2) less arbitrary (an average operation).

6. Finally, these stored values are averaged along time (and the variance of these estimates is also computed) for all of the studied segments of 15 minutes each. The output variables of this Core-Barrel Motion analysis methodology are:

   i. $\hat{f}_1$: Averaged center frequency of MODE 1 along time.

   ii. $\hat{A}_1$: Average amplitude (The estimated global maxima) of MODE 1 along time.

   iii. $\hat{f}_2$: Averaged center frequency of MODE 2 along time.

   iv. $\hat{A}_1$: Averaged amplitude (The estimated global maxima) of MODE 2 along time.

3.3 CBM-VMD monitoring test on an artificial Neutronic noise signal

The CBM-VMD monitoring methodology described above is first tested with a synthetic noise signal that was generated by filtering Gaussian Noise in specific spectral regions to emulate the dynamics of a real neutronic noise signal. A total of three different butterworth [18] filters were used:

1. A low pass filter (LPF) of order 10 of passband in the interval 0 to 2.5 Hz, a stop band corner frequency of 5 Hz, with no more than 3dB of ripple and at least 60 dB of attenuation in the stop band.

2. A pass band filter (BPF 1) of order 6 of passband in the interval 7.5 to 8.5 Hz, with stopbands of 1.5 Hz wide on both sides of the passband, with at most 3 dB of passband ripple and at least 60 dB of attenuation in the stopbands.

3. Another pass band filter (BPF 2) of order 7 of passband in the interval 19 to 21 Hz, with stopbands of 2 Hz wide on both sides of the passband, with at most 3 dB of passband ripple and at least 60 dB of attenuation in the stopbands.

A single realization of white Gaussian noise is filtered with the Butterworth filters decribed above as follows:

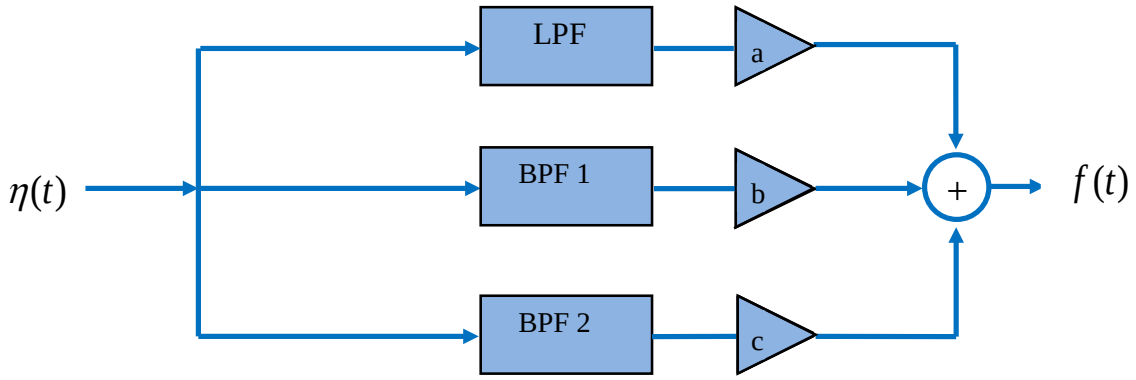

Figure 10. Block diagram used to emulate the Fourier spectral dynamics of neutronic noise from the starting Gaussian noise signal $\eta(t)$. The coefficients a, b and c are arbitrary constants that are used to control the gain of the filters, their values are a=1, b=1/16 and c=1/128.

The artificial neutronic noise signal is shown in Figure 11. The samling rate used is $F_s = 64$ Hz. The Welch Power Spectral Density (PSD) estimate of this neutronic noise is shown in Figure 12. This PSD estimate imitates the Fourier dynamics of a real neutronic noise signal. The CBM survey methodolgy discussed in section 3.2 is applied to the signal shown in Figure 11. A total of 15 IMFs were extracted through VMD (with the same parameter values given previously) and only the first 5 of them are shown in Figure 13. Figure 14 shows the Welch PSD estimates of the extracted IMFs, also a zoom in to our region of interest related to the beam mode (which is around 8 Hz) is also provided. It is infered that this 8 Hz peak was separated into two different IMFs that are renamed from now on as MODE 1 (which is the IMF 4) and MODE 2 (which is the IMF 5). MODE 1 is centered around 7 Hz whereas MODE 2 is centered around 8 Hz. Later a peak detection method is used to infer the value of the center frequency f_1 and the amplitude A_1 of the peak (estimated with equation (23) for a neighborhood of J=3 peaks around the global maxima of the lobe). This same procedure is applied to MODE 2. All amplitude estimated values are given in decibels (dB) and are presented in Table 2 along with the estimated central frequencies of boths MODEs.

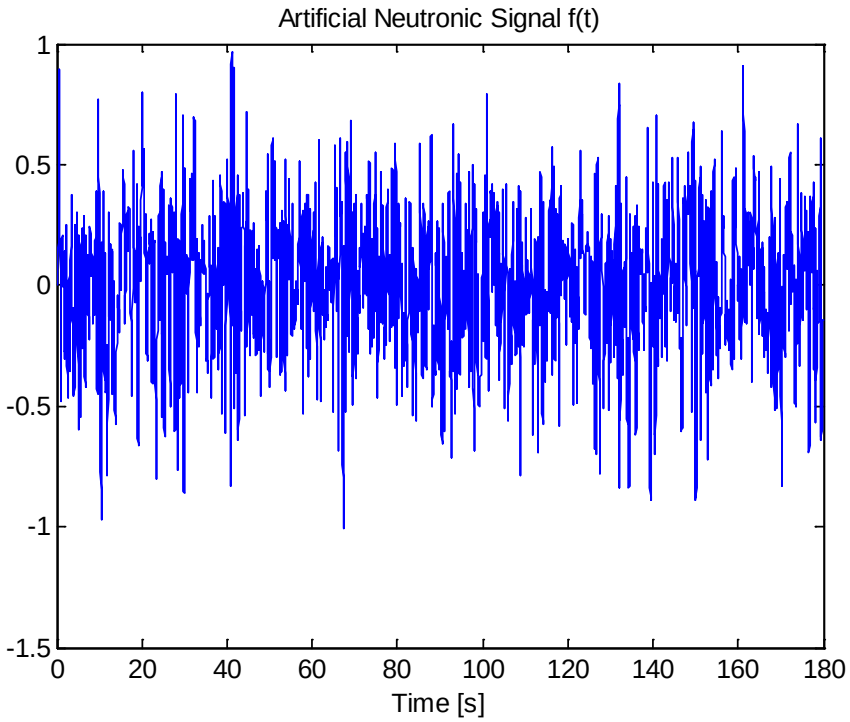

Figure 11. Artificial neutronic noise signal generated with the block diagram of figure 10.

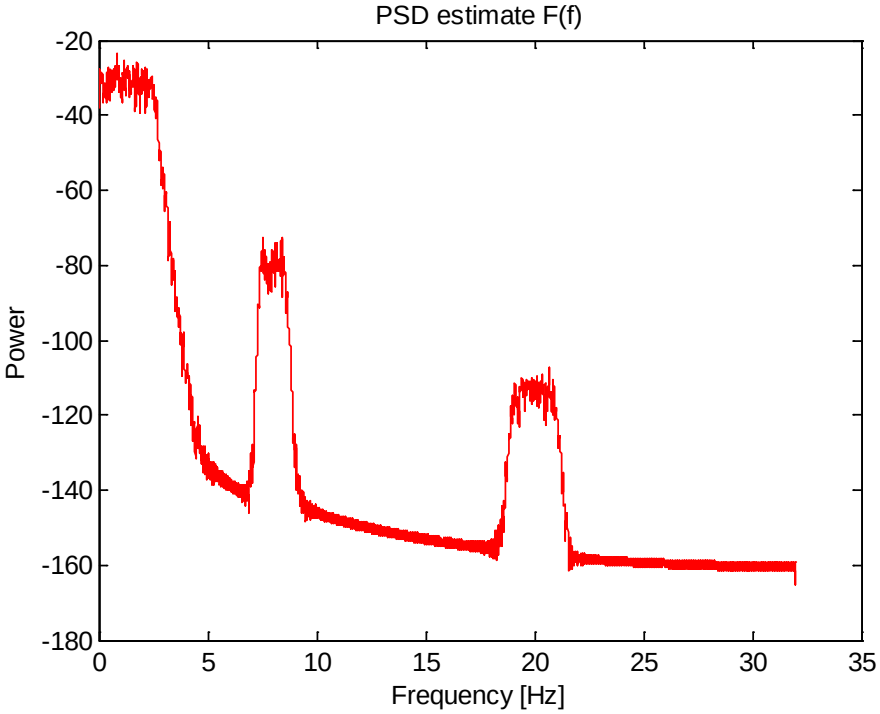

Figure 12. PSD estimate of the synthetic neutronic noise signal shown in Figure 11.

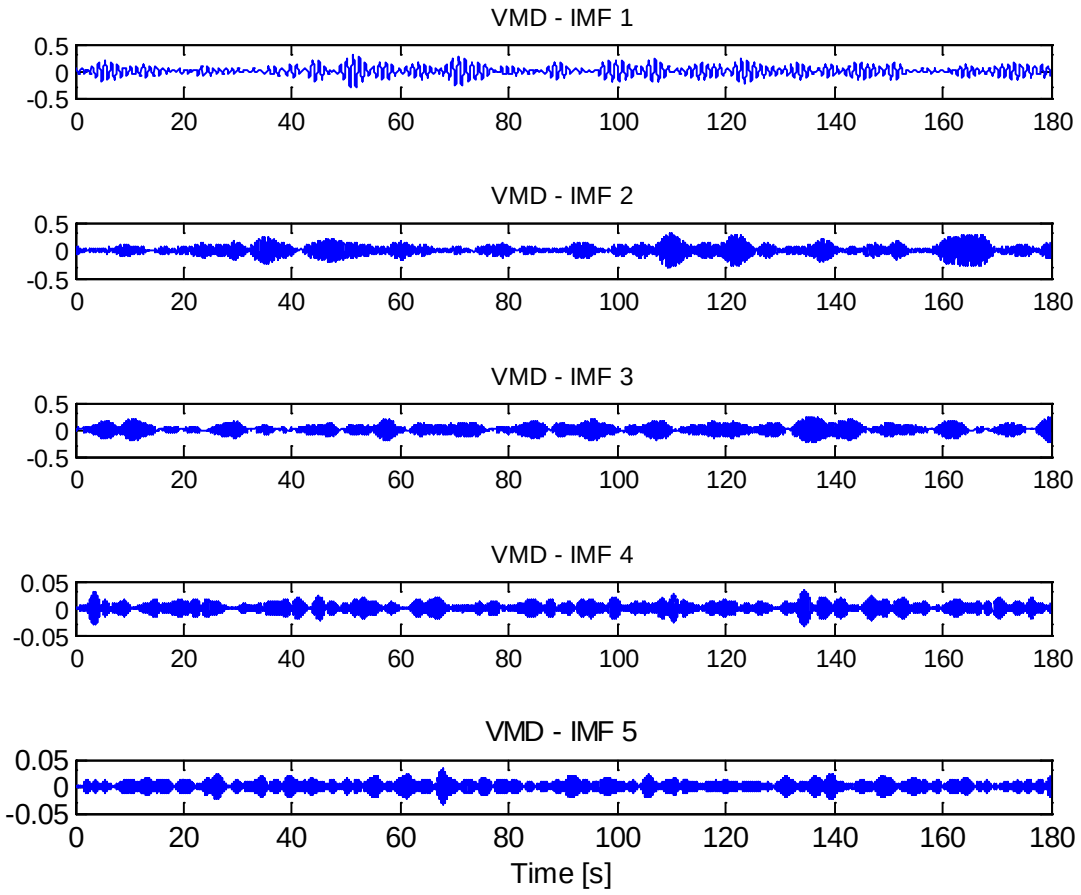

Figure 13. VMD decomposition of the signal shown in Figure 11 into IMFs. Only the first 5 IMFs are shown in this plot from a total of $K=15$. The parameters for the VMD model are $\alpha=2000$, the ω_k of the optimization method are initialized uniformly and the tolerance ε (step 10 of algorithm 1) remains fixed as before at $\varepsilon=10^{-7}$.

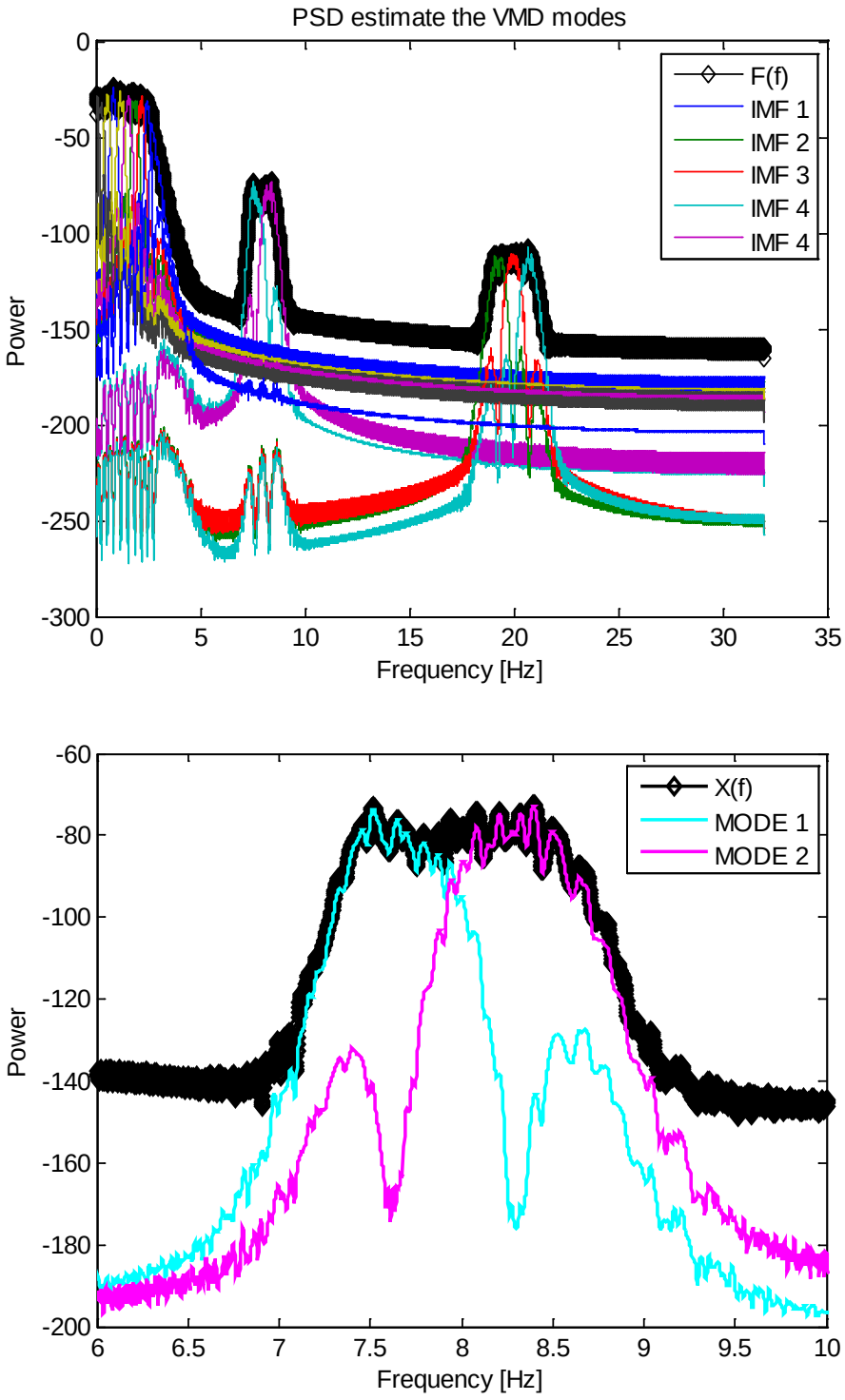

Figure 14. PSD estimate of the extracted IMFs through VMD, the black line is the PSD estimate of the original signal (shown in Figure 12). The remaining IMFs are ignored.

Modes Related to the Beam mode	Central Frequency Hz	Amplitude in dB
MODE 1 (*mode* 4)	$f_1 = 7.5566$	$A_1 = -79.0265$
MODE 2 (*mode* 5)	$f_2 = 8.2754$	$A_2 = -77.9179$

Table 2. Estimated central Frequency and Amplitude of the MODEs (IMFs 4 and 5) related to the beam mode (step 5 of the Methodology 1 described in subsection 3.2).

This methodology was capable of separating the two peaks of interest that lie very close to each other into two IMFs, from these individual IMFs (MODE 1 and MODE 2), it is possible to estimate their Amplitudes and their center frequecies to assess the Core-Barrel motion. However, the most important limitations of the VMD lie with boundary effects, sudden signal onset. Another point critics might have is the required explicit (manual) selection of the number of active *modes* in the decomposition. But, in this analysis, our main concern is to isolate the two peaks around our region of interest related to the beam mode. All other extracted *modes* are discarded.

3.4 CBM-VMD monitoring test on real neutronic signals

3.4.1 General Principles and Background

The signals that are used for analysis stem from four detectors that are placed around the core and are numbered as: detectors N41, N42, N43 and N44. These detectors are placed diagonally opposite to each other, as shown in Figure 15. These two diagonals define the x and y components of the beam-mode vibrations. The neutron noise induced by the beam-mode vibrations is proportional to the dosplacement components, scaled with an (unknown) displacement to-detector current factor μ. The total signals of the four detectors, accounting for all noise components, can be obtained as follows. One assumes that the individual signals of each ex-core detector consist of four components, i.e., uncorrelated background noise $\delta r_i(t)$, a reactivity of point-kinetic components, $\delta P(t)$, beam-mode vibrations of the core barrel $\mu\delta r(t)$ [containing two directional components $x(t)$ and $y(t)$], and shell-mode vibrations of the core barrel $D(t)$. Based on symmetry considerations, the four detectors can be written as:

$$\delta\phi_1(t) = \delta r_1(t) + \delta P(t) + \mu x(t) + D(t) \tag{24}$$

$$\delta\phi_2(t) = \delta r_2(t) + \delta P(t) - \mu x(t) + D(t) \tag{25}$$

$$\delta\phi_3(t) = \delta r_3(t) + \delta P(t) + \mu y(t) - D(t) \tag{26}$$

$$\delta\phi_4(t) = \delta r_4(t) + \delta P(t) - \mu y(t) - D(t) \tag{27}$$

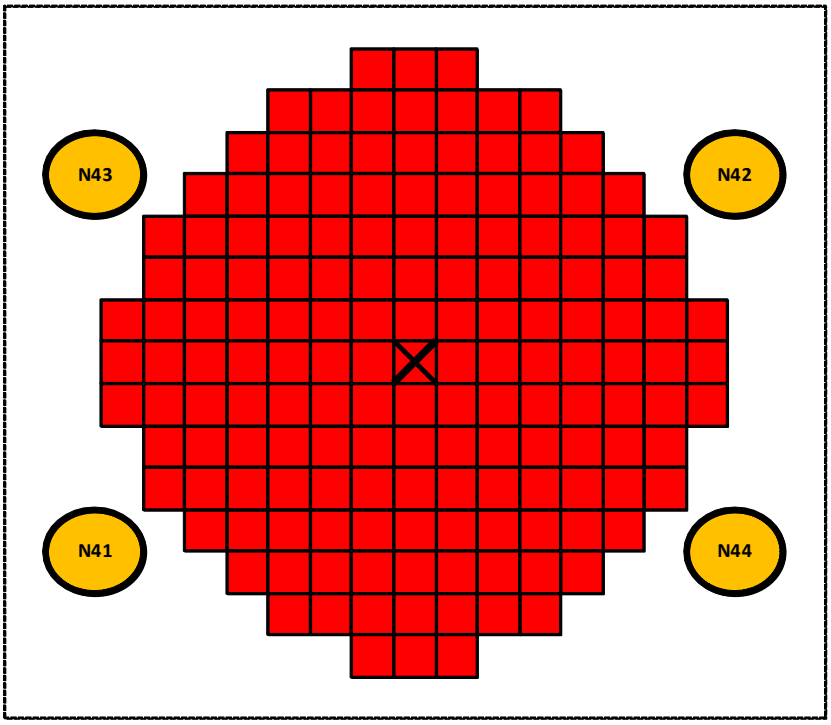

Figure 15. Layout of the ex-core neutron detectors placed around the core.

Where $\delta\phi_i$, $i = 1,...,4$ stands for the neutron noise from detectors N41, N42, N43, and N44, respectively (either Upper or Lower); μ is the (unknown) scaling factor between the neutron noise and the meachanical vibrations; $x(t)$ and $y(t)$ are the components of the beam-mode vibrations, the x-direction being the diagonal between the detectors N41 and N42. The last two terms in each expression correspond to the CBM modes (beam and shell), and their respective signs express the corresponding symmetry of the vibration modes. The uncorrelated background is due to other processes than the CBM and is, hence, statistically independent from it; moreover, it is uncorrelated between the four different detectors. The reactivity term may be induced either by independent processes or by the CBM itself, or a combination of the two. The separation of the beam-mode and the reactivity components is based on different combinations of the detector signals. The enhancement of the beam-mode component goes as follows. Based on equations (24) to equation (27), the four detectors at one axial level are used in the following combination to determine the

beam-mode displacement components:

$$\mu x(t) = \frac{1}{2}\left(\delta\phi_{41} - \delta\phi_{42}\right) \tag{28}$$

and

$$\mu y(t) = \frac{1}{2}\left(\delta\phi_{43} - \delta\phi_{44}\right) \tag{29}$$

This signal combination eliminates the reactivity component, and it is assumed that it diminishes the background noise, which is assumed to be small in anyway compared to the peak (in this case mode is different from our previous definition of *mode* (IMF)).

3.4.2 Analyis of the CBM measurements of the year 2016 through VMD (Upper detectors)

Figure 16 shows the upper beam mode displacement component $\mu x(t)$ between detectors $\delta\phi_{41}$ and $\delta\phi_{42}$ (detectors N41 and N42). A 15 minute segment is shown in this figure, this segment is analyzed through the CBM analysis methodology previously described in subsection 3.2. Figure 17 shows its Welch power spectral density (PSD) estimate, from now on, our goal is to separate this studied 15 minute segment into IMFs, to later isolate the IMFs related to the beam mode information spectral content. This signal is decomposed via the VMD into $K = 15$ different independent *modes*, their PSD estimates are shown in Figure 18, where a zoom is made in the region of 0 Hz to 10 Hz. It is inferred that the information of the 8 Hz peak was *separated* into 2 independent IMFs, located at the 7-th and 8-th (MODE 1 and MODE 2 respectively) level of the VMD decomposition. A peak detection algorithm (a local maxima detector) is used to infer the central frequencies and the amplitudes (the PSDs are expressed in dBs) of their peaks. Figure 20 shows the detected peaks that are used to infer the center frequencies f_1 and f_2 and the amplitudes of the peaks A_1 and A_2. To estimate A_1 (or A_2) equation (23) was used for $J = 5$. Table 3 shows these estimates for the upper studied segment shown in Figure 16. Figure 21 shows the estimated values of the center frequencies and amplitudes (with $J = 5$) along time for each 15 minute segment, a total of 12 segments were analized, the entire time span of the signal is of 3 hours for a sampling frequency $F_s = 62.5$ Hz. Average values for the estimated parameters with their respective standard deviations are shown in Table 4. The extracted modes (in the time domain) are not shown in the plots, becuase the information of interest lies in the Fourier domain.

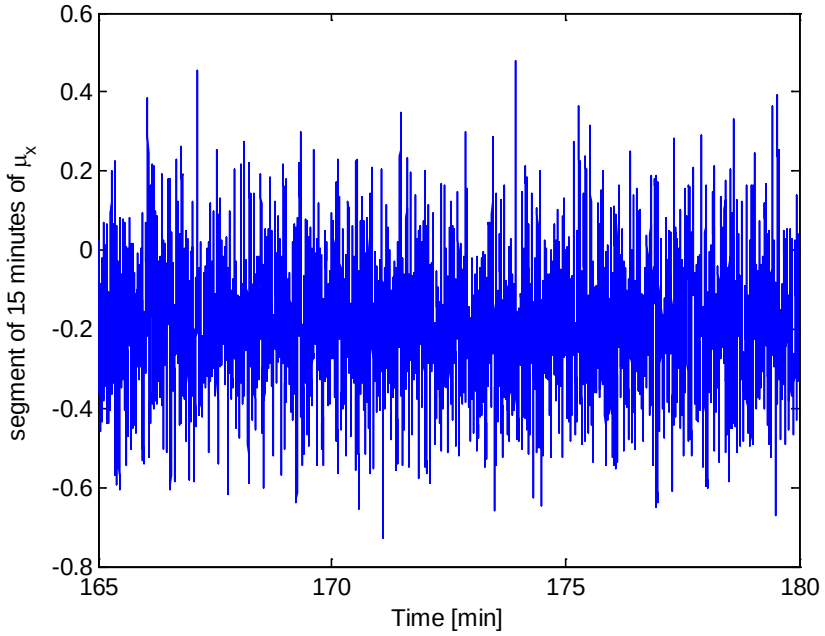

Figure 16. Real studied Upper displacement component $\mu x(t)$.

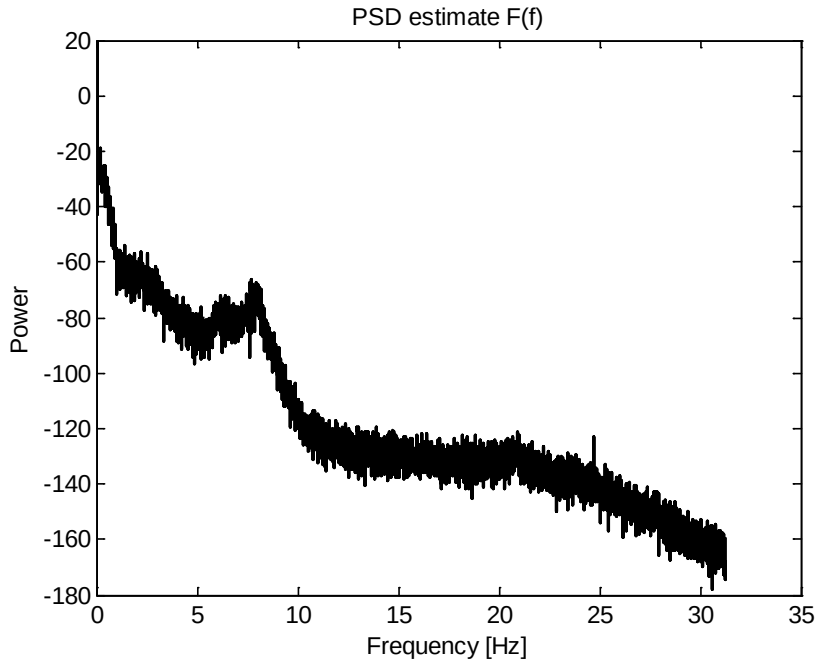

Figure 17. PSD estimate of the signal shown in Figure 16.

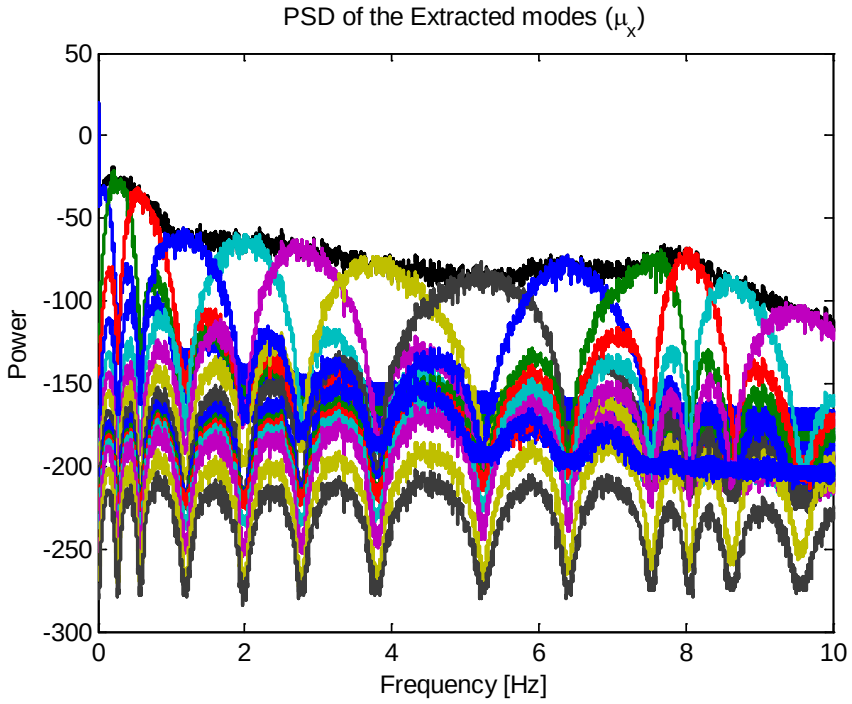

Figure 18. Welch PSD estimates of the IMFs extracted through VMD.

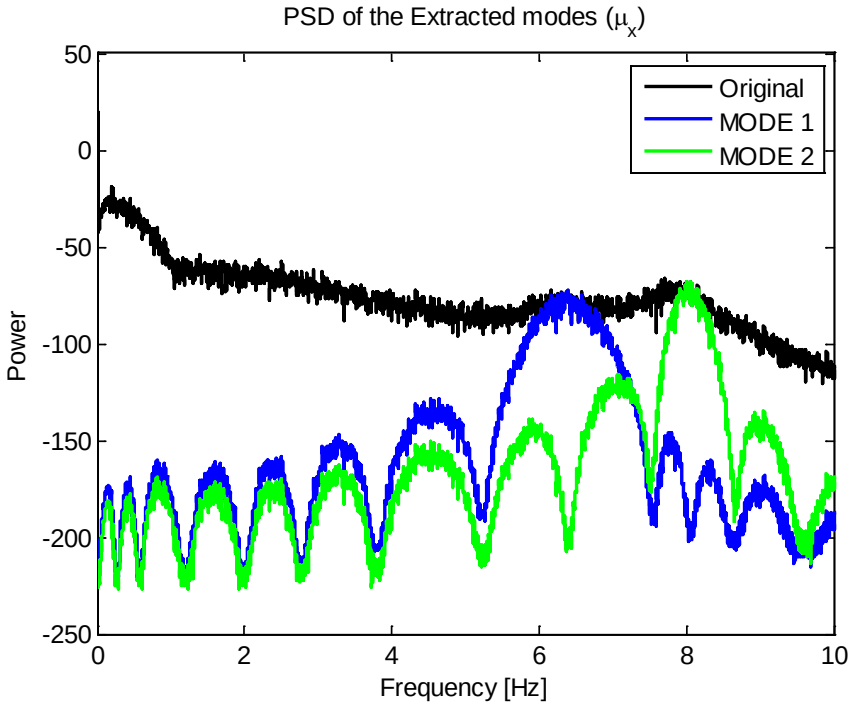

Figure 19. PSD estimates of the IMFs of interest related to the beam mode (MODE 1 and MODE 2).

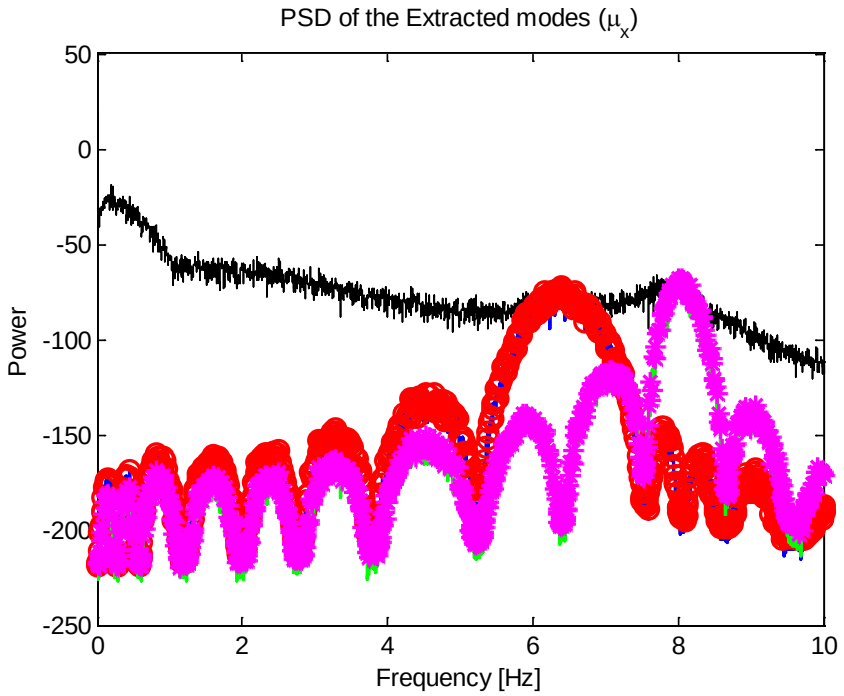

Figure 20. Detected Peaks of MODE 1 and MODE 2 that are used to infer the peak amplitudes (A_1 and A_2) and center frequencies (f_1 and f_2) of the extracted modes.

Modes Related to the Beam mode	Central Frequency Hz	Amplitude in dB
MODE 1 (*mode* 7)	$f_1 = 6.3843$	$A_1 =$ -72.3652
MODE 2 (*mode* 8)	$f_2 = 8.0149$	$A_2 =$ -68.2828

Table 3. Estimated central Frequencies and Amplitudes of the MODEs (IMFs 7 and 8) related to the beam mode (step 5 of the Methodology 1 described in subsection 3.2).

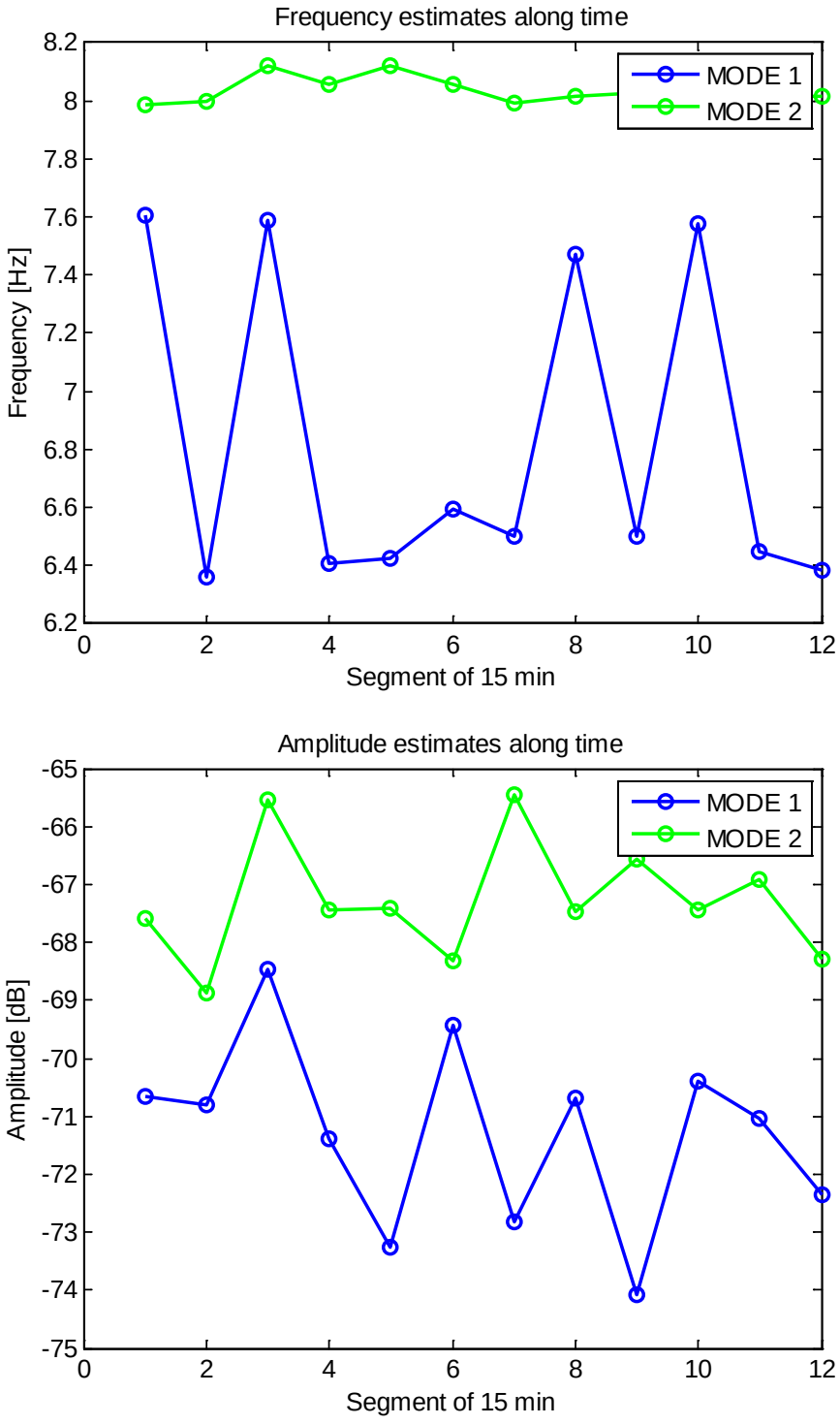

Figure 21. Estimated values of the central frequencies and amplitudes ($\mu x(t)$) for MODE 1 and MODE 2.

Estimates for **MODE 1**	Mean value	Standard deviation
Center Frequency f_1 [Hz]	6.8229	0.5497
Amplitude of the Peak A_1 [dB]	-71.2813	1.6069

Estimates for **MODE 2**	Mean value	Standard deviation
Center Frequency f_2 [Hz]	8.0343	0.0473
Amplitude of the Peak A_2 [dB]	-67.2730	1.0333

Table 4. Average value of the central frequencies and peak Amplitudes of the Upper displacement component $\mu x(t)$ estimated via a CBM-VMD analysis methodology.

Figure 22 shows the beam mode displacement component $\mu y(t)$ between detectors $\delta\phi_{43}$ and $\delta\phi_{44}$ (detectors N43 and N44) . Again, a 15 minutes segment is shown in this Figure. It's power spectral density estimate (PSD) is shown in Figure 23. This neutronic noise signal is separated via VMD into 15 different independent modes, the PSD estimates of this modes are shown in Figure 24 (with a zoom in to our region of interest near the beam mode, the black line is the PSD estimate of $\mu y(t)$ (the targeted signal to be decomposed)). The two *modes* (MODE 1 and MODE 2) closer to the beam mode region of interest are isolated for further processing and the remaining IMFs are ignored. MODE 1 and MODE 2 are shown in Figure 25 and their detected peaks (local maxima) are shown in Figure 26. Table 5 shows the estimated center frequencies and peak amplitudes of the studied segment. Figure 27 shows the estimated values of the center frequencies and amplitudes (with $J = 5$) along time for each 15 minute segment, a total of 12 segments were analized, the entire time span of the signal is of 3. Average values for the estimated parameters with their respective standard deviations are shown in Table 7.

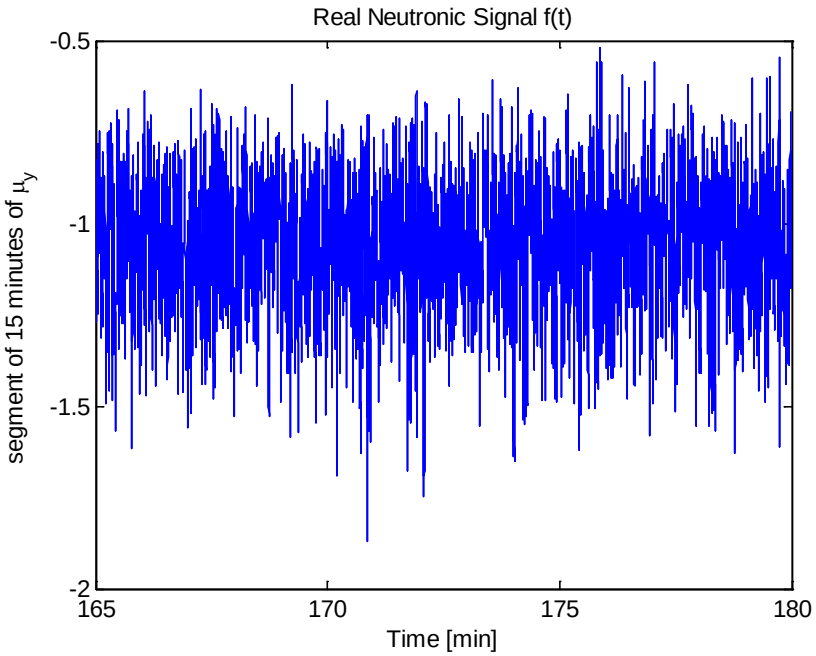

Figure 22. Real studied displacement component $\mu y(t)$.

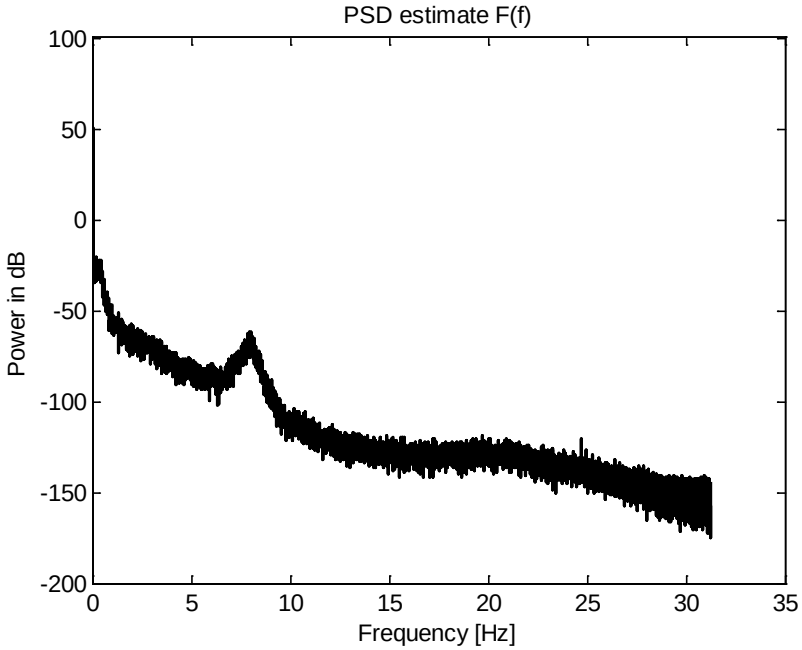

Figure 23. PSD estimate of the signal shown in Figure 22.

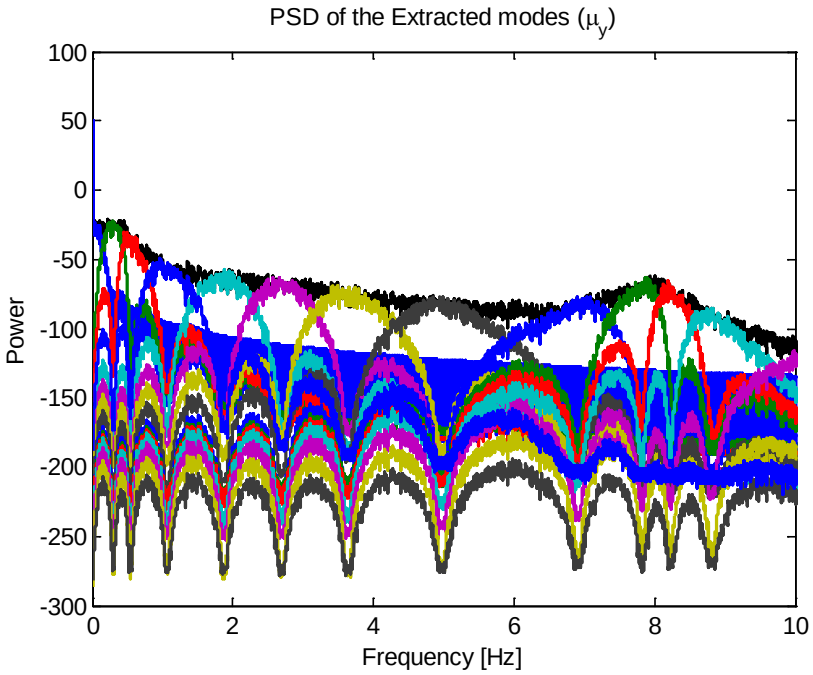

Figure 24. Welch PSD estimate of the IMFs extracted through VMD.

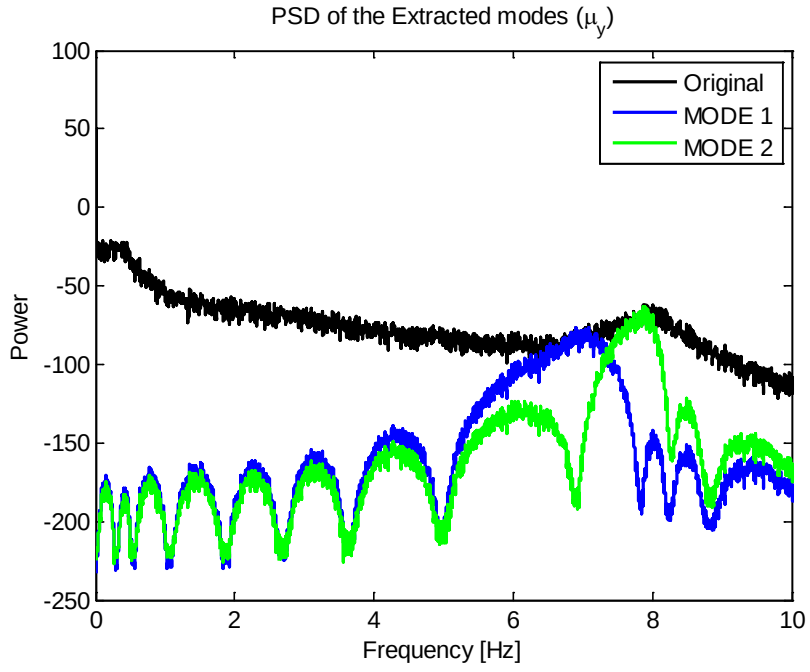

Figure 25. PSD estimates of the IMFs of interest related to the beam mode (MODE 1 and MODE 2).

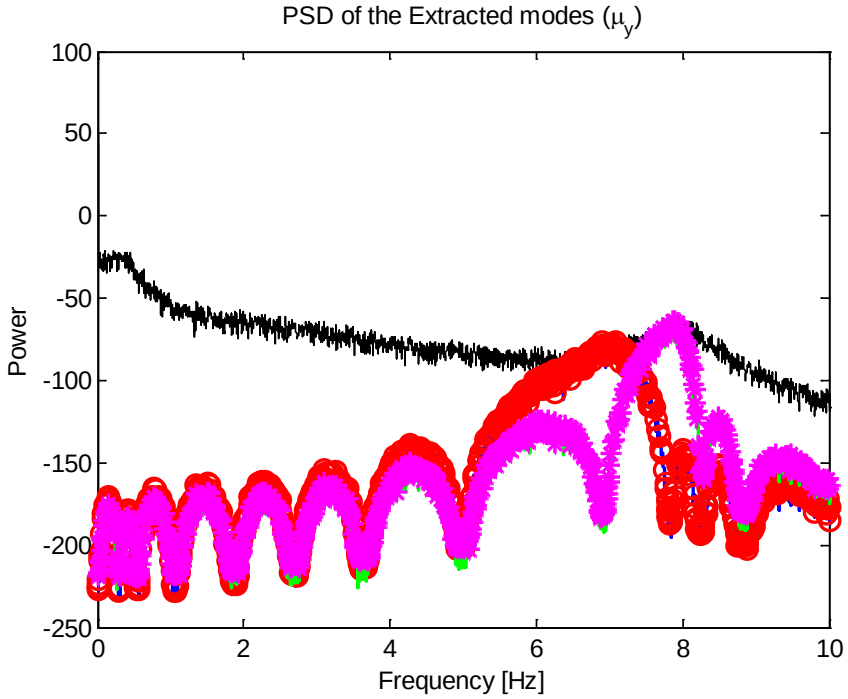

Figure 26. Detected Peaks of MODE 1 and MODE 2 that are used to infer the peak amplitudes (A_1 and A_2) and center frequencies (f_1 and f_2) of the extracted modes.

Modes Related to the Beam mode	Central Frequency Hz	Amplitude in dB
MODE 1 (*mode* 7)	f_1 = 6.9076	A_1 = -76.6799
MODE 2 (*mode* 8)	f_2 = 7.8643	A_2 = -62.9447

Table 5. Estimated central Frequencies and Amplitudes of the MODEs (IMFs 7 and 8) related to the beam mode (step 5 of the Methodology 1 described in subsection 3.2).

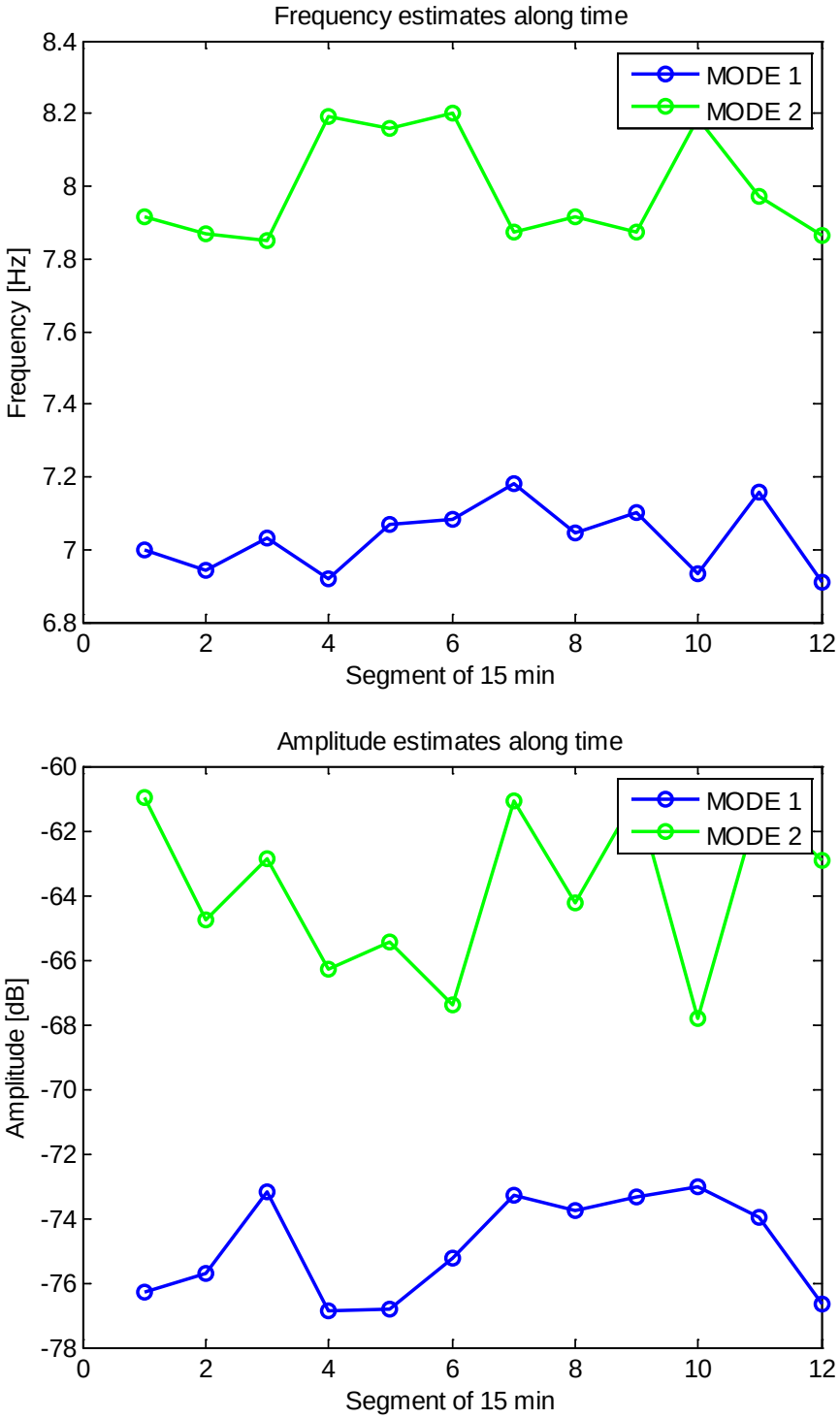

Figure 27. Estimated values of the central frequencies and amplitudes ($\mu y(t)$) for MODE 1 and MODE 2.

Estimates for **MODE 1**	Mean value	Standard deviation
Center Frequency f_1 [Hz]	7.0312	0.0923
Amplitude of the Peak A_1 [dB]	-74.8531	1.5673

Estimates for **MODE 2**	Mean value	Standard deviation
Center Frequency f_2 [Hz]	7.9897	0.1474
Amplitude of the Peak A_2 [dB]	-63.8221	2.5493

Table 6. Average value of the central frequencies and peak Amplitudes of the Upper displacement component $\mu y(t)$ estimated via a CBM-VMD analysis methodology.

For reasons of space, only the analysis of the Upper detectors (the analysis of the Upper displacement components $\mu x(t)$ and $\mu y(t)$) was presented in full detail, the center frequencies and peak amplitudes of all the detectors (Upper and Lower) are shown in Table 7.

Estimates for **MODE 1**	Mean(f_1) Hz	Std(f_1) Hz	Mean(A_1) in dB	Std(A_1) in dB
UPPER				
$\mu x(t) = (N41U - N42U)/2$	6.8229	0.5497	-71.2813	1.6069
$\mu y(t) = (N43U - N44U)/2$	7.0312	0.0923	-74.8531	1.5673
LOWER				
$\mu x(t) = (N41L - N42L)/2$	7.4300	0.0798	-65.4356	1.3552
$\mu y(t) = (N43L - N44L)/2$	7.4728	0.3751	-64.8035	3.1152

Estimates for **MODE 2**	Mean(f_2) Hz	Std(f_2) Hz	Mean(A_2) in dB	Std(A_2) in dB
UPPER				
$\mu x(t) = (N41U - N42U)/2$	8.0343	0.0473	-67.2730	1.0333
$\mu y(t) = (N43U - N44U)/2$	7.9897	0.1474	-63.8221	2.5493
LOWER				
$\mu x(t) = (N41L - N42L)/2$	7.9452	0.0401	-59.9722	1.1980
$\mu y(t) = (N43L - N44L)/2$	8.0481	0.0505	-56.8539	1.5138

Table 7. Average center frequencies f_1 and f_2 (with their respective standard deviations (std)) and average peak amplitudes A_1 and A_2 (with their respective standard deviations (std)) for the 2016 year Core-Barrel Motion measurements.

3.4.3 Analyis of the CBM measurements of the year 2017 through VMD (Upper detectors)

Now, the CBM analysis of the measurements of this year are presented, starting with the analysis of the displacement component $\mu x(t)$ (between detectors N41U and N42U). Figure 28 shows the signal that will be decomposed by VMD into 15 different IMFs. Figure 29 shows its Welch PSD estimate. Figure 30 shows the PSD estimate of the extracted IMFs, Figure 31 shows the PSD of the isolated IMFs of interest (MODE 1 and MODE 2) , Figure 32 shows the detected peaks of the isolated Intrinsic Mode Functions (IMFs) of interest, their peak amplitudes and center frequencies (of all the segments) are shown in Figure 33. Table 8 shows the average output parameters (f_1 and f_2 for the center frequencies of the studied MODEs and amplitude peaks A_1 and A_2) along time for all of the 12 studied segments. And Table 9 shows the average estimated values for the 2017 CBM detector measurements.

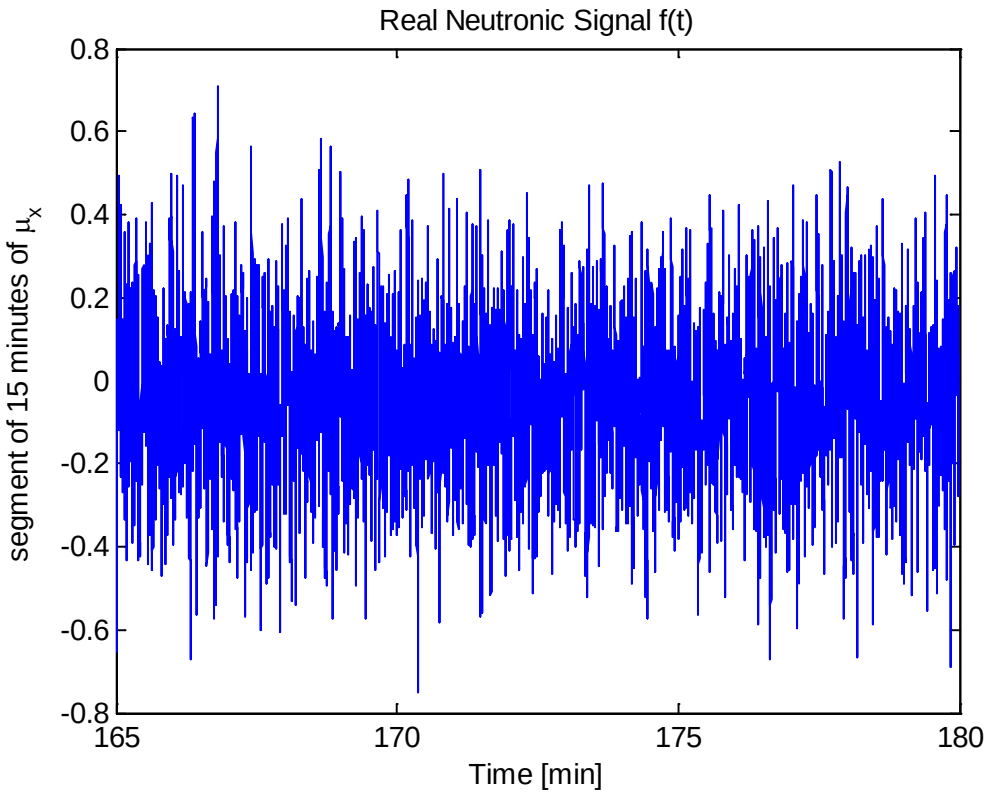

Figure 28. Real studied displacement component $\mu x(t)$.

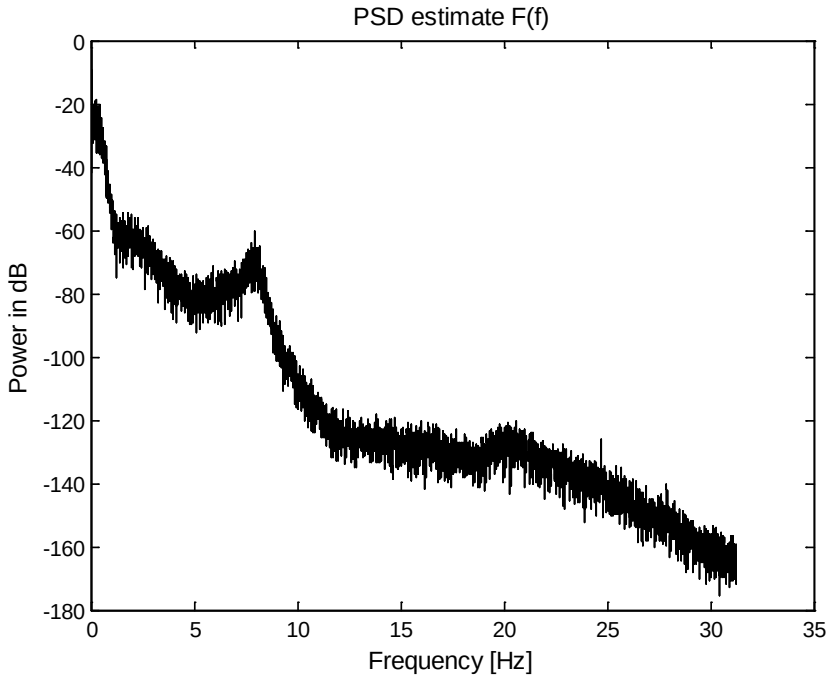

Figure 29. PSD estimate of the signal shown in Figure 28.

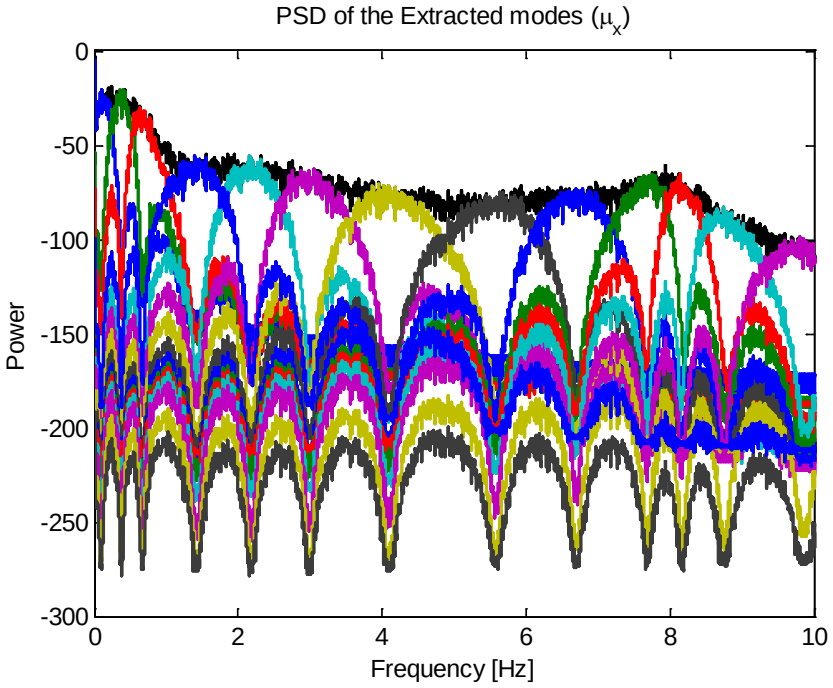

Figure 30. Welch PSD estimate of the IMFs extracted through VMD.

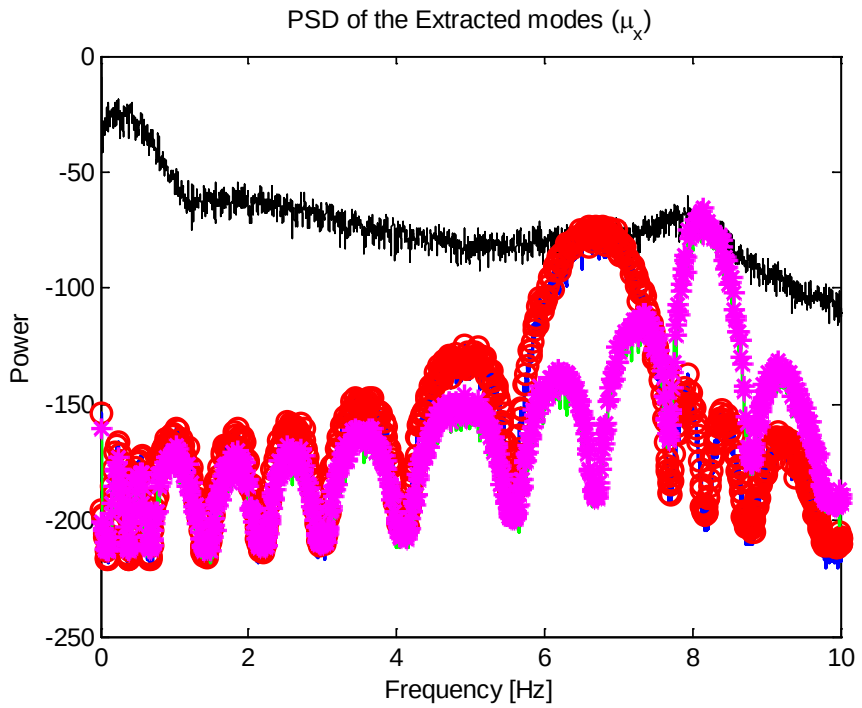

Figure 31. Detected Peaks of MODE 1 and MODE 2 that are used to infer the peak amplitudes (A_1 and A_2) and center frequencies (f_1 and f_2) of the extracted modes.

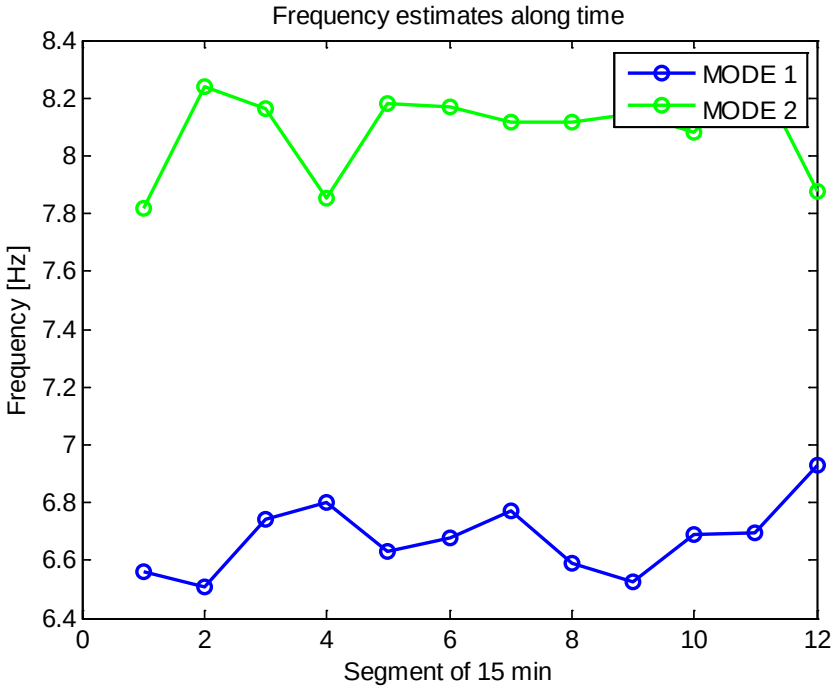

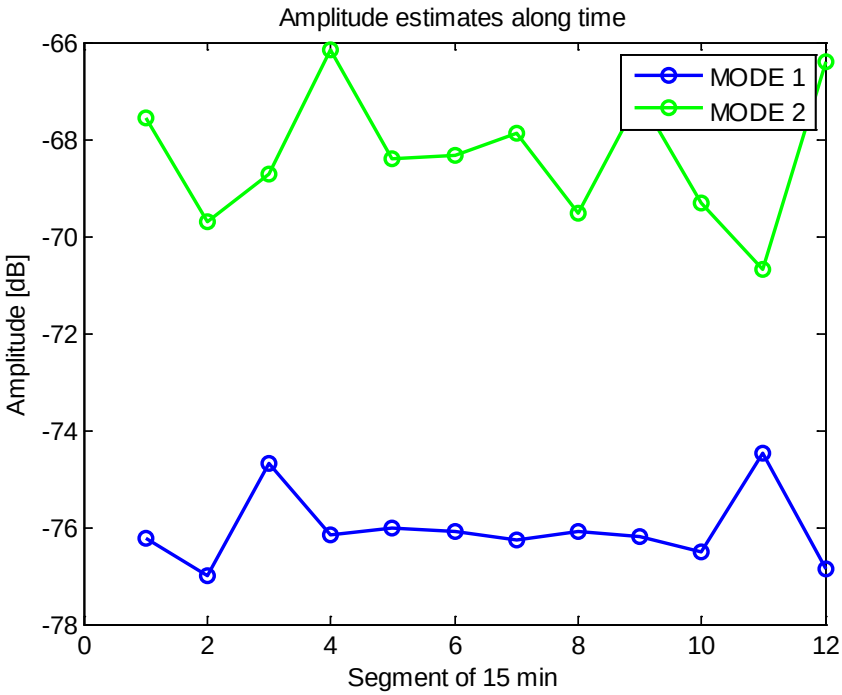

Figure 32. Estimated values of the central frequencies and amplitudes ($\mu x(t)$) for MODE 1 and MODE 2.

Estimates for **MODE 1**	Mean value	Standard deviation
Center Frequency f_1 [Hz]	6.7940	0.1002
Amplitude of the Peak A_1 [dB]	-75.9353	0.9563

Estimates for **MODE 2**	Mean value	Standard deviation
Center Frequency f_2 [Hz]	8.1276	0.0909
Amplitude of the Peak A_2 [dB]	-70.2712	0.7848

Table 8. Average value of the central frequencies and peak Amplitudes of the Upper displacement component $\mu x(t)$ estimated via a CBM-VMD analysis methodology.

For reasons of space to make the analysis less repetitive, only the analysis of the Upper detectors (the analysis of the Upper displacement components $\mu x(t)$) was presented in full detail, the center frequencies and peak amplitudes of all the detectors of the year 2017 (Upper and Lower) are shown in Table 9.

Estimates for **MODE 1**	Mean(f_1) Hz	Std(f_1) Hz	Mean(A_1) in dB	Std(A_1) in dB
UPPER				
$\mu x(t) = (N41U - N42U)/2$	6.7940	0.1002	-75.9353	0.9563
$\mu y(t) = (N43U - N44U)/2$	6.6768	0.1241	-76.0505	0.7566
LOWER				
$\mu x(t) = (N41L - N42L)/2$	7.5501	0.0801	-63.8572	1.9697
$\mu y(t) = (N43L - N44L)/2$	7.2593	0.0474	-67.8523	7.4194

Estimates for **MODE 2**	Mean(f_2) Hz	Std(f_2) Hz	Mean(A_2) in dB	Std(A_2) in dB
UPPER				
$\mu x(t) = (N41U - N42U)/2$	8.1276	0.0909	-70.2712	0.7848
$\mu y(t) = (N43U - N44U)/2$	8.0890	0.1561	-68.3178	1.3746
LOWER				
$\mu x(t) = (N41L - N42L)/2$	8.0186	0.0486	-60.6234	0.8639
$\mu y(t) = (N43L - N44L)/2$	8.0313	0.0524	-57.2062	0.6868

Table 9. Average center frequencies f_1 and f_2 (with their respective standard deviations (std)) and average peak amplitudes A_1 and A_2 (with their respective standard deviations (std)) for the 2017 year Core-Barrel Motion measurements.

To complete this study, Figure 33 shows the center frequency f_1 and A_1 (for MODE 1) for the Upper Detector to contrast the 2016 year estimate versus the 2017 year estimate. Figure 34 shows the Center frequency f_1 and A_1 (for MODE 1) for the Lower Detector. Figure 35 shows the Center frequency f_2 and A_2 (for MODE 2) for the Upper Detector and finally, Figure 36 shows the center frequency f_2 and A_2 (for MODE 2) for the Lower Detector.

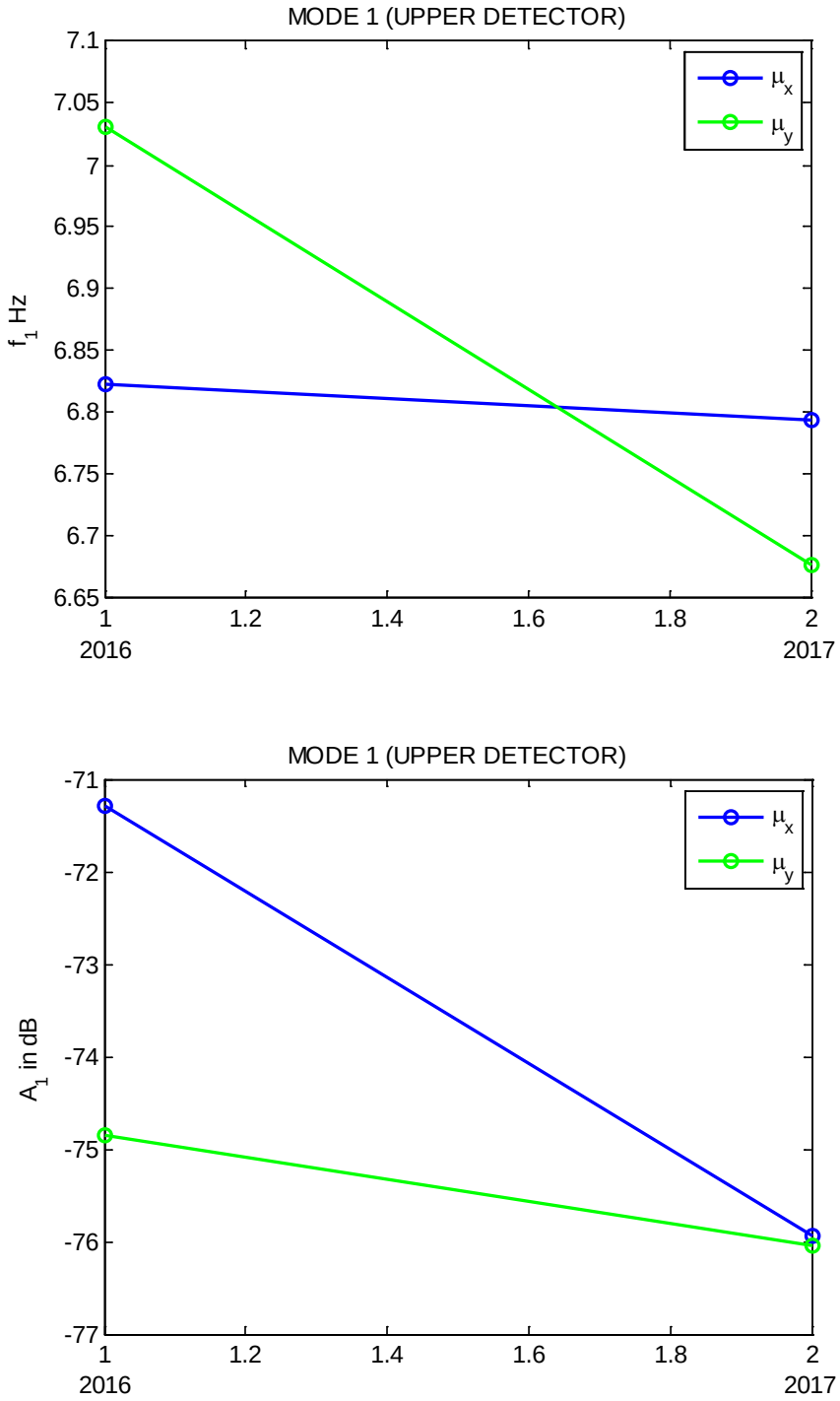

Figure 33. Center frequency f_1 and A_1 (for MODE 1) for the Upper Detector.

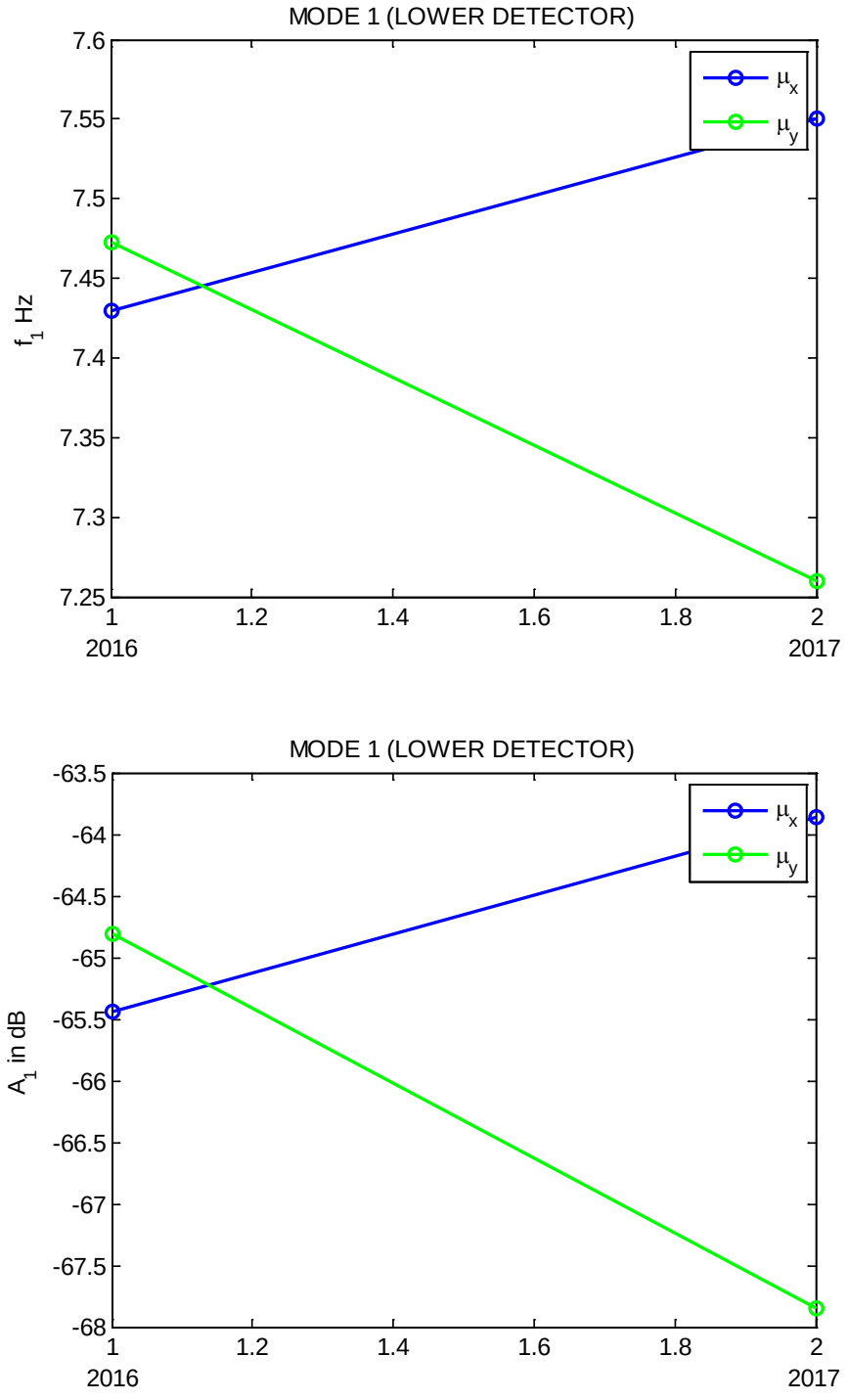

Figure 34. Center frequency f_1 and A_1 (for MODE 1) for the Lower Detector.

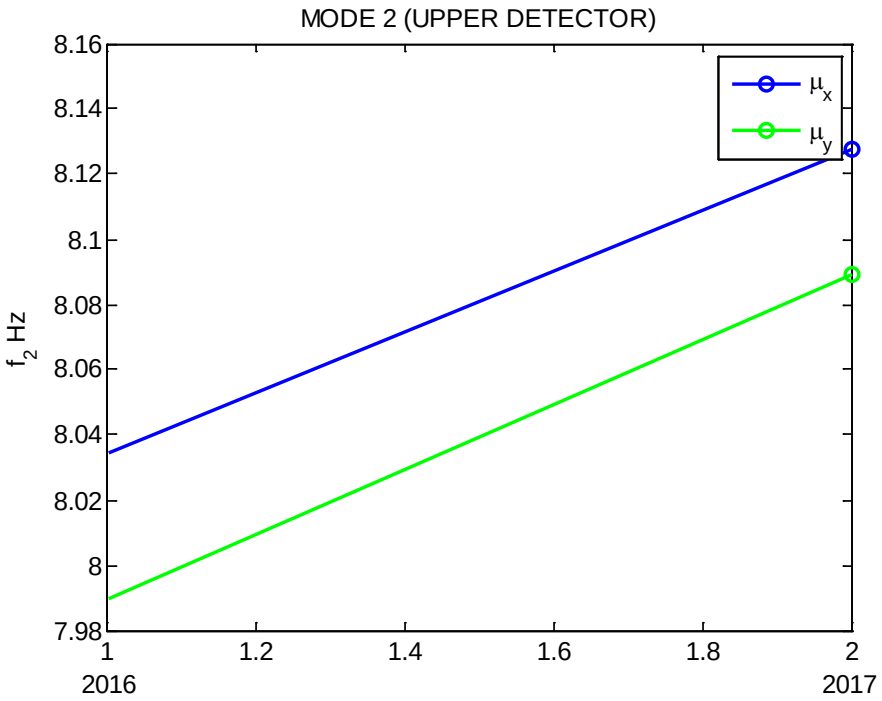

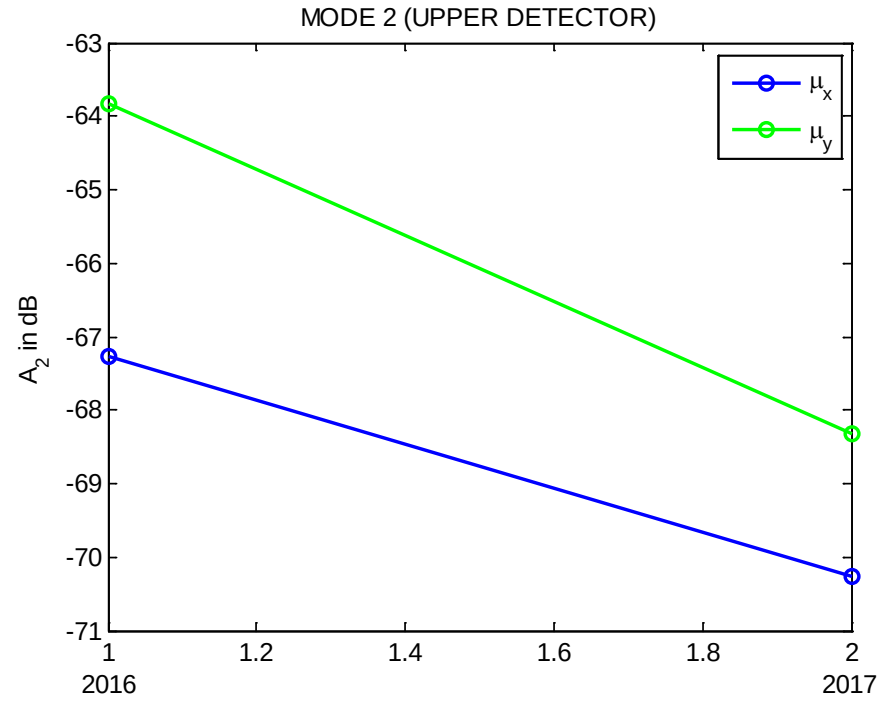

Figure 35. Center frequency f_2 and A_2 (for MODE 2) for the Upper Detector.

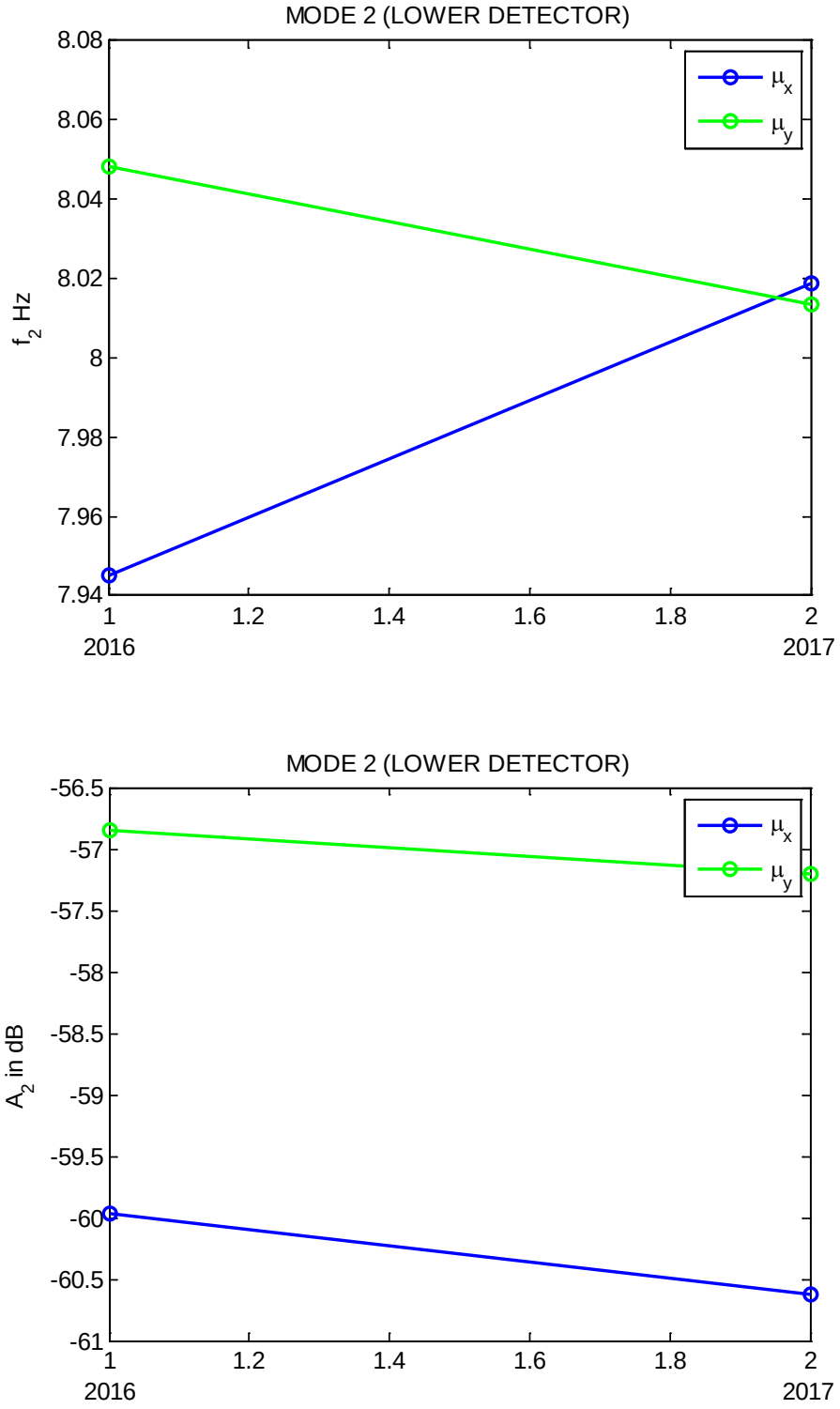

Figure 36. Center frequency f_2 and A_2 (for MODE 2) for the Lower Detector.

CONCLUSIONS

In this work, an entirely new Core Barrel motion (CBM) analysis methodology to study the beam mode was proposed based on the non-recursive Variational mode decomposition (VMD) model, which is an entirely recent non-recursive minimization method to decompose a signal into band-limited Intrinsic Mode Functions (IMFs) or simply *modes*. The model looks for an a priori given number of *modes* and their respective center frequencies, such that the modes reproduce the input signal, while being smooth after demodulation into baseband. This technique is related to Wiener filter denoising, in fact, this method is a generalization of the classic Wiener filter into adaptive, multiple bands. This method, excels the frequency resolution of the default Empirical Mode Decomposition (EMD) model and is suited to accurately separate harmonics whose frequency content lies very close to each other, even in noisy scenarios. Thus, this method is suited to isolate the beam mode of real neutronic CBM signals, our goal is to be able to detect the peaks of interest, the first one, a peak very close to 6.8 Hz (labeled as MODE 1) and the second one, another peak close to 7.9 Hz (labeled as MODE 2), later on, our goal is to infer the central frequency of the IMF and the amplitude of the peak (the global maxima) to provide information about the wear of the CMB. The methodology that was proposed splits the displacement components of interest ($\mu x(t)$ or $\mu y(t)$) signal into segments of 15 minutes (this signal splitting into various segments was performed due to computational resource constraints), then this 15 minute signal segment was decomposed via the VMD into 15 different independent *modes* (this number of IMFs to extract was chosen arbitrarily based on empirical experiments). Then, two *modes* are selected, the *modes* of interest around the beam mode area (MODE 1 and MODE 2), Via a simple peak detection method, the local maxima are detected, from the inferred global maxima : the central frequency of the MODE is computed, later to estimate the amplitude, a neighborhood of points J ($J = 5$ was the rule of thumb value that was chosen for the analysis) around the global maxima was selected to make the peak estimation of MODE 1 (and MODE 2) less arbitrary. The 2016 and 2017 Core-Barrel motion measurements where studied through this CBM-VMD new methodology.

REFERENCES

1. Huang, N. E., Shen, Z., Long, S. R., Wu, M. C., Shih, H. H., Zheng, Q., Yen, N. C., Tung, C. C., Liu, H. H., 1998. The empirical mode decomposition and the Hilbert spectrum for nonlinear and non-stationary time series analysis, in: Proceedings of the royal Society, pp. 903-995.

2. Wu, Z., Huang, N.E., 2009. Ensemble empirical mode decomposition: a noise assisted data analysis method. Adv. Adapt. Data Anal. 1, 1-41.

3. Torres, M.E., Colominas, M.A., Schlotthauer, G., Flandrin, P., 2011. A complete ensemble empirical mode decomposition with adaptive noise. IEEE International Conference on Acoustics, Speech and

Signal Processing (ICASSP), pp. 4144-4147.

4. Colominas, M. A., Schlotthauer, G., Torres, M. E., 2014. Improved complete ensemble emd: A suitable tool for biomedical signal processing. Biomedical Signal Processing and Control 14, 19-29.

5. Flandrin, P., Rilling, G., Goncalves, P., 2004. Empirical mode decomposition as a filter bank. IEEE signal processing letters, 11(2), 112-114.

6. Klügel, N., 2012. Practical Empirical Mode Decomposition for Audio Synthesis. In Int. Conference on Digital Audio Effects (DAFx-12), No. 2, 15-18.

7. Barnhart, B. L., Eichinger, W. E., 2011. Empirical mode decomposition applied to solar irradiance, global temperature, sunspot number, and CO 2 concentration data. Journal of Atmospheric and Solar-Terrestrial Physics, 73(13), 1771-1779.

8. Prieto-Guerrero, A., Espinosa-Paredes, G., 2014. Decay ratio estimation in boiling water reactors based on the empirical mode decomposition and the Hilbert-Huang transform. Progress in Nuclear Energy 71, 122-133.

9. Daubechies, I., Lu, J., Wu, H. T., 2011. Synchrosqueezed wavelet transforms: An empirical mode decomposition-like tool. Applied and computational harmonic analysis, 30(2), 243-261.

10. Gilles, J., 2013. Empirical wavelet transform. IEEE transactions on signal processing, 61(16), 3999-4010.

11. Carson, J., 1922. Notes on the theory of Modulation. Proceedings of the IRE, vol. 10, no. 1, 57-64.

12. Dragomiretskiy, K., Zosso, D., 2014. Variational mode decomposition. IEEE transactions on signal processing, 62(3), 531-544.

13. Tikhonov, A. N., 1963. Solution of incorrectly formulated problems and the regularization method. In Soviet Math. Dokl, vol. 5, 1035-1038.

14. Wiener, N., 1949. Extrapolation, Interpolation, and Smoothing of Stationary Time Series. Cambridge, MA: MIT Press.

15. Gonzalez, R. C., Woods, R. E., 1992. Digital Image Processing. Addison Wesley.

16. Hahn, S. L., 1996. Hilbert transforms in signal processing. Vol. 2. Boston: Artech House.

17. Welch, P., 1967. The use of fast Fourier transform for the estimation of power spectra: a method based on time averaging over short, modified periodograms. IEEE Transactions On Audio and Electroacoustics, 15(2), 70-73.

18. Butterworth, S., 1930. On the theory of filter amplifiers. Wireless Engineer, 7(6), 536-541.